Technische Universität München

Lehrstuhl für Experimentalphysik (E11)

Ultraschnelle Phänomene und Quantenoptik

Development & Characterization of Sources for high-energy, high-intensity coherent Radiation

Mag. rer. nat. Wolfram Helml

Vollständiger Abdruck der von der Fakultät für Physik
der Technischen Universität München zur Erlangung des akademischen Grades eines

Doktors der Naturwissenschaften

genehmigten Dissertation.

Vorsitzender:	Univ.-Prof. Dr. Martin Zacharias
Prüfer der Dissertation:	
	1. Univ.-Prof. Dr. Reinhard Kienberger
	2. Univ.-Prof. Dr. Franz Pfeiffer

Die Dissertation wurde am 11. Juli 2012 bei der Technischen Universität München eingereicht und durch die Fakultät für Physik
am 18. Juli 2012 angenommen.

Widmung

„Die richtig guten Ergebnisse kommen erst,
wenn der Leidensdruck groß genug ist.“

Alte Experimentalphysikerweisheit,
tradiert von Reinhard Kienberger

„Aber bei meiner Liebe und Hoffnung beschwöre ich Dich:
wirf den Helden in Deiner Seele nicht weg!
Halte heilig Deine höchste Hoffnung!“ –

Also sprach Zarathustra.
Friedrich Nietzsche

Zusammenfassung

Die Erzeugung ultrakurzer Lichtpulse [1] im Bereich von Femto- und Attosekunden (1 as = 10^{-3} fs = 10^{-18} s) hat die Tür zur wissenschaftlichen Erforschung bisher unzugänglicher Gebiete aufgestoßen und ermöglicht die Bobachtung von elekronischen Bewegungen auf deren natürlicher Zeitskala. Die Umverteilungsdynamik der Elektronen nach einer äußeren Störung oder nach einem inneren Umstrukturierungsprozess bestimmt die Eigenschaften und das Verhalten einer Vielzahl von Materialien. Daher gewährt die Fähigkeit, Elektronenbewegungen in Echtzeit zu verfolgen, einen tiefen Einblick in die Natur dieser fundamentalen Phänomene. Diese Methode ist im Prinzip auf so verschiede Systeme wie atomare Ensembles in der Gasphase, komplexe Moleküle und Festkörper, von Kristallgittern bis hin zu amorphen Materialien, anwendbar und kann sogar zur Untersuchung ultraschneller Reaktionen in organischen Strukturen [2] verwendet werden, wie sie z. B. Proteine, lebendige Viren (sofern Viren überhaupt als “lebendig” betrachtet werden können!) oder komplette Zellen darstellen.

Im letzten Jahrzehnt wurde eine ganze Menge bahnbrechender Experimente mit Hilfe dieses neuen Messinstruments und -konzepts [3] durchgeführt und aufregende und unerwartete Ergebnisse in verschiedensten Forschungsbereichen zutage gefördert [4]. Dennoch war die Machbarkeit vieler geplanter Studien gerade zu den interessantesten Untersuchungsgegenständen bisher beeinträchtigt, hauptsächlich durch zwei Unzulänglichkeiten der derzeit zu Messzwecken verfügbaren ultrakurzen Lichtpulse. Einerseits ist durch mangelnden Photonenfluss die benötigte hohe optische Intensität nicht gewährleistet, andererseits setzt die Beschränkung der Strahlung auf einen bestimmten Wellenlängenbereich den erreichbaren Photonenenergien eine obere Grenze. Das Thema der in dieser Arbeit vorgestellten Experimente ist es, Lösungen für diese Herausforderungen zu finden. Beide Einschränkungen werden betrachtet und verschiedene Problemlösungsansätze experimentell untersucht.

Die Erzeugung hoher Harmonischer der Grundwellenlänge eines Lasers ist eine der beiden Methoden mit denen ultrakurze Pulse im extrem ultravioletten (XUV) Spektralbereich erzeugt werden. In einem ersten Experiment verwendeten wir einen Laser mit 2.1 µm Wellenlänge und Pulsdauern, die nur wenigen Zyklen der Trägerwelle entsprechen, um die vorhergesagte günstige Skalierung der Umwandlung zu kürzeren Wellenlängen und damit zu höheren Photonenenergien zu untersuchen. Das gemessene Photoelektronenspektrum reicht deutlich über 1 Kiloelektronvolt hinaus [5], was bedeutet, dass ein langwelliger Treiberlaser ein vielversprechender Kandidat als künftige hochenergetische, ultrakurze Strahlungsquelle ist.

In einem zweiten Experiment wurde eine lockere Fokussierungsgeometrie in einem speziell konstruierten Strahlführungsaufbau verwendet, der es erlaubt mit Fokussierungslängen von 10 – 15 Metern zu arbeiten. Aufbauend auf einem Hochleistungslasersystem niedriger Repetitionsrate im nahen infraroten Bereich wurde der Photonenfluss pro Puls im Vergleich zu konventionellen Harmonischenquellen um Größenordnungen gesteigert. Diese Ergebnisse legen den Grundstein zur langerwarteten Erforschung der nichtlinearen Optik im Spektralbereich der extrem ultravioletten und weichen Röntgenstrahlung und ermöglichen die Durchführung von XUV Anregungs–Abfragemessungen zur zeitaufgelösten Untersuchung der Dynamik von Übergängen zwischen tiefliegenden atomaren Schalen und molekularer Zerfallsprozesse.

Schließlich wurden die zur Messung höherer Harmonischer entwickelten Methoden zur Charakterisierung eines neuartigen Freie-Elektronen-Lasers (FEL) verwandt, der die derzeit brillianteste Quelle ultrakurzer, kohärenter Röntgenstrahlung darstellt [6]. Mit dem Verfahren der Attosekunden-Schlierenspektroskopie konnten wir die Dauer der kürzesten verfügbaren Röntgenpulse an der Linac Coherent Light Source (LCLS) direkt in der Zeitdomäne im Einzelschussmodus messen und eine Obergrenze für die Pulslängen von nur wenigen Femtosekunden für einen bestimmten Bereich der FEL-Parameter bestätigen. Bei der Analyse der Substruktur dieser Pulse stellt sich heraus, dass einige der Schüsse nur aus einer einzigen ‘Sub-Spitze’ bestehen, die einer Dauer von lediglich $\sim$800 Attosekunden entspricht [7]. Die Kombination der ultrahohen Photonenintensitäten dieser Röntgenquelle mit der räumlichen Auflösung im Nanometer- und der aufgezeigten zeitlichen Auflösung im Attosekundenbereich bietet ein ideales Werkzeug zur Erforschung der Wechselwirkungen zwischen Licht und Materie auf deren natürlicher Zeitskala.

Abstract

The generation of ultrashort, femtosecond to attosecond duration (1 as = 10^{-3} fs = 10^{-18} s) optical pulses [1] has opened the door to previously unattainable regions of scientific research, allowing the observation of electronic motion on its natural temporal scale. Since the redistribution dynamics of electrons following external perturbations or internal reorganisation processes determine the behaviour and the properties of all kinds of matter, the ability to follow the electron movements in real time provides deep insights into the nature of these fundamental phenomena. This method is in principle applicable to such diverse systems as ensembles of gaseous atoms, complex molecules and solid bodies, ranging from crystal lattices to amorphous materials, and even to the investigation of ultrafast reactions happening in organic structures [2], like proteins, live viruses or whole biological cells.

A host of pioneering experiments utilizing this novel measurement tool and concept [3] has been conducted over the last decade and conveyed thrilling and often unexpected results [4] in a multitude of different research areas. Nevertheless, the practicability of many envisioned studies on the most interesting experimental subjects has been constrained up to date mainly by two shortcomings of the currently available ultrashort optical measuring pulses, namely by the lack of a suitably high photon flux and therefore limited intensities and by the restricted wavelength of the radiation, which sets an upper bound on the achievable photon energies. These challenges and the possible solutions are the topic of the experiments presented in this work. Both limitations are investigated and different ways to overcome them are experimentally tested.

Using a 2.1 μm-wavelength, few-cycle laser for high-order harmonic generation (HHG), one of the two methods employed for the creation of ultrashort pulses in the extreme ultraviolet spectral regime, the predicted favorable scaling of the conversion to shorter wavelengths and therefore higher photon energies is studied in a first experiment. The measured photoelectron spectra extend well above 1 kiloelectronvolt [5], making the long-wavelength driving laser a very promising candidate as a future high-energy, ultrashort-pulse radiation source.

In a second experiment with a loose focusing set-up, based on a high-power, low-repetition rate near-infrared laser system and a dedicated beamline allowing the implementation of focusing lengths of 10–15 meters, the photon flux per pulse is enhanced by orders of magnitude compared with conventional harmonic sources. These results pave the way to the long anticipated investigation of the regime of nonlinear optics in the XUV and soft X-ray spectral range and will allow the implementation of XUV pump/probe measurements for time-resolved studies of atomic inner-shell and molecular dissociation dynamics.

Finally, the methods developed in the measurement of HHG are applied to the characterization of a novel free-electron laser (FEL), which is currently the brightest source of ultrashort, coherent X-rays [6]. With the scheme of *attosecond streaking spectroscopy* we were able to measure the duration of the shortest available X-ray pulses at the Linac Coherent Light Source (LCLS) directly in the time domain on a single-shot basis, yielding an upper limit of the pulse duration of only a few femtoseconds for a certain FEL parameter range. Analyzing the substructure of these pulses we find that some of these shots consist of only one single 'sub-spike', with a temporal width in the range of $\sim$800 attoseconds [7]. Combining the ultrahigh photon intensities with the nanoscale spatial resolution and demonstrated attoscale temporal resolution of these X-ray sources offers an ideal tool for the investigation of light–matter interactions on their natural time scale.

During the doctoral studies the following papers were published or submitted to peer-reviewed journals with W. Helml as leading author or co-author:

[1] Intense 1.5-cycle near infrared laser waveforms and their use for the generation of ultra-broadband soft-x-ray harmonic continua
A. L. Cavalieri, E. Goulielmakis, B. Horváth, W. Helml, M. Schultze, M. Fieß, V. Pervak, L. Veisz, V. Yakovlev, M. Uiberacker, A. Apolonski, F. Krausz & R. Kienberger
New Journal of Physics **9**, 242 (2007), DOI: 10.1088/1367-2630/9/7/242

[2] TIMI 3 flow after primary angioplasty is an important predictor for outcome in patients with acute myocardial infarction
J. Kammler, A. Kypta, R. Hofmann, K. Kerschner, M. Grund, K. Sihorsch, C. Steinwender, Th. Lambert, W. Helml & F. Leisch
Clinical Research in Cardiology **98**, 165–170 (2009), DOI: 10.1007/s00392-008-0735-9

[3] Attosecond control of tunneling ionization and electron trajectories
M. Fieß, B. Horváth, T. Wittmann, W. Helml, Y. Cheng, B. Zeng, Z. Xu, A. Scrinzi, F. Krausz & R. Kienberger
New Journal of Physics **13**, 033031 (2011), DOI: 10.1088/1367-2630/13/3/033031

[4] Single-Shot Carrier-Envelope Phase Measurement of Few-Cycle Laser Pulses
T. Wittmann, B. Horvath, W. Helml, M. G. Schätzel, X. Gu, A. L. Cavalieri, G. G. Paulus & R. Kienberger
Nature Physics **5**, 357–362 (2009), DOI: 10.1038/NPHYS1250

[5] Sub-femtosecond K-shell excitation with a Few-Cycle Infrared Laser Field
G. Marcus, W. Helml, X. Gu, Y. Deng, R. Hartmann, T. Kobayashi, L. Strueder, R. Kienberger & F. Krausz
Physical Review Letters **9**, 023201 (2012), DOI: 10.1103/PhysRevLett.108.023201

[6] Femtosecond x-ray pulse length characterization at the Linac Coherent Light Source free electron laser
S. Düsterer, P. Radcliffe, C. Bostedt, J. Bozek, A. L. Cavalieri, R. Coffee, J. T. Costello, D. Cubaynes, L. F. DiMauro, Y. Ding, G. Doumy, W. Helml, W. Schweinberger, R. Kienberger, A. R. Maier, F. Grüner, M. Messerschmidt, V. Richardson, C. Roedig, T. Tschentscher & M. Meyer
New Journal of Physics **13**, 093024 (2011), DOI: 10.1088/1367-2630/13/9/093024

[7] Direct time domain measurement of the world's shortest X-ray pulses
W. Helml, A. R. Maier, W. Schweinberger, I. Grguras, P. Radcliff, G. Doumy, C. Roedig, J. Gagnon, M. Messerschmidt, F. Grüner, J. D. Bozek, T. Tschentscher, J. T. Costello, M. Meyer, R. Coffee, S. Düsterer, A. L. Cavalieri & R. Kienberger
Under review by *Nature Photonics*

Contents

Widmung **III**

Zusammenfassung **V**

Abstract **VII**

Contents **XI**

List of Figures **XIII**

List of Tables **XV**

Introduction **1**

1 Fundamentals of ultrashort, high-energy EM pulse generation **3**
1.1 Overview of high-energy pulse generation 3
1.2 Strong field–matter interaction 4
1.2.1 High-order harmonic generation (HHG) 6
1.2.2 Elastic rescattering & inelastic recollision 10
1.3 HHG with a longer-wavelength driver IR laser 10
1.4 Free-Electron Lasers 13
1.4.1 Undulator radiation 13
1.4.2 Self-amplified spontaneous emission (SASE) 16
1.4.3 Characteristics of SASE FEL X-ray pulses 19

2 Scaling the energy of HHG towards the keV regime **23**
2.1 The LWS 1 OPCPA system 23
2.1.1 Principles of broadband OPA systems 26
2.1.2 Seed & pump pulse generation 29

2.1.3 Stretcher & compressor design . . . 33
2.1.4 OPA design & parametric superfluorescence . . . 34
2.1.5 OPCPA system output & pulse characterization . . . 36
2.2 Experimental set-up — the beamline AS 4 . . . 39
2.2.1 The high harmonic generation set-up . . . 39
2.2.2 High harmonic detection with the pnCCD camera . . . 42
2.3 HHG in the keV regime . . . 44
2.4 Direct inner-shell electron excitation . . . 51
2.5 Conclusion . . . 56

3 Scaling the intensity of XUV pulses for high-flux experiments 59
3.1 The LWS 20 OPCPA system . . . 60
3.2 Experimental set-up — the beamline AS 6 . . . 64
3.3 High-flux harmonics at 100 eV . . . 67
3.4 Conclusion . . . 73

4 Temporal characterization of a high-intensity X-ray source 75
4.1 The LCLS at the SLAC National Accelerator Laboratory . . . 76
4.2 Basic principles of streaking spectroscopy . . . 80
4.3 The instrumentation at the AMO hutch . . . 83
4.3.1 Experimental set-up and alignment . . . 83
4.3.2 FEL settings . . . 85
4.3.3 Magnetic bottle electron spectrometer (MBES) . . . 86
4.4 Direct time domain measurement of ultrashort X-ray pulses . . . 86
4.4.1 Single-shot X-ray pulse duration measurement . . . 88
4.4.2 Measurement of sub-femtosecond X-ray pulses . . . 92
4.5 Conclusion . . . 96

Summary & Outlook 97

A Build-up of the beamline AS 6 101

B List of Acronyms 109

References 111

Danksagung 125

List of Figures

1.1 Strong-field light–matter interaction 7
1.2 HHG with IR wavelenghts 12
1.3 LCLS site at SLAC 14
1.4 Undulator radiation 15
1.5 Electron–X-ray self-interaction 17
1.6 Microbunching and exponential gain 18
1.7 Intensity spiking in the time domain 21

2.1 Principle of OPCPA 24
2.2 Sketch of the noncollinear OPA geometry 28
2.3 Schematic of the LWS 1 mid-IR OPCPA system 30
2.4 Seed pulse spectra 31
2.5 Calculated GD curves 33
2.6 Calculated small-signal OPA gains 35
2.7 Spectral measurement of the superflourescence 37
2.8 FROG traces of the compressed IR pulse 38
2.9 CEP measurement of the OPCPA output pulse 39
2.10 Outline of the beamline AS 4 41
2.11 Layout of the pnCCD camera chip 43
2.12 Schematic drawing of events on the pnCCD 45
2.13 Image of HH beam at AS 4 46
2.14 High harmonic spectra from Ne and N_2 47
2.15 Spectral contributions from multi-pixels events 48
2.16 Comparison of real and ‘pseudo’ spectra 49
2.17 HH yield as a function of the backing pressure 50
2.18 Comparison of beam profiles at different photon energies 53

2.19 Comparison of electron recollision models 55

3.1 Set-up of the high-power OPCPA LWS 20 61
3.2 Pulse duration & spectrum of LWS 20 63
3.3 AS 6 Beamline at the MPQ 66
3.4 AS 6 XUV characterization assembly 67
3.5 LWS 20 beam at HHG focus 68
3.6 Plasma in HHG focus at AS 6 69
3.7 Harmonic beam from LWS 20 70
3.8 Harmonic spectra from LWS 20 71
3.9 Determination of the XUV intensity 72

4.1 LCLS machine layout 76
4.2 The slotted spoiler 78
4.3 Basic concept of streaking spectroscopy 82
4.4 Experimental set-up and measurement principle at the LCLS . . 84
4.5 Streaked X-ray photoelectron spectra 87
4.6 Determination of FEL–IR arrival time jitter 89
4.7 Streaking of few-femtosecond X-ray pulses 91
4.8 Average FEL pulse duration 93
4.9 Measurement of an attosecond X-ray pulse 95

A.1 The crane is ready 101
A.2 Lifting 102
A.3 The first part is up! 103
A.4 Pillars needed 104
A.5 . . . hurry up! 104
A.6 Ready for a test 105
A.7 Good work! 105
A.8 From Bridge to chamber 106
A.9 Finishing touches 106
A.10 AS 6 beamline at work 107

List of Tables

2.1 Parameters for the theoretical model of electron recollision . . . 57

4.1 LCLS machine parameters 77

Introduction

The penultimate goal of the first historically recorded efforts of classical natural philosophers was to gain a deeper insight into the workings of the surrounding world and to be able to better predict the oftentimes greatly arbitrarily seeming behaviour of nature. This very quest has ultimately led to some of the most astonishing accomplishments of the human mind, giving rise to discoveries spanning an ever larger scope of both space and time.

From the very beginnings always the extreme facets of the whole spectrum of phenomena have been the most intriguing ones for the human mind. In space, the question of the fabric and extension of the skies and the universe even beyond, possibly reaching into infinity or the identity of the smallest constituents of the matter surrounding us, down to the 'impartible'—the atoms. And, in a parallel, temporal vein, the far away future or the distant past, the history of the cosmos or its destiny and, on the opposite side of the range, the tiniest moments, the way motion can happen at all if you look at it at shorter and shorter intervals of time, like in Zeno's famous paradox of Achilles and the tortoise [1].

This last aspect of scientific research has maybe been developed the most during the past decades, having seen the invention of instruments that can directly measure time spans first in the picosecond [2], then the femtosecond [3] and recently in the attosecond [4] temporal region (1 as = 10^{-3} fs = 10^{-6} ps = 10^{-18} s). The accessibility of this new regime of physics relies on the discovery of two novel methods to pump and probe matter with specially designed laser pulses and was therefore dubbed 'ultrafast' optics. It is remarkable, that the shortest time intervals and the temporally most distant events can both be best understood by literally shedding light on them.

On the one hand so-called 'free-electron lasers' (FELs, see section 1.4) nowadays provide an ultrabright source of radiation in a wavelength range from ~ 15 nm to ~ 0.15 nm and with pulse durations between hundreds of femtoseconds down to the sub-10 fs region, delivering peak powers of more than 10 GW.

On the other hand this development was driven by the advent of laser pulses consisting of only a few oscillations of their underlying electromagnetic field and their application to generate even shorter optical pulses in the extreme ultraviolet (XUV) and soft X-ray regime, a process called high-order harmonic generation (HHG, compare section 1.2.1). Although this technique currently exhibits some limitations in photon energy and flux, it represents a table-top tool and has produced the worldwide shortest pulses ever measured up to date [5].

In chapter 1 a short introduction about the basics of ultrashort optical pulse generation is given and the two above mentioned current methods of their generation are discussed in some detail. Chapter 2 reports on the experiments with a few-cycle, mid-infrared laser to extend HHG sources to higher photon energies in the range of 1 keV and above. The low photon flux, another restriction of current HHG schemes, is investigated in chapter 3 and a possible solution provided in form of a set-up with a loose focusing geometry and a high-power driving laser. Chapter 4 finally demonstrates the capability of a state-of-the-art FEL to produce ultrabright X-ray pulses with few-femtosecond and in some cases even sub-femtosecond durations by successfully applying the attosecond measurement technique of *photoelectron streaking spectroscopy* to such a system. A short summary of the findings and an outlook are given at the end of this work.

Chapter 1

Fundamentals of ultrashort, high-energy electromagnetic pulse generation

1.1 Overview of high-energy pulse generation

Today the most widely used technique to generate coherent extreme-ultraviolet (XUV) and soft X-ray radiation is a process called high-order harmonic generation (HHG). In the usual set-up a high-intensity laser pulse interacts with a gaseous target inside a vacuum chamber, whereupon part of the energy of the driver pulse is converted via a highly nonlinear process into light at odd harmonics of the fundamental laser. The emitted radiation is fully coherent, has a small divergence, is polarized in the same direction as the generating laser field and can cover an energy range from a few tens of electronvolts (eV) up to a few hundred eV, when generated with the conventional ultrashort-pulse 800-nm Ti:sapphire laser. The highest achieved harmonic energy with a driving source at this wavelength was reported to extend even beyond 1 keV [6], reaching well into the X-ray regime. Due to the shorter optical period below 1 femtosecond (fs, 1 fs = 10^{-15} s) and the temporal coherence of these sources, laser pulses with sub-femtosecond durations are made available. These attosecond (as, 1 as = 10^{-3} fs = 10^{-18} s) pulses were first demonstrated in 2001 [4, 7, 8] and have since then been utilized in a number of time-resolved experiments (e. g. [9–17]). Thus, high-order harmonic generation has been

developed to a reliable and indispensable tool, opening a new era of ultrafast measurements on the natural time-scale of atom and electron dynamics.

The second method currently employed to generate coherent high-energy radiation was already invented in 1971 [18] in the form of free-electron lasers (FELs), initially as high-intensity laser sources from the far-infrared through the visible spectral region [19, 20], which has since been extended to ever higher photon energies and intensities. However, only with the advent of FELs based on the principle of self-amplified spontaneous emission (SASE) [21, 22] radiation wavelengths in the extreme ultraviolet and even the soft and hard X-ray regime have been made accessible [23–26]. At the same time, also the available pulse durations have steadily become shorter, eventually reaching the few-femtosecond or even sub-femtosecond level at the Linac Coherent Light Source (LCLS) [25, 27]. Whereas the above described HH sources readily fit onto a laboratory table, the FELs of the last generation are large-scale machines, requiring an electron accelerator often extending over more than one kilometer and another storehouse-sized device called an undulator (see sec. 1.4.1) for their operation. On the other hand, these novel FELs are distinguished from every other current X-ray source by their ultrahigh peak brightness, defined as the photon flux per frequency bandwidth per unit phase space volume, which is about 10 orders of magnitudes higher than for the former workhorses of X-ray generation in the form of incoherent synchrotron radiation based on electron storage rings [28].

1.2 Strong field–matter interaction

The interaction between light and matter has been a topic of investigation from the very first days of natural science and has never stopped to occupy thinkers throughout the centuries. The names of the most famous natural philosophers and researchers are always also connected with breakthrough discoveries in the field of optics. Not only in a historical sense this area of investigation lies at the heart of modern physics, exemplary in the form of Einstein's famous explanation of the photoelectric effect [29]. Over the last hundred years our knowledge on electromagnetic (EM) radiation has steadily been extended, and the invention of the laser, triggered by the success of the maser [30] and first

demonstrated by Maiman in 1960 [31], has lead to an even increased interest in the fundamental properties of light. Today we are able to investigate the dynamics of radiation and matter on the natural time scales of the basic constituents of these processes, namely the time an electron needs to travel once around the core of the hydrogen atom in Bohr's model, which is roughly 150 as.

The key to access these ultrafast electronic reactions in matter was the development of very powerful and extremely short laser pulses that open the door to the regime of *nonlinear optics*. The area of optics that we will deal with in this chapter is characterized by an electrical field strength of the incident laser that is comparable to the atom's binding field of the outer-shell electrons. If this happens, the electron can escape from the atom by way of tunneling ionization, and its behaviour is subsequently governed by the electric field of the laser pulse. Driven by this external field, the electron performs a 'wiggling' motion with an amplitude that can exceed the Bohr radius by orders of magnitude, thereby gaining considerable energy. This cycle-averaged kinetic or ponderomotive energy can be substantially higher than the atom's binding energy or, as we will see in chapter 2, even the ionization potential of deeper bound inner-shell electrons, depending on the lasers intensity and its central wavelength. For the scope of optical wavelengths, from near-infrared (NIR) to the mid-infrared region, used in the below described experiments the laser intensities giving rise to these processes are around $\sim 1 \times 10^{15}$ W/cm^2 and above and the associated range of parameters is referred to as the *strong-field regime* [32].

At moderate, slightly lower intensities, $\sim 10^{13}$–10^{14} W/cm^2, the electric field is not strong enough to allow tunneling ionization from the atom, but the predominant mechanism of excitation is multiphoton or above-threshold ionization. A mathematical way to discern these two regimes is provided by the Keldysh parameter γ [33], a scaling parameter that is given by

$$\frac{1}{\gamma} = \frac{eE_0}{\omega_L \sqrt{2m_e W_b}} = \frac{eE_0 a_B}{\hbar \omega_L}, \tag{1.1}$$

where E_0 and ω_L are the amplitude and the angular carrier frequency of the electric field, while $m_e = 9.11 \times 10^{-31}$ kg and $e = -1.6 \times 10^{-19}$ C are the electron rest mass and charge, respectively, and $W_b \gg \hbar\omega_0$ is the ionization

potential of the atom. $\hbar = 1.06 \times 10^{-34}$ Js is the reduced Planck constant and $a_B = 0.053$ nm is the Bohr radius that are connected with the ionization potential and the electron mass via $a_B = \hbar/\sqrt{2m_e W_b}$. If $\gamma^{-1} < 1$ we are in the multiphoton ionization regime, whereas for $\gamma^{-1} > 1$, the laser field strongly suppresses the atom's Coulomb potential, so that tunneling ionization may take place. For a simple picture of these different regimes take a look at Fig. 1.1, which will be discussed later in more detail.

This behaviour can be further understood, if we make a quick estimation of the acquired wiggling amplitude a_w and the ponderomotive energy U_p in the field of a laser with intensity $I = 10^{15}$ W/cm^2 and at a central wavelength of $\lambda_0 = 1$ μm. Under these conditions the evolution of the electron in the laser field can be calculated clasically [34] (see also the next section) and the respective values are derived to be $a_w = 12.4$ nm and $U_p = 93$ eV [32]. Therefore, in the case of $\gamma^{-1} > 1$ the electron is accelerated far away from the mother ion and acquires a large kinetic energy in a fraction of the lasers's oscillation period. This clearly indicates the dominant influence of the intense electric field over the atom's Coulomb field and gives rise to the observed phenomena connected with the strong-field regime of light–matter interaction.

The process of high-order harmonic generation is a special case of strong-field nonlinear optics in the non-relativistic regime and is described by the infamous semiclassical three-step model derived by Corkum and others [34, 35]. For an intuitive sketch of the sequence of the three steps see Figure 1.1: In the first step the intense laser field bends the Coulomb potential of the atom in a way, that a valence-shell electron can tunnel out of the potential well and escape into the continuum (1b). In the second step, the electron is accelerated away in the laser field and gains energy. Since the electric field oscillates sinusoidally, eventually it reverses its sign, whereupon the electron is accelerated back again towards the mother ion (2). Finally, the electron can recombine with the ion, thereby setting free the accumulated ponderomotive energy in an ultrashort burst of high-energy radiation (3a).

1.2.1 High-order harmonic generation (HHG)

After this qualitative description of the three-step model, the individual steps involved and the relevant assumptions shall be discussed in more detail. As

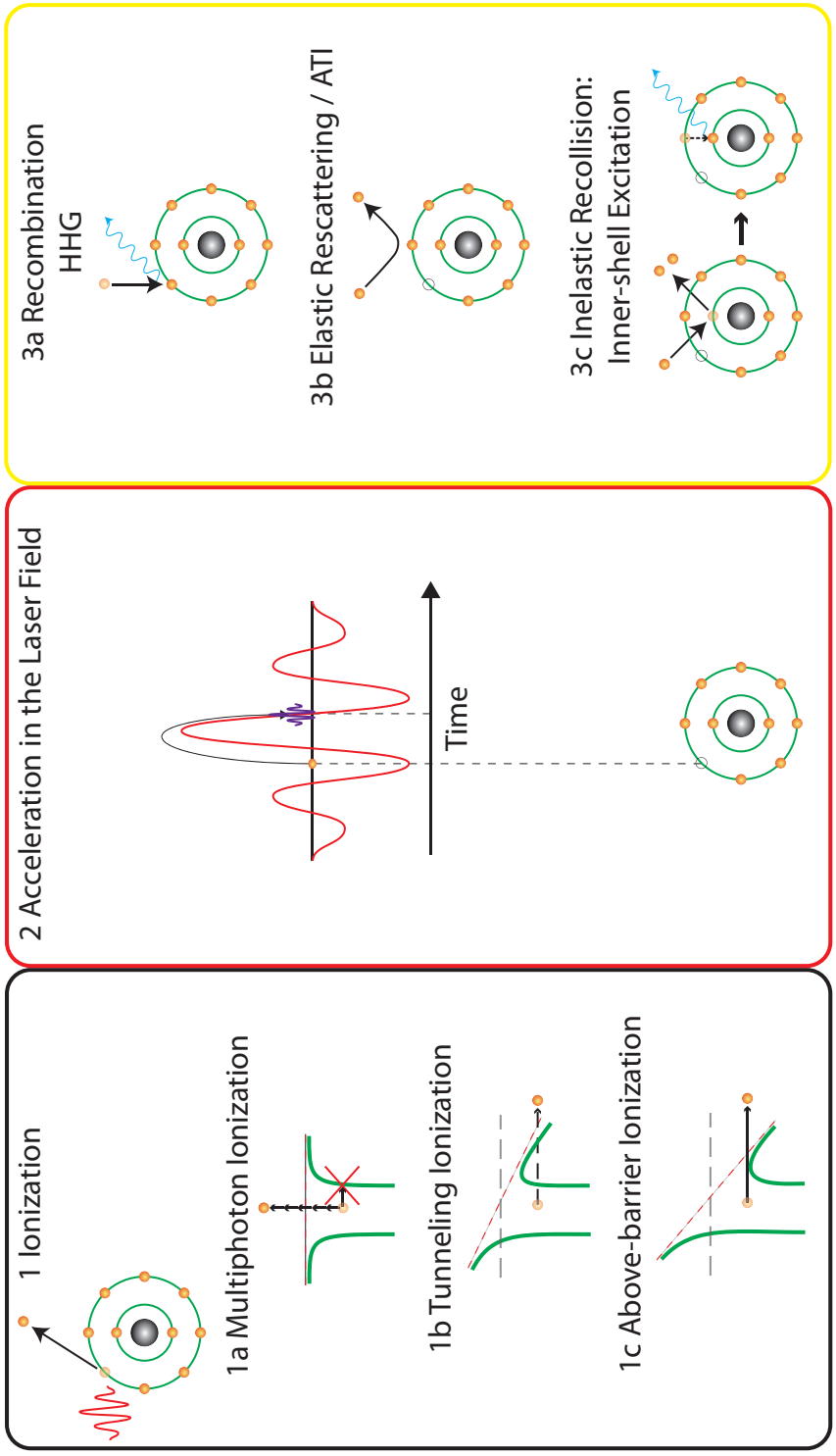

Figure 1.1: Schematic drawing of the interaction of an intense, few-cycle light field with atomic matter and possible outcomes. A detailed discussion of the different steps is given in the main text.

a general synopsis of strong light–matter interactions and for further detailed discussion, including a quantum mechanical analysis and a host of continuative references, the review paper by Krausz & Ivanov [36] is to be recommended.

Let's assume a linearly polarized, few-cycle laser electric field given by

$$E_L(t) = E_0 f(t) \cos(\omega_L t + \varphi), \tag{1.2}$$

where E_0 and ω_L are again the amplitude and the angular carrier frequency, $f(t)$ is a real-valued envelope function with the peak normalized to 1 at $t = 0 \equiv t_0$, so that $f(t_0) = 1$ and φ is the carrier–envelope (CE) phase, which determines the timing of the field oscillations with respect to the pulse peak, $\Delta t_0 = \varphi/\omega_L$. Since the suppression of the Coulomb potential, necessary for the tunnel ionization of the atom, is highly sensitive to the electric field, it only happens near the extrema of the oscillating field, twice per optical cycle. Thus the electron emission is confined to a small window, with a duration of only a fraction of the half-cycle period.

Once the electron has tunneled through the Coulomb wall, it emerges in the continuum with zero velocity $v(t_b) = 0$, where t_b is the moment of tunnel ionization and the instant 'birth' of the free electron outside the atom, and the electron is immediately accelerated away from the ion by the strong laser field. Thus, in the strong-field approximation (SFA), which is applicable for the laser intensities we are studying here, the Coulomb field of the ion can be neglected and the motion of the electron in the electric laser field can be described classically by

$$m_e \ddot{x} = -eE_L(t); \tag{1.3}$$

here and in the rest of this section we use the system of Hartree atomic units [au]: $\hbar = e = m_e = \frac{1}{4\pi\epsilon_0} = 1$, with $\hbar$, e and m_e being the reduced Planck constant and the electron charge and rest mass specified above, and ϵ_0 is the electric constant with the value $\epsilon_0 = 8.85 \times 10^{-12}$ F/m in SI units. Defining the vector potential $A_L(t)$ as

$$E_L(t) = -\frac{dA_L}{dt}, \tag{1.4}$$

this equation of motion can be integrated, leading to the time-dependent electron momentum

$$p(t) = eA_L(t) - eA_L(t_b). \tag{1.5}$$

The final momentum of the electron, after the electric field has passed by, is therefore

$$p_f = e\underbrace{A_L\left(\lim_{t\to\infty}\right)}_{=0} - eA_L(t_b) = -eA_L(t_b), \tag{1.6}$$

where the acquired momentum is uniquely determined by the electric field at the moment of ionization of the atom. The instant of release also decides if an electron will be brought back to the ion upon reversal of the sign of the electric field at the maximum, which can be shown by integrating equation (1.5) again, yielding the respective electron trajectories. These electrons can then recombine with their mother ions and their maximum kinetic energy sets an upper limit for the photon energy of the emitted high harmonic radiation via [34, 37, 38]

$$\Omega_{max} \approx I_p + 3.17\,U_p. \tag{1.7}$$

Here I_p is the ionization potential and U_p is the cycle-averaged wiggle energy of the electron in the laser field, given by

$$U_p(t) = \frac{E_0^2 f^2(t)}{4\omega_L^2} = \frac{E_0^2 f^2(t)\lambda_L^2}{16\pi^2 c^2} \tag{1.8}$$

in atomic units. It is evident from eq. (1.8) that the harmonic cutoff energy can be extended either by increasing the laser intensity I_L, as $U_p \propto E_0^2 \sim I_L$, or by utilizing lasers with longer wavelengths, which might even be preferable, because of the favorable quadratic scaling $U_p \propto \lambda_L^2$. This route shall be described in section 1.3, whereas our experimental results generating high-energy harmonics with a 2.1 µm-wavelength IR driving laser are presented in chapter 2.

1.2.2 Elastic rescattering & inelastic recollision

Very briefly, the other two cases for the third step in the light–matter interaction diagram sketched in Figure 1.1 shall be described.

Elastic rescattering

Panel 3.b of Fig. 1.1 depicts the process of rescattering, where the electron is not recombining with the ion, but is rather elastically backscattered. The final energy of these electrons does not only depend on the electric field at the moment of initial ionization, but also of the time of recollision. It can be shown that for certain, well defined instances of the electric field the energy of the backscattered electrons may reach values as high as $10\,U_p$ [39]. Therefore, the final energy and the number of backscattered electrons are very sensitive to the carrier wave evolution, especially for few-cycle pulses. This effect has been utilized to determine the phase of the carrier with respect to the envelope without residual ambiguity [40], and just recently we were able to accomplish these measurements in a single-shot mode [41].

Inelastic recollision

In contrast, panel 3.c of Fig. 1.1 illustrates inelastic recollision of the accelerated electron, which can lead to nonsequential double ionization of the atom with high efficiency [42, 43]. Of special interest would be the recollision with high enough energies to excite inner-shell electrons. Since the relevant energies in rare gases are well above the cutoff energy for the usual 800 nm-harmonics ($\sim$870 eV for the Ne 1s shell for example), this has not been accomplished so far. In section 2.4 I will report on the first evidence for direct inner-shell excitation in neon via inelastic recollision driven by a few-cycle, 2.1 μm-wavelength IR laser.

1.3 HHG with a longer-wavelength driver IR laser

The typical driver laser for HHG and attosecond pulse generation is provided by a Ti:sapphire amplifier system, producing few-cycle pulses of a few hundred

microjoules at ∼800 nm [44–46]. To reproducably generate attosecond pulses for ultrafast time-resolved measurements the driving laser's carrier–envelope phase (CEP) has to be stabilized by a combination of a fast control loop, regulating the oscillator pumping power, thereby ensuring that every pulse picked for amplification exhibits the same waveform, and a slower working compensation of the CE phase drift accumulated in the amplifier [47, 48]. As an example, the shortest pulse ever measured was an 80-as pulse generated with a driver of this kind [5]. While such isolated attosecond pulses have been widely applied in many experiments [49], their photon energies have unfortunately been limited to ∼100 eV and thus the measurements have been restricted to weakly bound electronic states.

We have seen that the single-atom cutoff energy for HHG can be derived to be

$$\hbar\Omega_{max} = I_\mathrm{p} + 3.17\,U_\mathrm{p} = I_\mathrm{p} + \frac{3.17e^2}{16\pi^2 c^2 m_e} I_\mathrm{L}\lambda_\mathrm{L}^2, \tag{1.9}$$

where I_p is the ionization potential, and the ponderomotive potential U_p scales with the driver laser intensity I_L and the square of the laser wavelength λ_L, and we have, for the sake of completeness, explicitly written the reduced Planck constant $\hbar$, the elementary charge e and the rest mass of the electron m_e, which are set to unity in atomic units.

The possibility of generating soft X-ray photons up to keV with a tabletop system is a long-standing goal for all fields of spectroscopic research, from nonlinear optics and quantum chemistry to material science and even biological research. Especially the efficient generation of intense, coherent radiation in the spectral range of he so-called 'water window' (∼280 to 530 eV) is highly sought after for biomedical imaging, because of the possibility to selectively image carbon atoms without water absorption.

Scaling the XUV photon energy by increasing the driving laser intensity leads to ionization depletion of the target atoms, which effectively sets a maximum boundary on the applicable fundamental laser intensity at the focus to $I_\mathrm{L} \approx 10^{14}$–$10^{15}$ W/cm^2. To circumvent this intensity limitation, another possibility to achieve higher photon energies is to utilize longer driver laser wavelengths. This route is also clearly favored by the single-atom cutoff formula given above, where the ponderomotive potential is proportional to the square

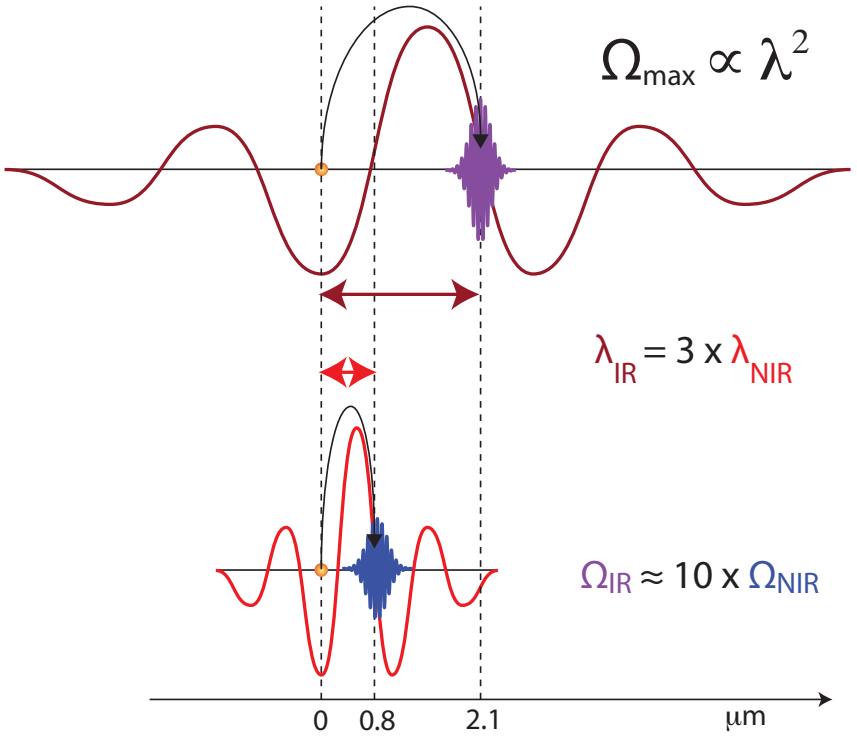

Figure 1.2: Sketch of HHG with an 800-nm and a 2.1-μm-wavelength driver laser. Intuitively it can be understood, that the electron gains more kinetic energy during the longer sojourn in the IR laser's electric field, which is indicated in the graphic by the violet colour of the emitted XUV pulse. The intensity of the HH radiation from the 2.1-μm-laser is overrepresented by this figure, since the single-atom efficiency for harmonic generation drops significantly with the wavelength, as is mentioned in the text.

of the driver laser wavelength (see Fig. 1.2). To quantify this wavelength dependence, eq. (1.9) predicts a HH cutoff energy of considerably above one keV for a 2.1-μm driver laser with 1 PW/cm^2 laser intensity, compared to 205 eV with a 800-nm laser at the same intensity.

Theoretical studies [50] confirm this intuitive behavior of the cutoff energy, although a strong decrease of the harmonic intensity with longer driver wavelengths is predicted in the single-atom picture, indicating a harmonic yield scaling like $\approx \lambda^{-5.5\pm0.5}$ [51, 52]. Nevertheless, simulations taking into account propagation effects of the fundamental laser and the generated harmonic beam in the interaction medium imply a trade-off of this detrimental intensity scaling due to the occurrence of tunable (e. g. by changing the gas density or the focusing geometry) spectral regions of 'perfect phase-matching' [53]. Pioneering scaling experiments corroborate these predictions [54–57].

However, generating intense few-cycle pulses in the mid-infrared requires a different laser technology than the conventionally used Ti:sapphire, due to the lack of a broadband laser medium in the mid-infrared wavelength regime. Therefore, one has to resort to a different mechanism for the amplification of intense, few-cycle IR pulses, namely to optical parametric chirped-pulse amplification (OPCPA), which is currently the only technique capable of delivering the desired output parameters. The LWS 1 system at the MPQ is based on this technique, and will be the subject of discussion in section 2.1.

1.4 Free-Electron Lasers

In the following the fundamental principles of undulator radiation generation and some general properties of the SASE process and high-gain FELs are briefly summarized. For an in-depth treatment of these topics and the full derivations of the following equations refer to the extensive review paper by Z. Huang and K.-W. Kim [28] and references therein.

1.4.1 Undulator radiation

The basics mechanism of FELs is the periodic generation of bremsstrahlung from high-energy electrons. This is achieved by accelerating the electrons in

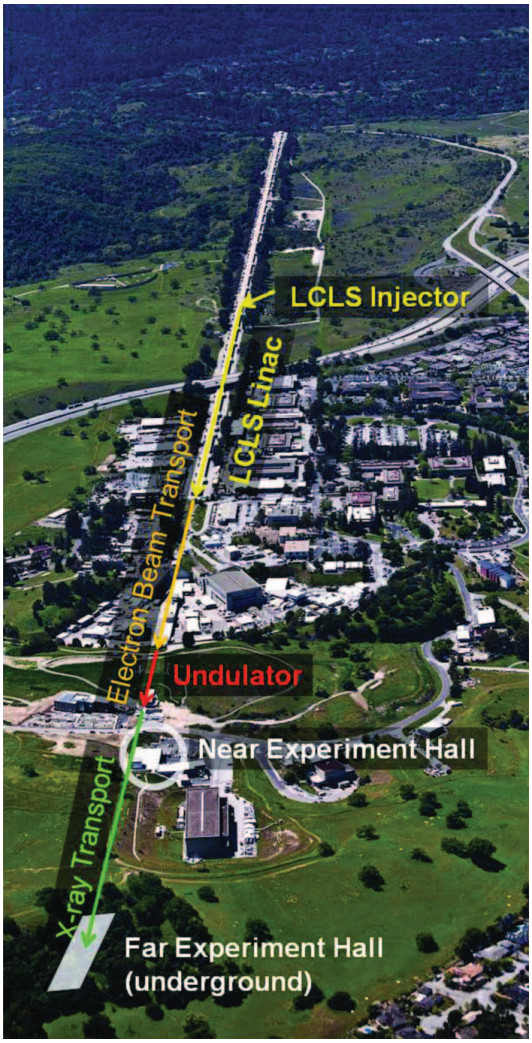

Figure 1.3: The LCLS site at the Stanford Linear Accelerator (SLAC). Depicted are the locations of the 'old' 3 km-long electron accelerator and the newly built electron beam transport tunnel and the undulator hall. Also shown are the near and far experimental areas. (Figure reproduced from reference [58].)

a linear accelerator and coupling the resulting bright electron beam into a periodic magnetic device called an 'undulator' (see Figures 1.3 and 1.4).

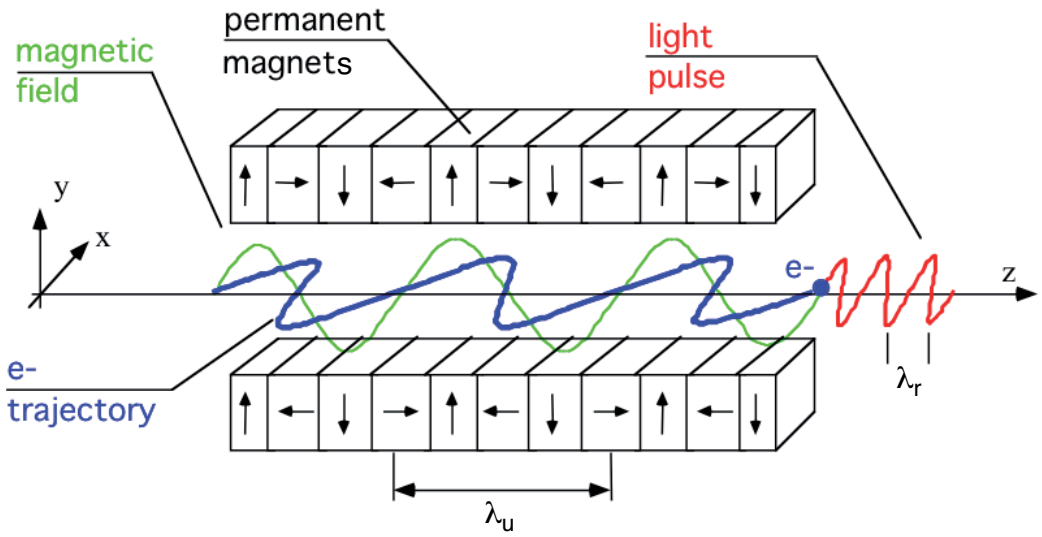

Figure 1.4: Undulator radiation. The alternating magnetic north and south poles are depicted, together with the electron bunch trajectory (red) and the generated light pulse (red).*

The undulator consists of a succession of magnetic north and south poles, so that the electron bunch moving with relativistic velocity along its center in z-direction is deflected via the Lorentz force on an approximately sinusoidal trajectory, thereby emitting electromagnetic radiation in a small cone in forward direction at each period. This light field is polarized along the electron's acceleration vector (x-direction in Fig. 1.4) perpendicular to the propagation direction.

The resonant wavelength of this undulator radiation λ_r is defined by the relativistic electron energy W_e and properties of the undulator device, namely the magnetic pole field B_0 and the undulator wavelength λ_u, via

$$\lambda_r = \frac{\lambda_u}{2\gamma^2}\left(1 + \frac{K^2}{2}\right). \tag{1.10}$$

Here, $\gamma = W_e/m_e c^2$ is the electron energy in units of the rest energy and K

*Figure adapted from the website: Centre Laser Infrarouge d'Orsay, Université Paris-Sud 11, France (`http://clio.lcp.u-psud.fr/clio_eng/FELrad.html`).

is the dimensionless undulator strength parameter

$$K = \frac{eB_0}{m_e c k_u} \approx 0.93 \times B_0[\mathrm{T}] \times \lambda_u[\mathrm{cm}], \tag{1.11}$$

with $k_u = 2\pi/\lambda_u$, and B_0 is the peak magnetic field on the electron propagation axis.

Initially, the sinusoidal motion of the individual electrons is not correlated and the emitted radiation is incoherent so that the generated X-ray power is directly proportional to the number of electrons $P_{X-ray} \propto N_e$.

1.4.2 Self-amplified spontaneous emission (SASE)

As the emitted electromagnetic wave in the forward direction and the electron bunch co-propagate through the undulator, they can interact with each other and exchange energy. This self-interaction is made advantage of for the coherent exponential growth of the X-ray radiation in FELs based on the principle of self-amplified spontaneous emission (SASE) [21, 59]. If the X-ray field is defined by $E_x(z,t) = E_0 \cos(k_{X-ray} z - \omega_{X-ray} t + \phi_0)$, the energy transfer between the electron beam and the undulator radiation can be calculated to

$$\frac{dW_e}{dt} = \vec{v} \cdot \vec{F} = -e v_x(t) E_x(t). \tag{1.12}$$

From eq. (1.12) it follows immediately that the X-rays gain energy from the electrons ($\frac{dW_e}{dt} < 0$) every time the electron propagation vector and the electric field point into the same direction. Since the electrons move with an average speed $\bar{v}_z = c\left(1 - \frac{2+K^2}{4\gamma^2}\right)$ into the forward direction, they are overtaken by the X-ray field moving along with the speed of light c, so that the interaction cannot be sustained in free space. In the undulator, this dephasing can be circumvented, if the X-rays overtake the electrons by exactly one optical wavelength per undulator period, so that the same alignment of the transverse electron velocity component v_x with the emitted electric field E_x is repeated periodically (see Figure 1.5).

This behaviour is ensured by the resonance condition for the undulator, equating the difference of the propagation distance λ_s between the X-ray field and the electrons in one undulator period, the so-called 'slippage length', with

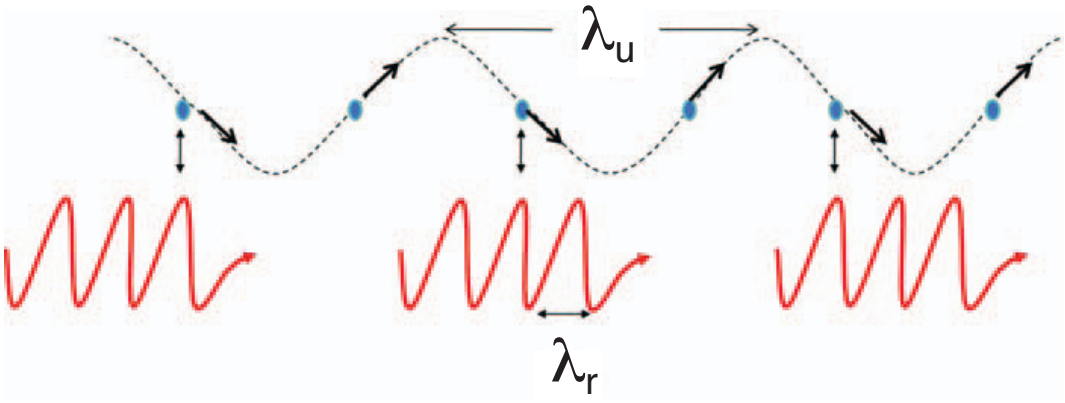

Figure 1.5: Electron–X-ray self-interaction inside the undulator. If the difference of the propagation distance λ_s between the X-ray field (red) and the electron bunch (blue) in one undulator period, the so-called 'slippage length', equals the radiation wavelength λ_r, the energy transfer from the electron bunch to the X-ray beam can be sustained over an extended interaction length. (Figure adapted from reference [58].)

the aforementioned undulator radiation wavelength λ_r (compare eq. (1.10)):

$$\lambda_s = \lambda_r = \frac{\lambda_u}{2\gamma^2}\left(1 + \frac{K^2}{2}\right). \tag{1.13}$$

As one can see from Fig. 1.5, while some electrons will loose energy to the undulator radiation others will always gain energy, depending on the relative phase of the electrons to the plane electromagnetic wave. When the self-interaction is sustained over sufficiently many undulator periods, this leads to a periodic modulation of the electron bunch energy at the wavelength λ_r of the emitted radiation. Thus, accelerated high-energy parts and slowed down low-energy parts of the electron bunch are squeezed together and a periodic electron density modulation starts to develop in the undulator. This process is known as 'microbunching' and is evident as a longitudinal distribution of thin, high-density slices of electrons inside the longer electron bunch, shown in Figure 1.6.

In this way, more and more electrons are radiating in phase at the expense of electron beam kinetic energy, giving rise to a coherent interference of the emitted X-ray radiation and hence to a quadratic dependence of the radiation

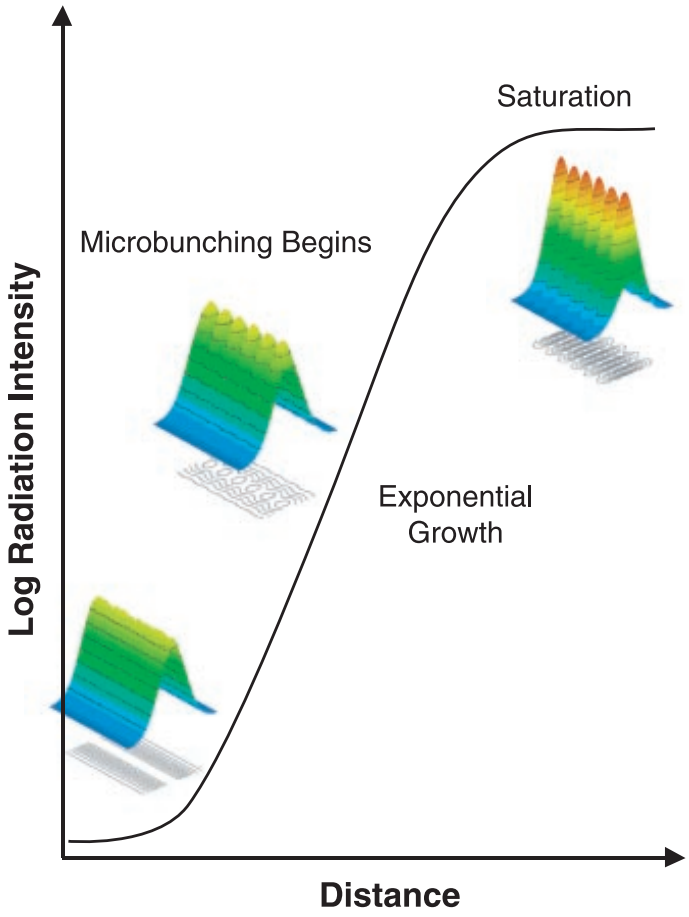

Figure 1.6: Microbunching and exponential gain of the SASE process. The self-interaction of the electrons via the generated X-ray beam leads to a periodic modulation of the electron energy and thus to a periodic density distribution of the electron bunch on the scale of the slippage length λ_s along the propagation direction, a process that is called 'microbunching'. Only the electrons in the same microbunch are emitting X-rays coherently to each other. In this regime the X-ray power grows exponentially until the resonance condition (1.13) is no longer fulfilled and the FEL reaches saturation. (Figure reproduced from reference [22].)

power on the number of electrons $P_{X-ray} \propto N_e^2$. As illustrated in Fig. 1.6, in this high-gain regime the power of the FEL grows exponentially along the propagation distance in the undulator according to

$$P_{X-ray}(z) \propto \exp\left(\frac{z}{L_{G0}}\right), \tag{1.14}$$

until the electron beam has been depleted so much that the resonance condition (1.13) is no longer fulfilled and both the X-ray power and the microbunching reach a maximum saturation level. In equation (1.14) L_{G0} is the monoenergetic power gain length of the FEL, which can be expressed in terms of the undulator wavelength λ_u and the important Pierce parameter ρ:

$$L_{G0} = \frac{\lambda_u}{4\pi\sqrt{3}\rho}. \tag{1.15}$$

The dimensionless Pierce parameter is a characteristic scaling parameter for a high-gain FEL and typically lies in the range of $\rho \sim 10^{-3}$ for short-wavelength FELs using high-energy electron beams.

1.4.3 Characteristics of SASE FEL X-ray pulses

Although FELs share some of their characteristics with conventional optical lasers, like their high intensity, their small spectral bandwidth and their large spatial and expected temporal coherence, there also exist significant differences. The most obvious one is probably the reachable very short wavelengths — down to ~ 1.5 Å at the LCLS — in combination with the ability to easily tune this wavelength and the pulse duration over a broad range according to the experimental requirements. On the other hand, due to the generation principle from self-amplified spontaneous emission, the spectral components of these X-ray pulses can fluctuate from shot to shot constraining measurements sensitive to these changes. For the same reasons, also the pulse duration and the temporal sub-structure of the FEL pulses stemming from the process of microbunching described above vary like the properties of chaotic light [60]. In the following a few FEL properties that are of special interest for the later discussion are briefly described.

Pulse duration & temporal structure

Employing statistical methods one can derive the so-called coherence time t_c, a measure for the duration of the FEL radiation emitted by a single microbunch and thus a coherent ensemble of electrons

$$t_c = \frac{\sqrt{\pi}}{\sigma_\omega}, \tag{1.16}$$

which is inversely proportional to the rms SASE bandwidth σ_ω and generally decreases to about $\sigma_\omega \sim \rho\omega_{X-ray}$ at the FEL saturation point. For hard X-ray wavelengths, where the coherence time determined by eq. (1.16) can be in the range of only a few hundred attoseconds, this is much shorter than the flattop SASE pulse duration T, usually on the same order as the typical electron bunch of tens of femtoseconds, so that $T \gg t_c$ is fulfilled. Then the M parameter, characterizing the temporal mode of the SASE pulse, is defined as

$$M = \frac{1}{\sigma_W^2} = \frac{T}{t_c}, \tag{1.17}$$

and the shot-to-shot pulse energy distribution is approximately given by a Gaussian with a relative rms fluctuation $\sigma_W \sim 1/\sqrt{M}$. These ultrashort, coherent intensity spikes are also roughly spaced by the same interval t_c, which is corroborated by a statistical analysis estimating the average number of intensity spikes per SASE pulse to about $0.7 \times M$ (see Figure 1.7) [61].

Saturation power & saturation length

We have seen that the exponential growth of the FEL power must stop, when the electron beam energy has decreased so much, that the resonance condition (1.13) is no longer valid. Another effect that leads to saturation is the beam energy spread that increases during the electron propagation and eventually inhibits further X-ray amplification. These nonlinear interactions can be studied by a quasilinear theory (see e. g. [62]) and the maximum power be calculated numerically as a function of the initial relative rms energy spread σ_η of the electron beam. An analytic expression for the saturation power of the SASE FEL is provided in the form of a simulation fitting formula [63]

$$P_{sat} \approx 1.6 \left(\frac{L_{G0}}{L_G}\right)^2 \rho P_{beam} = \frac{1.6}{(1+\Lambda)^2} \rho P_{beam}, \tag{1.18}$$

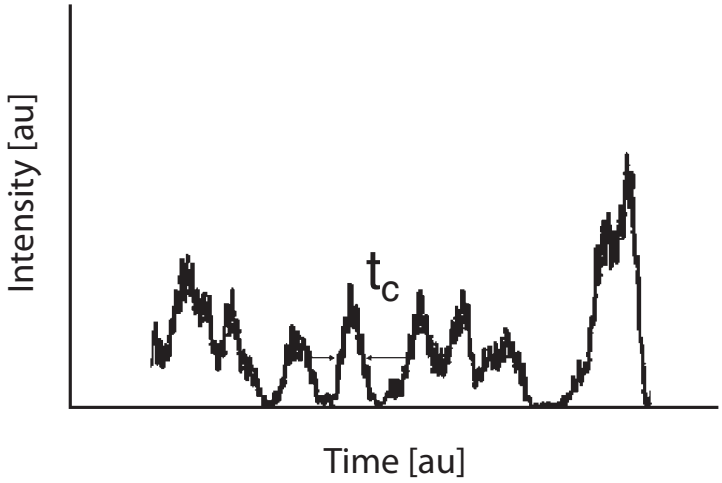

Figure 1.7: Intensity spiking in the time domain. The width and the spacing of the individual peaks is characterized by the SASE coherence time t_c (see equation (1.16)), while the length of the complete SASE pulse is best described by a flattop distribution with duration T, related to the electron bunch length. (Figure adapted from reference [61].)

where the power gain length of the fundamental mode $L_G \equiv L_{G0}(1+\Lambda)$ and the total electron beam power $P_{beam}[\mathrm{GW}] = (\gamma m_e c^2/e)[\mathrm{GV}] I_e[\mathrm{A}]$, with I_e being the electron peak current. Λ quantifies the various degrading effects of the electron beam during propagation along the undulator axis, like diffraction, frequency detuning, beam energy spread and angular spread.

Finally, the saturation distance is given as a multiple of the power gain length of the fundamental mode L_G by

$$\frac{z_{sat}}{L_G} \approx \ln\left(\frac{20 I_e t_c}{e}\right), \tag{1.19}$$

with a numerical factor that depends logarithmically on the number of electrons per coherence time, $N_c = I_e t_c/e$, and typically is close to 20. Setting $L_G \approx L_{G0}$ and taking into account that $4\pi\sqrt{3} \approx 20$, we can substitute equation (1.15) and the saturation length can simply be expressed by $z_{sat} \approx \lambda_u/\rho$.

Chapter 2

Scaling the energy of HHG towards the keV regime

As already mentioned in section 1.3, one way to extend the energy range of high harmonic generation is to use lasers with longer wavelengths as a driving source. A system that provides these longer-wavelength pulses was built up at the Max-Planck-Institute of Quantum Optics (MPQ) in Garching, Germany and will be described in the next section (2.1). This section is based on a condensed version of material to be published as a book chapter by X. Gu et. al. [64]. In section 2.2 the set-up of the experiment will be outlined in some detail and in section 2.3 the measurement results will be presented. Section 2.4 deals with a peculiar feature in the measured high-energy spectra and gives an explanation in terms of direct inner-shell electron excitation, an effect theoretically expected but to our knowledge never previously demonstrated in HHG. The conclusion (sec. 2.5) provides a short summary of the findings, which have been published in Phys. Rev. Lett. by G. Marcus, W. Helml *et. al.* [65]. Parts of this paper are reused for the presentation of the results in this thesis.

2.1 The LWS 1 OPCPA system

Optical parametric amplification (OPA) is physically the same process as difference-frequency generation (DFG), whereby one photon gets divided into two photons carrying the same total energy in a second-order nonlinear optical crystal. In OPA, the initial condition is that a strong pump beam of

shorter wavelength and a weak signal beam of longer wavelength interact in a nonlinear crystal. Through the OPA process, pump photons are continuously converted into pairs of signal photons and difference-frequency 'idler' photons. As a result, the pump energy flows into the signal beam and a new idler beam, whereby the weak signal can be amplified by many orders of magnitudes.

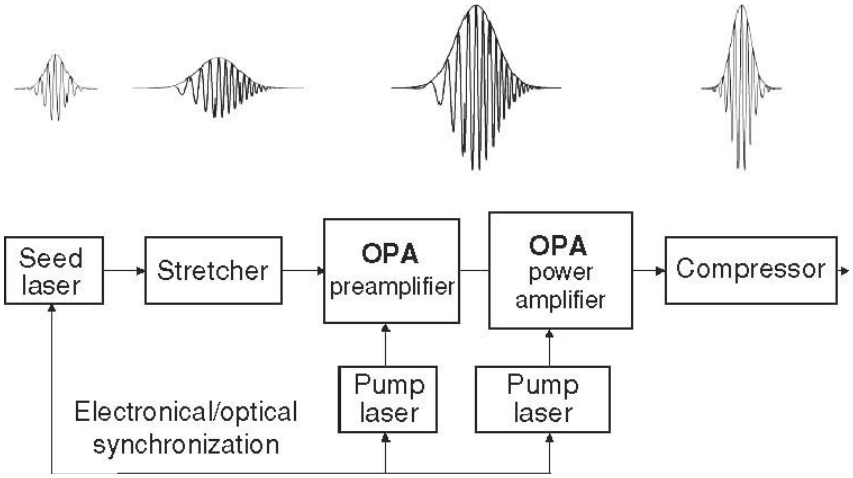

Figure 2.1: Principle of OPCPA. The seed pulse, coming from the lefthand side, is stretched before amplification in one ore more OPA stages. Only after the last amplifier stage the pulse is compressed to reach its final peak power, thereby avoiding deteriorating effects along the beam path due to laser self-interaction in the gain medium or in air. (Reproduced from reference [66].)

OPA can be very efficient. Combined with a temporal stretching of the signal pulse, a technique used in chirped-pulse amplification (CPA), the technology known as OPCPA [67–69] has in recent years become the most promising technique for the amplification of high-energy ultrashort laser pulses, and is so far the only method by which multi-mJ few-cycle pulses are generated [70–73]. Compared to traditional laser amplification, the advantages of OPA/OPCPA include:

- Gain bandwidth: One of the most remarkable properties of parametric amplification is broad amplification bandwidth without substantial gain narrowing.

- Single-pass gain: The single-pass gain achievable in OPA is extremely high, possible to reach even six orders of magnitude.

- Thermal load: The thermal load in OPA is almost negligible. The energy conversion from the pump into the signal and the idler is an instantaneous process. No excess energy is produced or stored in the crystal, which is different from laser amplification.

- Efficiency: High efficiencies can be reached with OPA, up to 25 % in many cases.

- Scalability to high energies: OPA can be scaled to very high pulse energies. With a broader amplification bandwidth, hence a shorter compressed pulse duration, the achievable pulse peak power can be much higher than in a conventional CPA amplifier.

- Versatility to achieve phase-matching: There are several degrees of freedom that can be exploited to achieve broadband phase-matching, including crystal orientation, the noncollinear angle between the pump and the signal, and the spatio-temporal properties of the beams.

- Idler wave: The idler wave can sometimes also be useful, for example, to generate a signal in spectral regions difficult to reach with conventional techniques or to use the idler wave to stabilize the CEP [74–77].

On the other hand, new challenges and disadvantages of OPA compared to the conventional laser amplification include:

- Pump-to-signal synchronization: Amplification takes place only when the pump and the signal are both present. Therefore precise synchronization is required.

- Stretching and compression: Stretching the seed pulse to a fraction of the pump pulse duration is required for efficient energy conversion. In case of a long pump pulse, recompression with a ratio of many orders of magnitude can be difficult to achieve.

- Strict phase matching conditions: Alignment of a parametric amplifier involves numerous factors including the geometry of interaction, pointing stability, pump energy fluctuations, beam collimation, etc.

- Background superfluorescence: The background emission in OPA has a different mechanism compared to the amplified spontaneous emission (ASE) in a solid-state laser amplifier. The background emission in an OPA is created by optical parametric superfluorescence due to spontaneous decay of a pump photon into an idler and a signal photon which is further parametrically amplified.

- Demanding pump beam requirements: The pump beam must have high peak power, a relatively short pulse duration ($\lesssim$100 ps) with a high intensity contrast and a good beam quality.

In the first section, we are going to review some basic factors affecting the amplification gain bandwidth of the OPA process, which is critical for few-cycle pulses. Particularly, two phase-matching configurations will be covered.

2.1.1 Principles of broadband OPA systems

We assume a type I configuration in a uniaxial birefringent crystal, in which the pump is an e(xtraordinary)-wave, and the signal and the idler are o(rdinary)-waves. This is the most common phase-matching situation for OPA applications.

The basic OPA gain formula can be derived from the coupled-wave equations between the pump, signal and idler waves. Neglecting pump depletion, and assuming plane waves and the slowly-varying-envelope approximation [32, 66], we get for the intensity of the signal wave $I_{\mathrm{S}}(L)$ as a function of the interaction length in the gain medium L

$$\frac{I_{\mathrm{s}}(L)}{I_{\mathrm{s}}(0)} = 1 + (gL)^2 \frac{\sinh^2 a}{a^2}, \tag{2.1}$$

where the parametric gain factor g is

$$g = 4\pi d_{\mathrm{eff}} \sqrt{\frac{I_{\mathrm{p}}(0)}{2\epsilon_0 n_{\mathrm{p}} n_{\mathrm{s}} n_{\mathrm{i}} c \lambda_{\mathrm{s}} \lambda_{\mathrm{i}}}}\,, \tag{2.2}$$

$$\text{with} \quad a = \sqrt{(gL)^2 - (\Delta k L/2)^2} \tag{2.3}$$

and

$$\begin{aligned}\Delta k(\omega_\mathrm{p},\omega_\mathrm{s}) &= k_\mathrm{e}(\omega_\mathrm{p}) - k_\mathrm{o}(\omega_\mathrm{s}) - k_\mathrm{o}(\omega_\mathrm{p}-\omega_\mathrm{s}) \\ &= k_\mathrm{e}(\omega_\mathrm{p}) - k_\mathrm{o}(\omega_\mathrm{s}) - k_\mathrm{o}(\omega_\mathrm{i}). \end{aligned} \tag{2.4}$$

Here, the d_eff is the effective nonlinear coefficient and $\lambda_\mathrm{p,s,i}$, $n_\mathrm{p,s,i}$ and $\omega_\mathrm{p,s,i}$ are the wavelength, the refractive index and the angular frequency of the pump, signal or idler wave, respectively. Clearly, the spectral dependence of the gain, i. e. the gain bandwidth, is mostly determined by the spectral dispersion of the phase mismatch factor. While the pump frequency ω_p is basically fixed, the seed frequency ω_s varies over a large range for broadband pulses, and hence Δk can also vary. The maximum amplification is achieved at signal frequency ω_s where $\Delta k(\omega_\mathrm{p},\omega_\mathrm{s}) = 0$, and the OPA gain will remain high only in the region around ω_s where Δk stays small enough. Therefore, for broadband amplification to occur, we need both

$$\Delta k(\omega_\mathrm{p},\omega_\mathrm{s}) = 0 \tag{2.5}$$

$$\text{and} \quad \frac{\partial \Delta k(\omega_\mathrm{p},\omega_\mathrm{s})}{\partial \omega_\mathrm{s}} = 0. \tag{2.6}$$

The first condition can be easily satisfied by choosing an appropriate crystal angle θ, which affects the e-wave k_p. The satisfaction of the second condition at the same time is little bit more complicated and depends on the exact interaction geometry of the signal, idler and pump beams.

In a collinear geometry, in which the signal, idler and pump beams propagate along the same direction, eq. (2.6) implies

$$\left(\frac{\partial k_\mathrm{o}}{\partial \omega}\right)_{\omega_\mathrm{s}} - \left(\frac{\partial k_\mathrm{o}}{\partial \omega}\right)_{\omega_\mathrm{p}-\omega_\mathrm{s}} = 0. \tag{2.7}$$

Obviously, this can be satisfied at $\omega_\mathrm{s} = \omega_\mathrm{p} - \omega_\mathrm{s} = \omega_\mathrm{i}$, or $\omega_\mathrm{p} = 2\omega_\mathrm{s}$. In this case, the signal and the idler have the same wavelength, polarization and propagation; therefore, they are, in principle, indistinguishable. This configuration is called *degenerate OPA*, and it ensures broadband amplification.

If the desired signal center wavelength is not half of the pump wavelength, obviously, eq. (2.6) cannot be satisfied in a collinear geometry, and the amplification bandwidth would be narrow. An additional degree of freedom can be

introduced, however, if we allow the pump and the signal beams to cross with a certain angle. In this case, $\Delta\mathbf{k}$ is defined as the vector difference between the $\mathbf{k}$-vectors of the three waves, and is dependent on both the propagation direction of the pump beam θ and the signal–pump noncollinear angle α.

Differentiating $\Delta\mathbf{k}$ against ω_s in a similar fashion will lead to

$$\left(\frac{\partial k_\mathrm{o}}{\partial \omega}\right)_{\omega_\mathrm{s}} \cos(\alpha+\beta) - \left(\frac{\partial k_\mathrm{o}}{\partial \omega}\right)_{\omega_\mathrm{i}} = 0, \tag{2.8}$$

where β is the angle between the idler and the pump, and can be calculated from α using the relation $k_\mathrm{o}(\omega_\mathrm{s})\sin\alpha = k_\mathrm{o}(\omega_\mathrm{i})\sin\beta$.

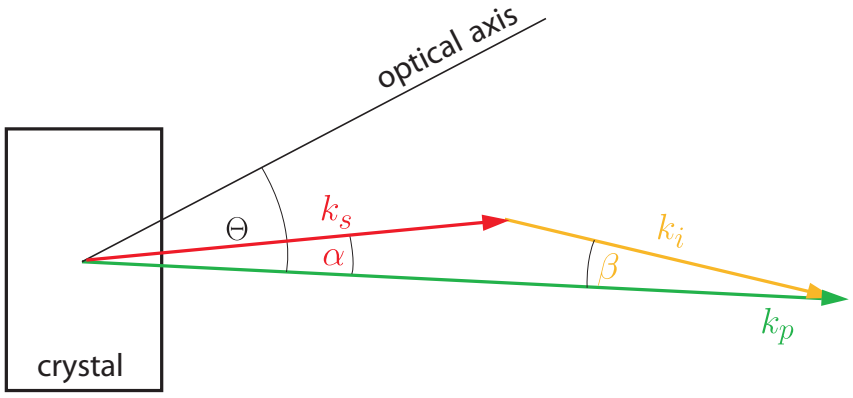

Figure 2.2: Sketch of the noncollinear OPA geometry. (Adapted from reference [78].)

Therefore, by choosing appropriate angles θ and α, one can also achieve a broad OPA bandwidth. This configuration is called *noncollinear OPA* (NOPA), which is widely used in the design of many OPCPA systems [70–73].

For the LWS 1 system to be discussed in this section [79, 80], it was chosen to build a 1053-nm Nd:YLF pump laser [81]. Twice the pump wavelength is 2.1 μm, which is an ideal center wavelength for the infrared OPCPA system. The design slightly deviates from the true degenerate configuration, in that the signal and the pump are not perfectly collinear, but cross at a very small angle. The angle difference allows to easily separate the signal and the pump beams after the OPA crystals, and avoid signal-idler interference which might disturb the signal pulse profile. The deviation from the degenerate condition is small, and the broad bandwidth is therefore not affected.

2.1.2 Infrared seed & and high-energy pump pulse generation

To achieve the necessary high-precision and reliable synchronization between the seed and the pump pulse in the OPCPA, in this system we rely on the scheme of all-optical seeding, using the same Ti:sapphire laser source as the front end for both the seed and the pump pulse generation. The schematic of the LWS 1 OPCPA system is shown in Fig. 2.3. The design and performance of the system will be discussed in the following sections.

The broadband infrared seed pulse

The creation of the broadband infrared seed pulse for the OPCPA system is accomplished by means of intrapulse difference-frequency generation (DFG) or optical rectification in a periodically poled lithium niobate (PPLN). This design automatically ensures CEP stability, which is further on preserved in the OPA process, and is of vital importance for many applications which rely on few-cycle pulses, especially for the efficient generation of high-energy, broadband cutoff harmonics, which can support attosecond pulses.

The front end of our system consists of a commercial 1-mJ, 25-fs 3-kHz Ti:sapphire multipass amplifier (Femtolasers Femtopower Pro). Five percent of the Femtopower system output are first spatially clipped by an iris, reducing and fixing the pulse energy to 12.3 μJ, and then focused into a gas cell filled with 17 bar of krypton, where the pulse creates a single filament and its spectrum is broadened by self-phase-modulation (SPM) to cover a spectral range from $\sim$600 to $\sim$950 nm. The pulse energy and the iris size are chosen such that the filament's output spectrum is as broad and smooth as possible without breaking into unstable multiple filaments. The white-light beam is then reflected four times on home-made bandstop mirrors, which are designed to remove the strong components between 750 and 850 nm from the reflected beam and have flat dispersion and uniform reflectivity in the spectral regions below 750 nm and above 850 nm (see Fig. 2.4). The pulse after the bandstop mirrors are then temporally compressed by a set of home-made chirped mirrors. The pulse is afterwards focused into a 1-mm-long 11.21-μm-period MgO-doped periodically poled $LiNbO_3$ crystal (MgO:PPLN), where the long-

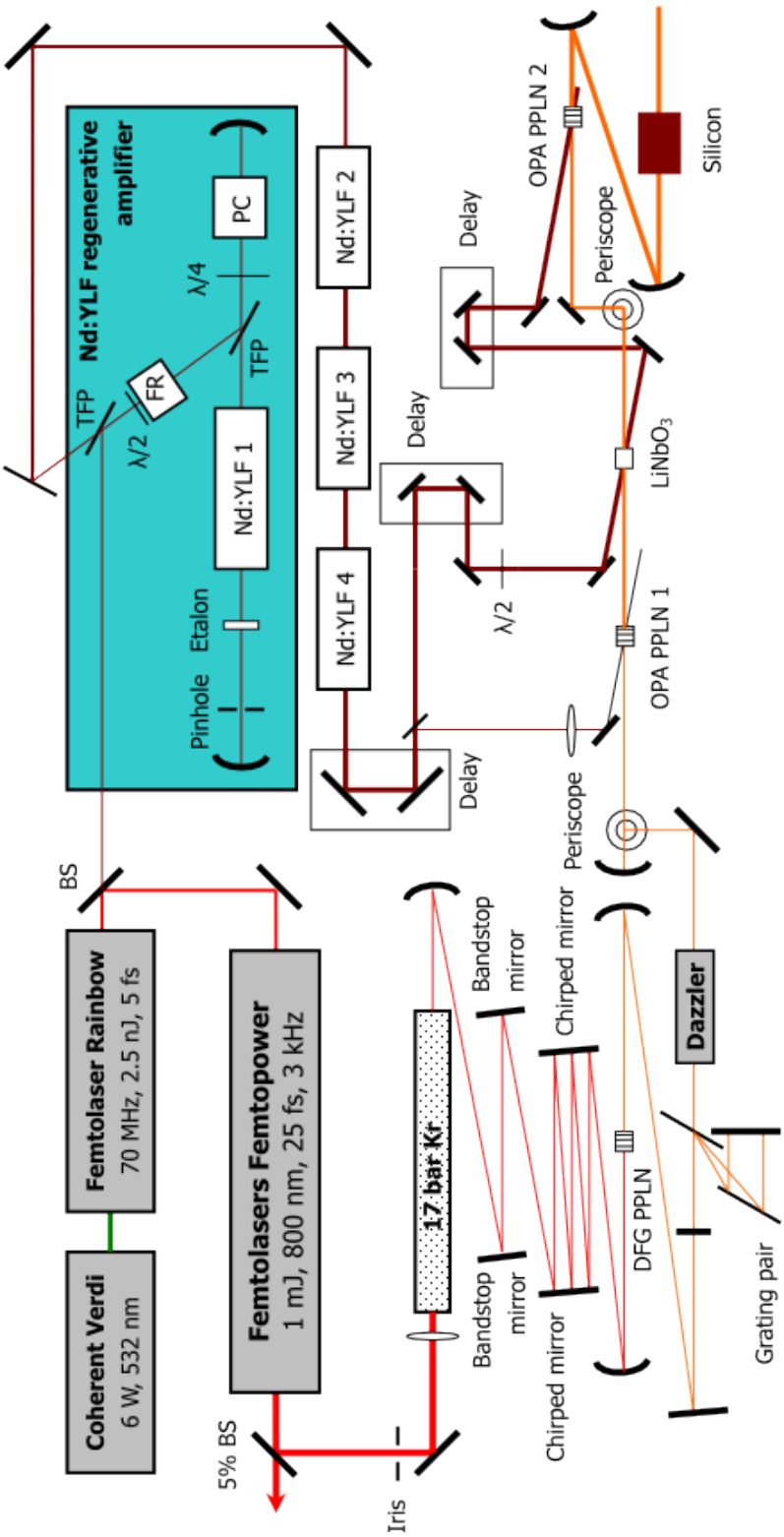

Figure 2.3: Schematic of the LWS 1 mid-IR OPCPA system. A description of the system is given in the text.

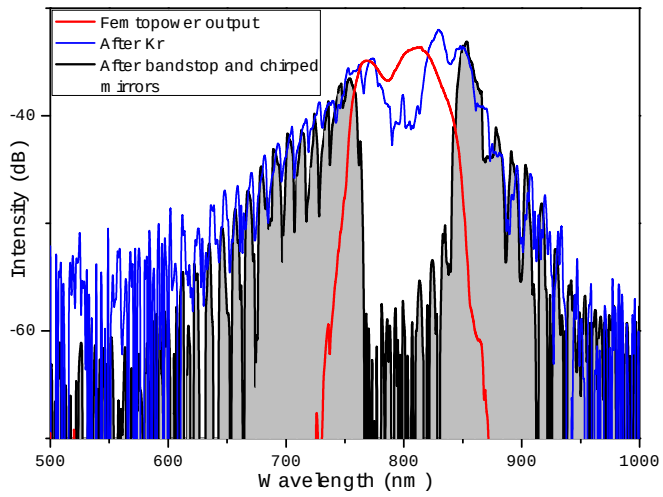

Figure 2.4: Spectra of the Femtopower Pro laser system output pulse (red), the spectrally broadened pulse after the krypton cell (blue), and the pulse after the bandstop and chirped mirrors (black).

and short-wavelength components are mixed, generating a difference-frequency signal extending from 1.7 to 2.6 μm.

This mechanism satisfies two important requirements for an OPCPA seed source. First, with an appropriate nonlinear crystal, 2-μm radiation can be acquired even more easily than 1.4 μm, because it requires less bandwidth from the fundamental radiation. Secondly, the CEP of the infrared signal generated by intrapulse DFG is automatically stabilized, regardless of the CEP stability of the fundamental pulse [74–77]. The mechanism can be easily understood by recognizing the fact that all the components in the fundamental pulse carry the same CEP, and the infrared DFG pulse has a CEP which is the difference between the long- and short-wavelength components in the same fundamental pulse. Therefore, even though the fundamental pulse's CEP may be random from shot to shot, the DFG pulse's CEP does not change, and is only defined by the envelope of the fundamental pulse. The stable CEP of the infrared seed pulse will in principle also be preserved in the OPA processes, regardless of the CEP stability of the pump pulse. This is very important for the use of few-cycle laser pulses as a driver for HHG or other highly nonlinear processes, where CEP plays a central role in determining the electric field of the pulse.

The resulting nJ-level, CEP-stable broadband infrared seed is then used as the seed for our OPCPA system.

The Nd:YLF high-energy pump laser

To achieve mJ-level infrared output pulses from the OPCPA system, one principal challenge is the design and build-up of a picosecond pulse pump laser capable of delivering pulse energies of tens of mJ at kHz repetition rates. For the LWS 1 IR system these pump pulses are generated by a 49-ps, 13-mJ Nd:YLF amplifier chain, consisting of a regenerative amplifier and three linear post-amplifiers, all developed in house [81].

The regenerative amplifier is seeded by the Ti:sapphire oscillator (Femtolasers Rainbow) contained in the Femtopower front end described in the previous section, and is operated at 1 kHz. The oscillator spectrum is specially tuned so that its spectrum extends just beyond ~ 1060 nm [44]. The infrared part of the oscillator output, measuring ~ 10 pJ within the fluorescence bandwidth, is split off by a dichroic mirror, and sent as the seed into the Nd:YLF regen amplifier, which features a Northrop-Grumman laser module containing a 80-mm-long 4-mm-diameter a-cut Nd:YLF rod. This optical seeding scheme ensures that excellent synchronization is maintained between the seed and pump pulses of the OPA, which is of great importance for the stability and reliability of the system [82]. The infrared pulse is amplified up to 3.5 mJ after ~ 40 round trips in the cavity, at which point it is ejected out of the cavity by Pockels cell switching.

Three single-pass Nd:YLF amplifier modules are used to further amplify the regen output. These amplifiers each contain a 120-mm-long a-cut Nd:YLF rod crystal, with 4 or 5 mm diameter, and are continuously pumped by laser diode arrays. The design with alternating orthogonal polarization of the amplified beam is chosen specifically to compensate for the elliptical thermal lensing of the Nd:YLF crystal. Most importantly, delicate balance must be achieved between thermal lensing and self-focusing in these crystals, in order to extract maximum amplification without damaging the crystals. To this end, appropriate lenses are placed between the stages to optimize the beam size and divergence in these amplifiers and maintain a high-quality beam profile. After the three post-amplifiers, an output energy of 13 mJ with a pulse energy

stability of 1.2 % rms is obtained. The FWHM pulse duration, assuming a Gaussian pulse shape, is 49 ps, with an intensity contrast ratio between the peak of the amplified pulse and the ASE floor determined to be $\sim 10^3$. These pulses are therefore ideal for pumping the IR OPCPA system.

2.1.3 Stretcher & compressor design

OPA being an instantaneous nonlinear process, energy transfer from the pump pulse to the seed pulse can occur only when and where both pulses overlap. Since the pump pulse is much longer than the seed pulse, the seed pulse must be first temporally stretched to a significant fraction of the pump pulse duration, in order to achieve maximum amplification efficiency. After amplification it has to be recompressed back to its Fourier limit as closely as possible. Therefore, the design of the stretcher and the compressor must allow, first of all, the required stretched pulse duration, and secondly, the cancellation of not only the GDD but also the high-order phases in the final compressed pulse.

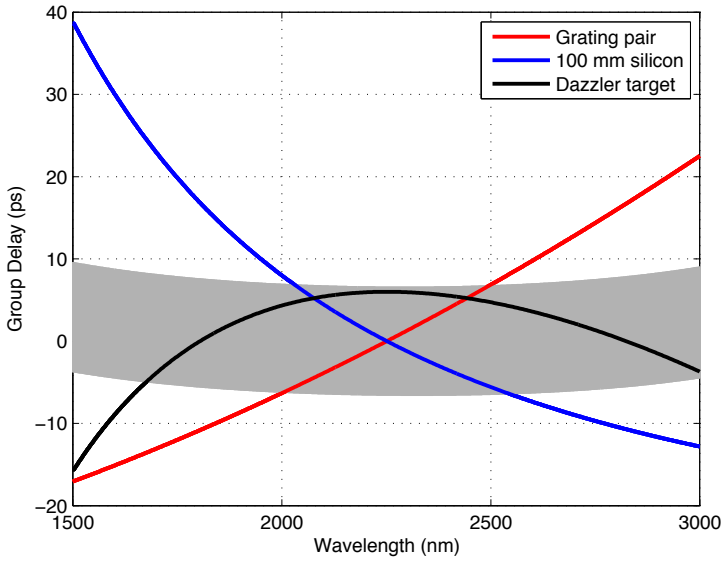

Figure 2.5: Calculated GD curves for the grating pair (red), silicon compressor (blue) and the target GD to be realized by the Dazzler (black). The gray shaded area represents the tuning range of the Dazzler.

Traditional CPA systems typically use a positively dispersive bulk material as the stretcher, and a prism/grating pair as the compressor. For the LWS 1

system positively dispersive AR-coated bulk silicon substrates are used as the compressor, which has a higher transmission throughput and faciltates easier alignment than a grating compressor. For the stretcher, we use a pair of 300 lines/mm gratings separated by 75 mm, and a Fastlite Dazzler specially designed for the infrared spectral range. The use of the Dazzler, an acousto-optic pulse shaper, allows for fine compensation of arbitrary phase profiles within its tuning range.

The design group delay (GD) curves of the grating pair and the silicon compressor, the phase to be compensated and the Dazzler tuning range are all shown in Fig. 2.5. As one can conclude from the GD presented in the figure, the infrared seed pulse between 1.8 and 2.7 μm is stretched to 26 ps after the grating pair and the Dazzler (which corresponds to a dispersion of roughly the same amount, but with opposite sign, as that introduced by the silicon blocks), and the phase to be compensated by the Dazzler falls well within its tuning range. Fine tuning of the dispersion can be achieved by measuring the phase of the compressed pulse, and feeding back the opposite of the measured phase to the Dazzler, accordingly.

2.1.4 OPA design & parametric superfluorescence

For our system pumped by 1037-nm pulses, degenerate OPA provides a broad bandwidth around 2.1 μm. Experimentally, the signal and the pump beams are arranged to cross with a small angle ($\sim 3°$) in the OPA crystals, to allow for easy separation of the beams and to avoid signal-idler interference.

OPA design

The best crystal transparent in the whole spectral range of interest and providing the highest second-order nonlinear coefficient is lithium niobate ($LiNbO_3$). Pumped at 5 GW/cm^2, a 6.5-mm-thick MgO-doped LiNbO3 crystal cut at 42.9° can support a small-signal-amplification bandwidth from 1.8 to 2.5 μm, sufficient for a sub-3-cycle pulse. Even better, periodically poled LiNbO3 (PPLN) crystals can provide the same amplification with a shorter crystal length, and therefore a broader amplification bandwidth.

The phase mismatch in a PPLN can be calculated by adding a quasi-phase-

matching (QPM) term to the usual definition

$$\Delta k = k_{\mathrm{p}} - k_{\mathrm{s}} - k_{\mathrm{i}} - \frac{2\pi}{\Lambda}, \tag{2.9}$$

where Λ is the poling period. The OPA gain calculation is the same as described in eq. (2.1).

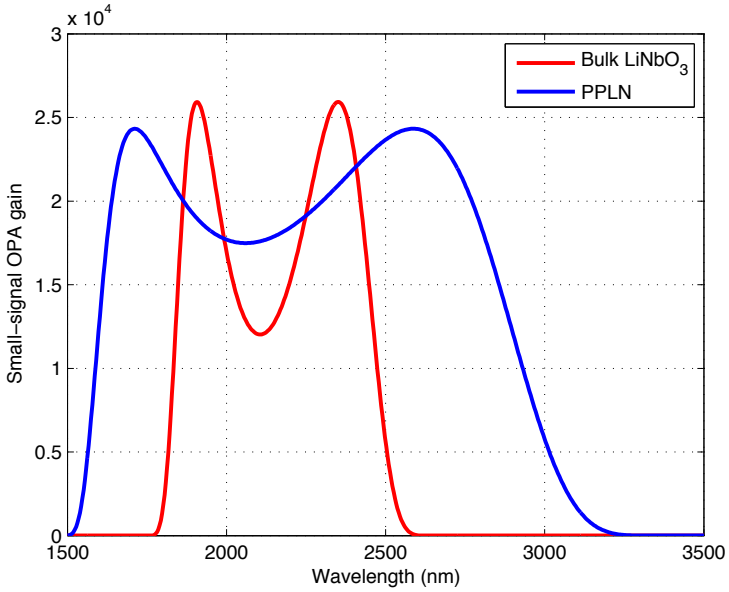

Figure 2.6: Calculated small-signal OPA gains for a 6.5-mm-long $LiNbO_3$ cut at 42.9°(red), and a 1.9-mm-long 30.3-μm-period PPLN (blue), both pumped at 5 GW/cm^2.

The calculated small-signal OPA gain curves are shown in Fig. 2.6. Clearly, PPLN supports a broader amplification bandwidth than bulk $LiNbO_3$, and therefore is the crystal of choice for our broadband IR OPCPA system. However, a practical problem with PPLN is its limited available size. Therefore, for the OPCPA system, a 3-mm 30.2-μm poling period PPLN is chosen for the first OPA stage, where a nJ infrared seed pulse is amplified to $\sim$3 μJ. In the second and third OPA stage, 4-mm-thick bulk LiNbO3 crystals are used.

The first and the second OPA stages are pumped by 3 % and 97 % of the 13-mJ 1053-nm pulses, and the pump beam after the second OPA stage is reused for pumping the third OPA stage. The amplified signal beam is finally sent through a 100-mm-long silicon block for compression. The OPA system output, including possible superfluorescence, is 6 μJ after the first stage, 200 μJ

after the second stage, and 920 μJ after the third stage. The energy stability of the third-stage output is 9 % rms.

Parametric superfluorescence

In general, high-gain OPA systems have an inherent problem of background superfluorescence, and our system is no exception. To resolve this important but difficult issue, we have employed a novel method of spectral shaping of the seed pulse. In the absence of superfluorescence, any shaping of the IR seed spectrum by the Dazzler will be directly transferred to the amplified signal. In particular, if we annihilate a narrow region in the seed spectrum (or create a zero-reaching spectral 'hole') using the Dazzler, the real amplified seed will preserve the spectral hole with a 100 % modulation depth. Broadband parametric superfluorescence, on the other hand, is not shaped and its level unchanged if the hole is narrow enough. Therefore, in the combined spectrum, the spectral hole will be partially refilled by the superfluorescence. By measuring the depth of the spectral hole at different wavelengths across the spectrum, we can trace out the superfluorescence spectral distribution relative to the full OPA output and determine how much energy is in the superfluorescence and in the amplified signal, respectively.

We have used this simple method to measure the superfluorescence in our OPA system output, and the result is presented in Fig. 2.7. From this measurement, it is clear that out of the total 920 μJ third-stage OPA output, 740 μJ (80 %) belongs to the amplified seed and the rest (20 %) belongs to the superfluorescence. In comparison, the superfluorescence is negligible in the first-stage OPA output, and accounts for 2.5 % of the second-stage OPA output.

2.1.5 OPCPA system output & pulse characterization

The final compressed output pulse of the OPCPA system is characterized by a third-harmonic-generation (THG) frequency-resolved optical gating (FROG) apparatus [83]. The third-harmonic signal is generated on an air–CaF_2 interface, which possesses a large bandwidth sufficient to cover the full spectrum of the amplified IR signal. A home-written FROG retrieval code is used to

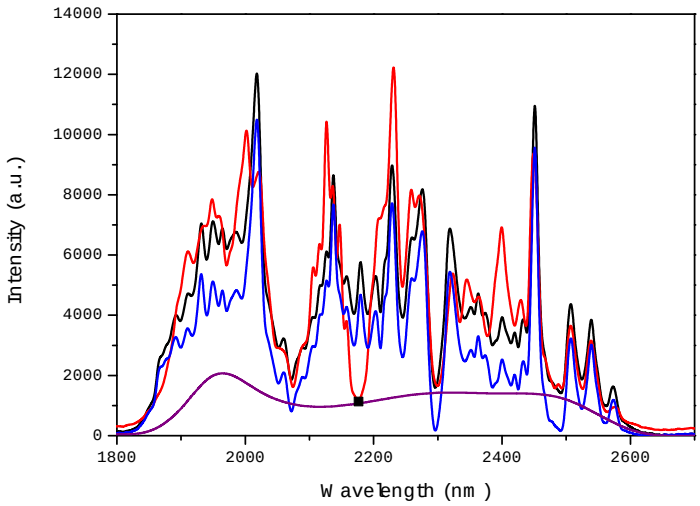

Figure 2.7: Spectra of the full third-stage OPA output (black), the OPA output with a 50-nm-wide Dazzler-imposed spectral hole at 2150 nm (red), the superfluorescence profile traced out by hole depths at different wavelengths (magenta), and the true amplified signal (blue, the full OPA output minus the superfluorescence). The black square denotes the measured level of superfluorescence at 2150 nm by the spectral hole technique.

retrieve the pulse intensity and phase from the measured THG FROG trace. Several iterations are employed to make fine spectral phase corrections with the Dazzler using the result of the FROG retrieval algorithm, ultimately bringing the compressed pulse to approach the Fourier-transform limit as closely as possible. The THG FROG measurement results of the final compressed pulse are presented in Fig. 2.8. The temporal intensity profile of the compressed pulse measures a FWHM of 15.2 fs, which is very close to the Fourier limit of 14.6 fs. At 2.1 μm, this pulse duration corresponds to merely 2 optical cycles. This is, to our knowledge, the shortest sub-mJ-level pulse ever generated at this wavelength.

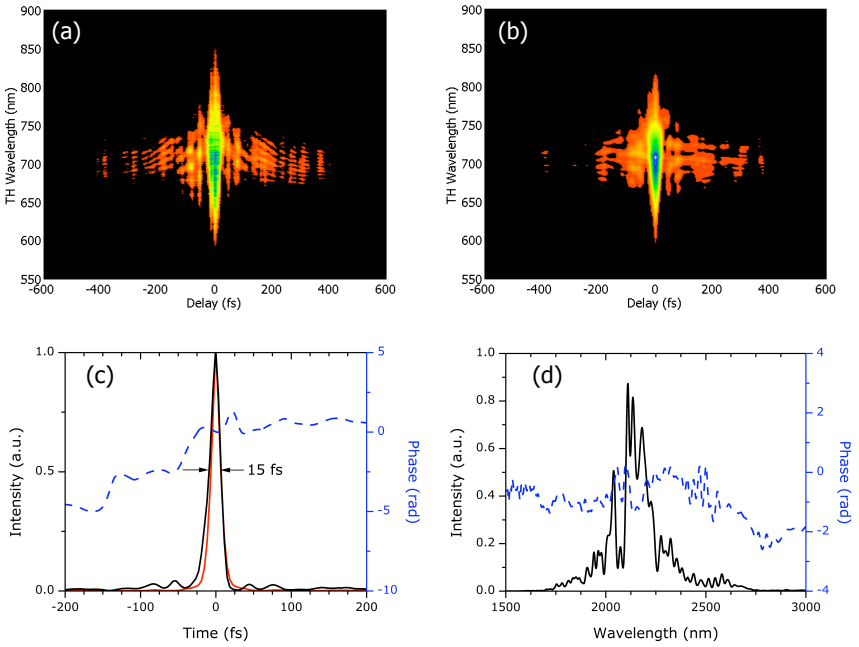

Figure 2.8: THG FROG measurement results of the compressed 15-fs pulse. (a) Measured FROG trace, (b) retrieved FROG trace, (c) temporal intensity and phase, (d) spectral intensity and phase. The black and the red curves in (c) are the measured and the ideal Fourier-limit intensity profiles, respectively.

The compression ratio of 25 ps to 15.2 fs and the amplified signal to superfluorescence energy ratio of $\sim 2:1$ means that the intensity contrast between the compressed amplified signal pulse and the parametric superfluorescence is larger than 10^3, which should be sufficient for a high-quality HHG experiment.

The CEP stability of the final output of the OPCPA system has been further verified in an f-to-3f nonlinear interferometer measurement [80] (see Fig. 2.9).

The spectrally broadened fundamental 2.1-μm light and its third harmonic are interfered in a spectrometer in a spectral region near 700 nm, resulting in spectral fringes whose positions indicate twice the CEP of the fundamental 2.1-μm light. This measurement experimentally confirms the preservation of the CEP stability of the infrared laser system output, which is very important for CEP-sensitive experiments.

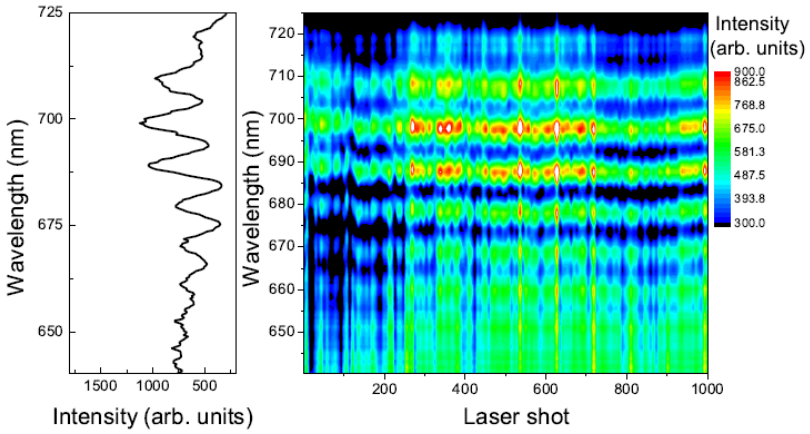

Figure 2.9: CEP measurement of the OPCPA output pulse. Left: a single-shot f-to-3f interferogram; right: Interferograms measured in 1000 consecutive shots.

The LWS 1 IR system generates CEP-stable 2.1-μm ∼700-μJ, 15-fs pulses at 1 kHz [79, 80]. With pulses spanning only about two optical cycles, this laser is unique in the world, providing the shortest sub-mJ pulses in the mid-infrared. This OPCPA system is therefore a perfectly suited driver for keV HHG and a range of other exciting experiments.

2.2 Experimental set-up — the beamline AS 4

2.2.1 The high harmonic generation set-up

To make work on the measurements as independent as possible from any alignment procedures of the laser system, there are two distinct areas in our laboratories dedicated to either experimental or laser related activities. As it is, the laser laboratories are located on the first floor of the building, while all of

our experiments with the IR laser source described above were conducted on the ground floor level. This layout makes it necessary to construct an optical guiding from the output of the OPCPA to the area where the actual measurements take place. Since we are using very short pulses and dispersion in air is not to be neglected, even for the long wavelength we are working at (1 m in air amounts to about 8 fs^2 GDD), all of this beam transport has to be done inside vacuum tubes. Therefore, a prerequisite for a successful experiment is the build-up of a suitable beamline. Figure 2.10 shows an outline of the so-called beamline AS 4 (AttoSecond 4).

Inside the HHG chamber the IR laser is temporarily compressed in a block of silicon with AR coated entrance and exit surfaces and subsequently focused into the gas target by a commercially available CaF_2 lens into the gas target. The pulse length can be determined in situ by way of a home-built THG FROG [83]. The measured dispersion (up to the fourth order) is fed back into the settings for a DAZZLER to precompensate for the detected chirp. This process is then run through for several times, with every feedback loop compressing the IR pulse yet further, until the shortest pulse duration reachable with the given laser spectrum is accomplished.

In our experiments, ensembles of neon atoms (Ne) and nitrogen molecules (N_2) were exposed to 17 fs, 350 μJ, few-cycle laser pulses carried at a wavelength of 2.1 μm from the LWS 1 system described in the previous section. At the wavelength of 2.1 μm this corresponds to roughly two full cycles of the optical carrier field with a period of ~ 7 fs. Since the kinetic energy of the recolliding electron is proportional to the ponderomotive energy $U_p \propto I\lambda^2$ (compare section 1.3), the long carrier wavelength together with the short IR pulse consisting only of a few oscillation periods allow the production of recolliding electrons with kinetic energies at the 1-kiloelectronvolt-level and above, easily exceeding the K-shell binding energy of Ne ($\sim$870 eV) without excessive ionization of the gas [51, 84].

The laser beam was focused with a $f = 250$ mm CaF_2 lens to a spot size of ≈ 35 μm FWHM, measured by a knife-edge scan. The interaction between the laser beam and the gas takes place within a nickel tube with an inner diameter of $\sim$2 mm. The best harmonic yield was achieved when the laser was focused ~ 350 μm before the center of the tube, in agreement with previous HHG

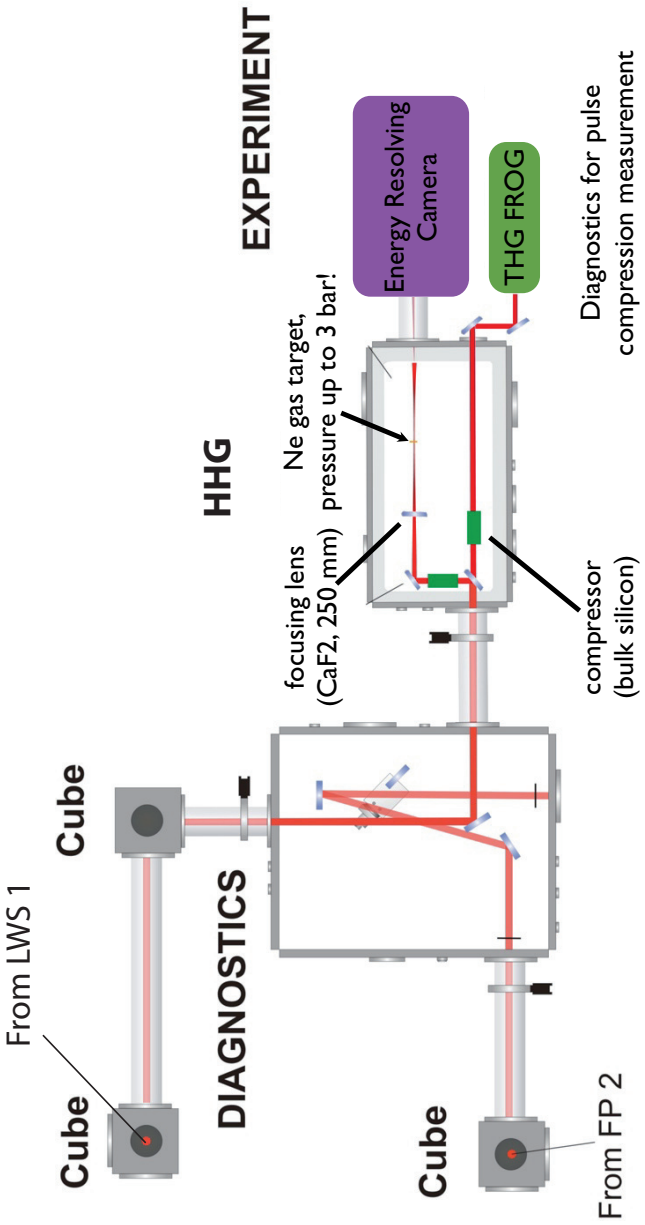

Figure 2.10: Outline of the beamline AS 4 at the MPQ. The laser enters through cube 1 (marked as 'from LWS 1') from above and is guided to the switch box, where it can be further deflected into multiple vacuum chambers for different experiments. In the case of the described measurement, the IR laser was sent to the HHG chamber to the right, where the high harmonic process took place. For the characterization of the pulse duration of the fundamental a THG FROG was set up, the generated soft X-ray radiation was detected with an energy-resolving camera at the chamber exit to the far right.

experiments [85]. The laser drills transverse holes into the thin tube walls, the diameters of which are precisely matched to that of the beam, minimizing gas load to the surrounding vacuum. The tube is fed continuously with the target gas and mounted on a three-axis translation stage.

2.2.2 High harmonic detection with the pnCCD camera

To measure the energy spectrum of the soft-X-ray emission from both the coherent HHG process and the incoherent spontaneous decay of the excited atoms the generated radiation is recorded by a specially designed pnCCD camera (PNSensor GmbH) [86, 87] consisting of 264×264 pixels, each being an independent energy-resolving X-ray detector. Since the resolution of this kind of cameras is low at sub-keV photon energies, it is the first time that such a detector has been used for the characterization of HHG. The layout of the pnCCD is illustrated in Figure 2.11. The whole chip is divided into an image area (in the centre) and an X-ray opaque frame storage area (split in two parts on both sides of the chip). This architecture allows to shift the signal accumulated on the image area during the measurement very fast ($\lesssim 30$ µs) to the two outer storage parts, where it can be processed while the cleared image area is already recording the data for the next measurement cycle.

Each storage area is again split up into two independent parts of 132 rows, that are read out one by one and are then amplified by a dedicated CAMEX (CMOS Amplifier and MultiplEX) chip in parallel before the data is sent to the analog-to-digital converters. In this way the chip read-out is very fast while at the same time maintaining a high signal-to-noise ratio, in principle facilitating measurements with kHz acquisition rates. Since for our experiments the flux of high harmonics with keV energies is expected to drop quite dramatically, we always integrated the recorded signal for at least some seconds, so that this ultrafast read-out feature of the pnCCD camera was not relevant for the data acquisition at the current settings.

The energy resolution of the pnCCD camera is about 12 %, limited by the Fano factor of silicon. Usually, energy resolving detectors are working in a single photon detection mode, but in the case of this array of detectors this limitation is relaxed and is limited to about 5×10^3 photons/pulse hitting the entire area of the CCD. To this end, metal filters were inserted into the high

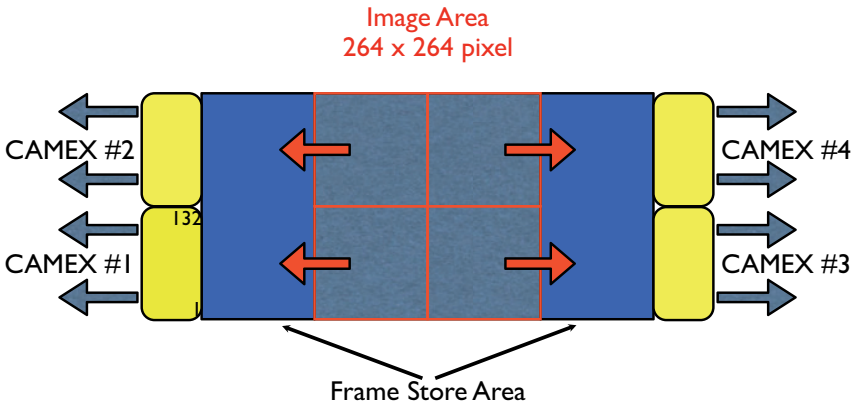

Figure 2.11: Layout of the pnCCD camera chip. The whole chip is divided into an image area and a frame storage area. This architecture allows data acquisition with kHz repetition rates, while simultaneously maintaining a high signal-to-noise ratio.

harmonic beam to suppress the fundamental laser light and to reduce the X-ray photon number to an appropriate level for the detector. The principle of operation of the pnCCD camera is similar to that of gas ionization chambers or silicon drift detectors (SDDs), where the number of electrons generated in the device is linearly proportional to the energy of the X-ray photon. Assuming that only a single photon hits the detector at a given time, one can deduce the photon energy by counting the number of generated electrons. The pnCCD is a back-illuminated CCD which uses a fully depleted substrate where each pixel serves as an energy-resolving detector, thereby providing the ability to measure both the energetic and spatial distribution of the radiation at the same time. When an IR or visible photon hits the pnCCD chip, it generates just one electron per photon, but at wavelengths below 300 nm the number of created electrons in the silicon bulk becomes proportional to the photon energy (see [87]). Therefore, below this wavelength the pnCCD works as an energy-resolving detector. At wavelengths above 1100 nm silicon becomes transparent and the camera is practically blind in this spectral range [88, 89].

In addition this architecture allows to work at higher photon fluxes than with a single-element SSD. As was mentioned before, with energy resolving devices one has to make sure that only one photon hits the detector for every read-out cycle. That means that the photon flux should be lower then

1/(detector area × integration time). In the pnCCD camera this limitation is mitigated by reducing the detector area to the size of about 3 x 3 pixels, whereas at the same time the number of detectors is increased. In this way, it is possible to expose the detector to higher fluxes without sacrificing the photons collection efficiency.

Another advantage is the ability to reduce noise and data-interpretation errors by using events statistics and events correlations. Figure 2.12 is a schematic drawing showing typical recorded events on the pnCCD chip. Because the pixel size is small (compared to a SDD for example), a portion of the charge that is created in one pixel may in some instances diffuse to the neighbouring pixels. So a single photon may appear sometimes as a single pixel (circles A and B) and sometimes cover two (C), three (D) or even four pixels (E). Accordingly, these events should be counted as stemming from one single photon and the respective electron currents should be added up to correctly determine its energy. I will show in the next section with the help of a measured spectrum how often these kind of multi-pixels events are detected and how to cope with them so as not to unduly distort the deduced photon energy distribution. Events (F) and (G) in figure 2.12 are rejected and not considered as a single-photon event, as it is unlikely to get such a charge distribution if the charge diffuses from one pixel to its neighbours. Events such as (G) are usually created by cosmic-ray particles. Events like (F) might be caused by two photons hitting the detector near to each other. In the case of events like (F) it is easy to reject these events and not include them in the spectrum.

2.3 HHG in the keV regime

An image of the generated high harmonic beam can be seen in Fig. 2.13. The camera was situated ∼60 cm away from the gas target and was shielded from the IR fundamental laser by 500-nm-thick metal filters to avoid damage of the CCD. The alignment with a 'real' IR laser (as compared to the widely used 800 nm NIR driver lasers) is a meticulous task, since the beam position and shape can only be seen by the human eye with the help of slowly-responding thermo-responsive sheets or the cumbersome set-up of IR cameras in the beam path, so that is is hard to center the generated XUV beam perfectly on the

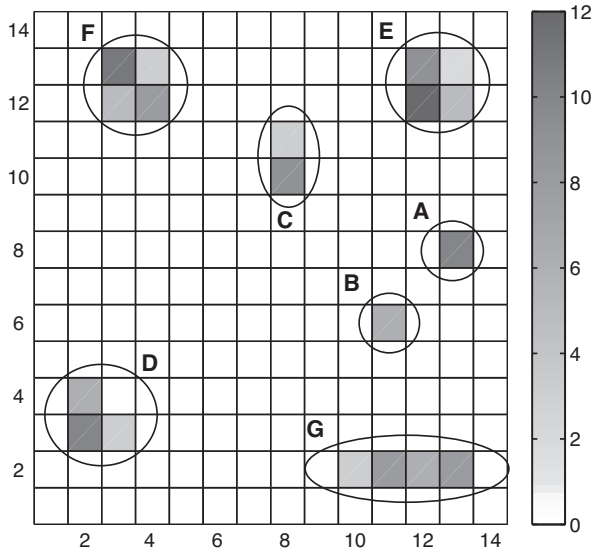

Figure 2.12: Schematic drawing of recorded events on the pnCCD sensor. A detailed description of the contributions of the different sketched pixel formations to the accumulated spectrum is given in the text.

CCD.

Figures 2.14(a) and 2.14(d) show typical spectra obtained with Ne through a 500 nm aluminum filter and with N_2 through a 500 nm magnesium filter, respectively, under identical conditions of laser irradiation. For the calibration of the spectrometer we inserted thin vanadium and iron filters (see Figs. 2.14(b) and (c)). Compared to the spectrum transmitted only through the aluminum filter (Fig. 2.14(a)), a clear cut at the L-edges of vanadium and iron in the filtered spectra can be observed.

Qualitatively, the spectra for Ne and N_2 look similar: both exhibit a plateau, extending up to the K-edge of the target atom (~ 870 eV for Ne, ~ 410 eV for N_2), followed by a long tail after a sharp drop at the K-edge. For Ne exposed to a laser peak intensity of $\sim 1.2 \times 10^{15}$ W/cm^2, this tail extends up to approximately 1600 eV, in agreement with the theoretically predicted cutoff harmonic energy $E_c = I_p + 3.17\,U_p$ [38], where I_p is the ionization potential of the target gas. Thus, we have demonstrated the scalability the of achievable photon energy for HHG with the driver wavelength, increasing the cutoff by roughly an order of magnitude when using a 2.1 µm-laser compared to the

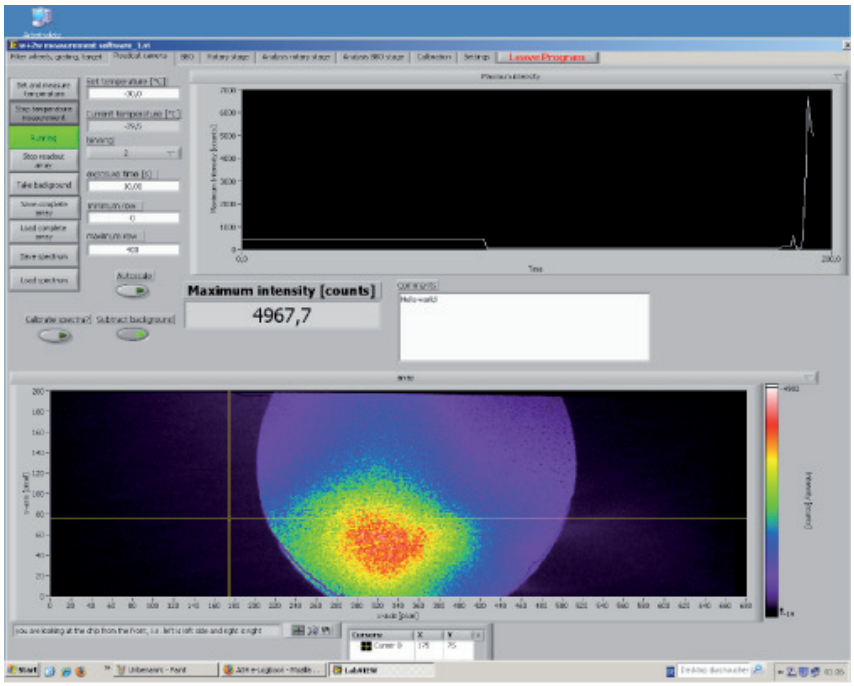

Figure 2.13: Image of the high harmonic beam generated by a 2.1-μm-driver laser recorded by a conventional XUV CCD (PIXIS-XO, Princeton Instruments). The hamonics were generated in neon gas at a pressure of ∼840 mbar and the beam was filtered by a 500-nm-thick zircon foil to get rid of the co-propagating fundamental IR pulse.

typical cutoff of $\lesssim$ 150 eV, reported with driving fields at 800 nm fundamental wavelength and with the same intensities on target.

Interestingly, in spite of negligible absorption, the HH spectrum of N_2 does not extend up to the predicted cutoff, possibly due to the increased ionization implied by the lower ionization potential of nitrogen [53, 90]. In both cases we observed a distinctive peak around the K-edge, whereas the other peak at the lower end of the spectrum is an artifact due to the high absorption of the aluminum/magnesium filters below 200 eV. The independent occurrence of pronounced peaks around the K-edge, both in Ne and N_2, strongly suggests that we observe the result of some inner-shell dynamics in addition to the expected process of HHG, which will be analyzed in the next section.

Before we discuss different aspects of these spectra in more detail, let's have a look at the above mentioned error correction method for the case of multi-pixels events in the recorded data. Figure 2.15 shows the recorded spectrum

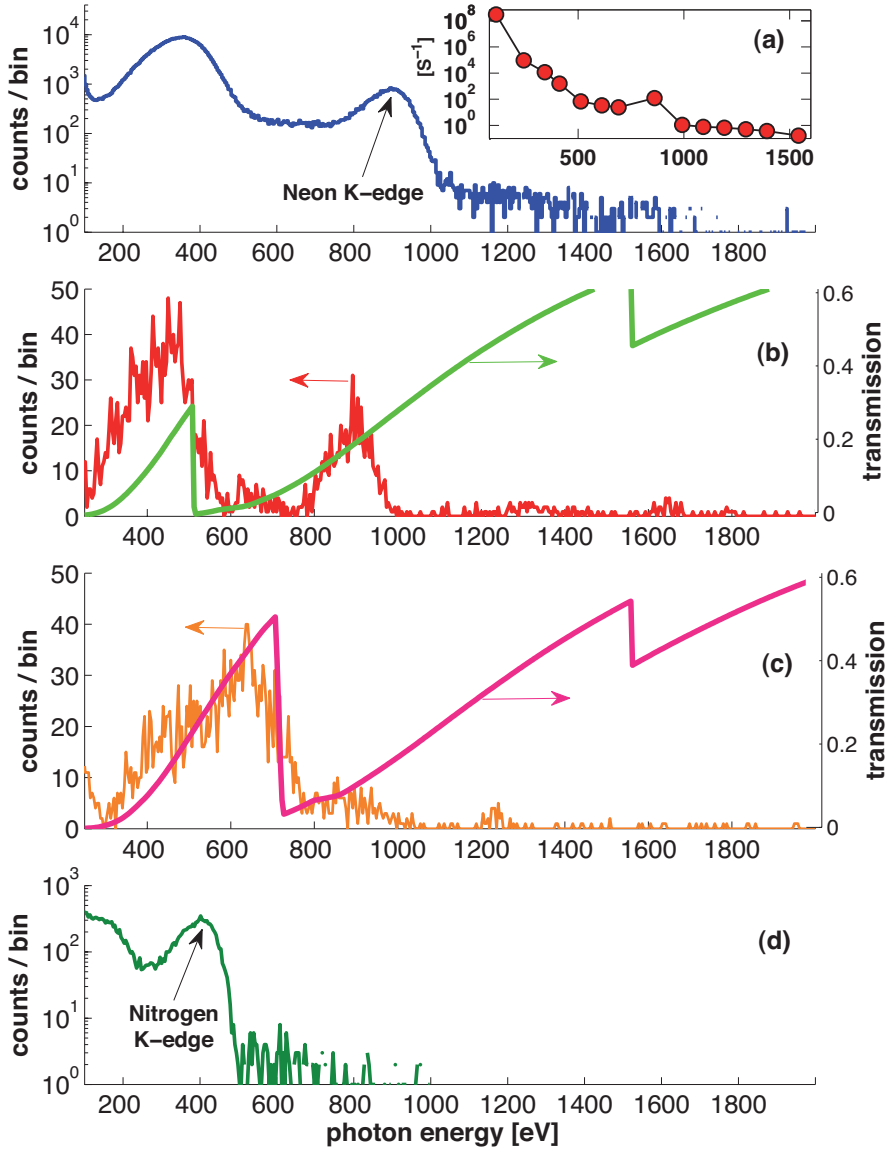

Figure 2.14: High harmonic spectra generated with Ne (a–c) and N_2 (d). (b) and (c) show the HHG spectra of Ne through additional 500 nm of vanadium and iron filters, respectively. Comparing the spectra in (b) and (c) to the spectrum in (a), a clear cut can be seen at the vanadium and iron L-edges. The transmission curves of the vanadium and iron filters are presented as well as green and pink lines. The inset figure in (a) shows the averaged absolute photon count rate in a 10 % bandwidth, after taking into account the transmission of the filters and the spectrometer efficiency

.

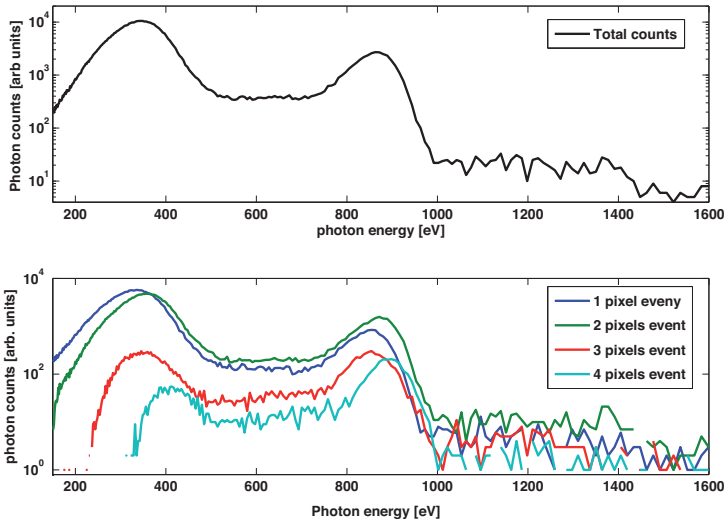

Figure 2.15: Spectral contributions from multi-pixels events. In the upper frame a recorded spectrum from the Ne target is presented, while the different contribuitions to the above spectrum coming from one-pixel events (blue), two-pixels events (green), three-pixels events (red) and four-pixels events (light blue) are shown in lower frame.

from a neon gas target (black) and the different contributions to this spectrum from single-pixel events (blue), two-pixels events (green), three-pixels events (red) and four-pixels events (light blue). It can be seen that at lower energies only single-pixel and two-pixels events are contributing to the spectrum. At higher photon energies more charge is generated and it tends to spread more, therefore generating also three-pixels and four-pixels events. Nevertheless, in the spectral range we are working at the one-pixel and two-pixels events are still dominating.

However, if two photons would hit the detector very close to each other this could in principle also create an event which looks similar to (C) or (D) in Figure 2.12 or even like a single event, if the photons hit exactly the same pixel. In that case this might cause an error in the construction of the spectrum. To demonstrate that this kind of miscounts does not unduly influence our spectra we made the following test: The probability that two photons hit the detector directly beside each other and therefore appear as a two-pixels event in our spectrum is equal to the probability to detect a single-pixel event and find

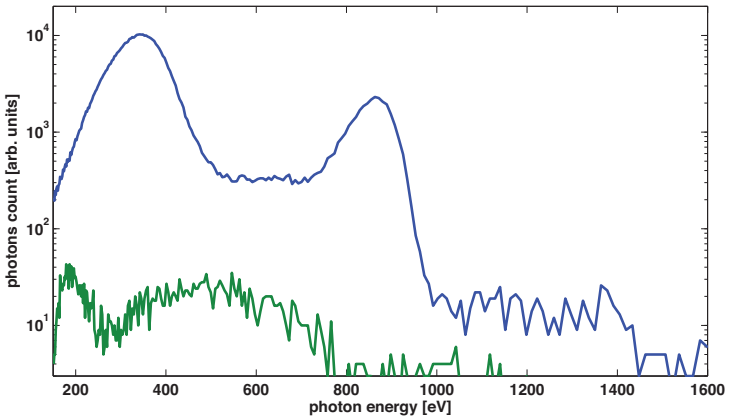

Figure 2.16: Comparison of spectra caused by real and 'pseudo' events. The blue curve represents spectra derived from all single-pixel and two-pixels events, while the green curve is constructed by adding up the detected pseudo single-pixel and two-pixels events.

another single-pixel event at one of four different fixed distances from this pixel. Therefore, if we detect a single pixel event, we check the positions three pixels to the left, three pixels to the right, three pixels above and three pixels below on the CCD. If we find another event there, we consider this as a pseudo two-pixels event and we count how many such pseudo two-pixels events we have for the whole chip. To take into account also the case that the second photon might hit exactly the same pixel as the first one, we check a fifth position in the neighbourhood of each single-pixel event to test for pseudo single-pixel events.

Figure 2.16 presents the results of this test. The blue line is the sum of the single-pixel and two-pixels events (see figure 2.15) and the green line is the sum of all the pseudo single-pixel and two-pixels events. Comparing these curves we conclude that the error caused by pseudo events in our spectrum is much smaller than the real signal and can be neglected, especially in the spectral region of the Ne K-edge and even at the range above 1 keV, where the signal is significantly lower.

To get a better picture of the parameter space for this new regime of HHG with a 2.1 μm driving laser, we measured XUV spectra at a broad range of different target gas pressures. In Figure 2.17 the soft-X-ray photon yield is plotted as a function of the gas pressure. With Ne, at the higher end of

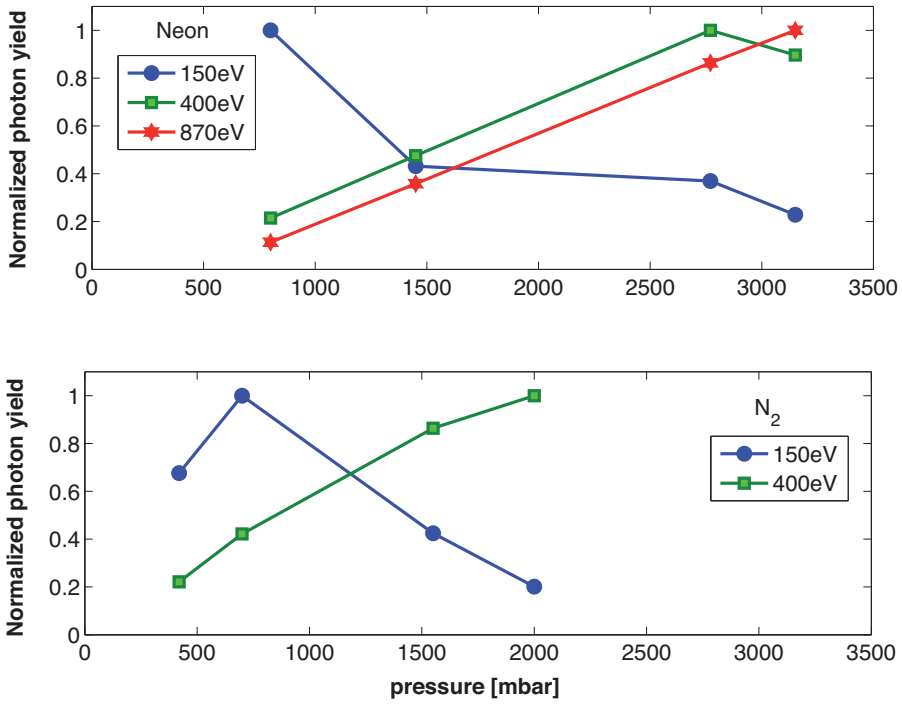

Figure 2.17: The photon yield as a function of the gas pressure at a few representative photon energies. The upper frame shows the results from the neon target while the lower frame shows the results from the N_2 gas target. The photon yields are normalized to the maximum photon yield at a given photon energy.

the spectrum ($\sim$500–1000 eV) we observed continuous growth of the photon yield up to a pressure of 3150 mbar, which was the upper limit for our vacuum pumping system. At the lower end of the spectrum ($\sim$150–250 eV) exactly the opposite behaviour was discernible: the photon yield drops continuously with the gas pressure, whereas for photon energies in a range in between ($\sim$ 360–450 eV) the harmonic yield grows up to a saturation pressure of about 2.8 bar, after which it starts to decrease again. A similar dependence was observed with N_2 at slightly lower pressures. The behaviour at the lower end of the spectrum matches our experience with high harmonics in the range of 50–150 eV, generated by an 800 nm driving pulse (compare for example [91]). For energies above 250 eV, the applied pressures we used in our measurements were much higher than the saturation pressure usually observed for low-energy harmonics driven by an 800 nm laser, but are in good agreement with other experimental data and theoretical work on HHG driven by IR fields with longer wavelengths [90, 92].

2.4 Bonus: Detection of direct inner-shell electron excitation

To understand the observed peaks around the K-edges in the measured spectra for Ne and N_2 we take a closer look on the theoretical conditions that can lead to a high yield of the XUV radiation. There are, in principle, several parameters that can influence the HHG efficiency. They can be classified as ones affecting the single-atom response and other ones determining the collective behaviour of the generating medium. In the former category, main factors include the atomic dipole moment and the ionization potential, neither of which is dependent on the presence of neighbouring atoms.

By contrast, collective emission heavily depends on the different contributions from all the atoms in the sample and hence on the pressure of the target gas. For example, if radiation from each target atom adds constructively, the harmonic yield grows quadratically with the number of emitters. Such a coherent build-up occurs in HHG provided the phase-matching condition is satisfied, i. e. the phase velocity of the harmonics matches that of the fundamental laser pulse. In mathematical form, it requires that $\Delta k_q = (k_q - qk_0) = 0$, where k_0

is the wave vector of the driving laser and k_q is the q^{th} harmonic wave vector.

To exclude the possibility that merely favorable phase-matching conditions, caused by the sharp change in the index of refraction at the K-absorption edge, give rise to the observed spectral enhancement we calculated the different contributions of the phase mismatch Δk_q. The latter is composed of the sum of the dispersion difference stemming from the neutral gas atoms, the dispersion difference induced by the plasma created by the laser and a purely geometrical factor, known as the Gouy phase shift [93, 94]. It can be written as $\Delta k_q = qk_0(\delta n_{atom} + \delta n_{plasma} - 1/k_0 z_R)$, where $\delta n_{atom/plasma} = n_q - n_0$ is the difference between the respective refraction indices at the q^{th} harmonic and the fundamental wavelength and $z_R = w_0^2 k_0/2$ is the Rayleigh range, with the IR beam waist w_0. Under our experimental conditions and for harmonics around 870 eV, we can estimate these contributions (neglecting for the moment possible resonance effects in the X-ray regime) as: $\Delta k_{atom} \approx -3.5 \times 10^3$ cm^{-1}, $\Delta k_{plasma} \approx 5 \times 10^5$ cm^{-1}, $\Delta k_{Gouy} \approx -7.3 \times 10^3$ cm^{-1}. Here we find that the plasma dispersion dominates over the other contributions by two orders of magnitude, thus allowing only for a low efficiency of HHG.

Next we investigate whether the influence of a nearby resonant transition can improve the phase-matching. Around a resonance line, the index of refraction may be written as $n^2 = 1 + A(\omega_0^2 - \omega^2 - i\omega\gamma_0)^{-1}$ and the radiation wave vector can be approximated as $k = \beta + i\alpha/2 \approx 1 + (A/2)(\omega_0^2 - \omega^2 - i\omega\gamma_0)^{-1}$, where A is proportional to the oscillator strength, ω_0 and γ_0 are the frequency and the natural width of the resonance transition, β is the real part of the wave-vector and α is the absorption coefficient. By substituting the values for α, ω_0 and γ_0 [95] we calculated that the maximum value for $(1 - n_{atom})$ in the XUV around the resonance is about 10^{-6}, which is still two orders of magnitude lower than the value of $(1 - n_{atom})$ in the near-IR regime. Therefore we conclude that the resonance transition around the K-edge can not account for a dramatic change in the phase-matching conditions.

The other possibility to explain the enhanced photon emission around the Ne K-edge is that once the recolliding electrons have enough energy to excite inner-shell electrons in their parent ions, the excited ions may subsequently decay via Auger electron emission or X-ray fluorescence. This process has long been predicted to happen for light–matter interactions with sufficiently intense

electric fields (compare also Fig. 1.1, panel 3 c and section 1.2.2), but has never been directly measured due to the high binding energies involved. Nevertheless, this incoherent X-ray photon emission would explain the enhanced feature we observe around the K-edge regions.

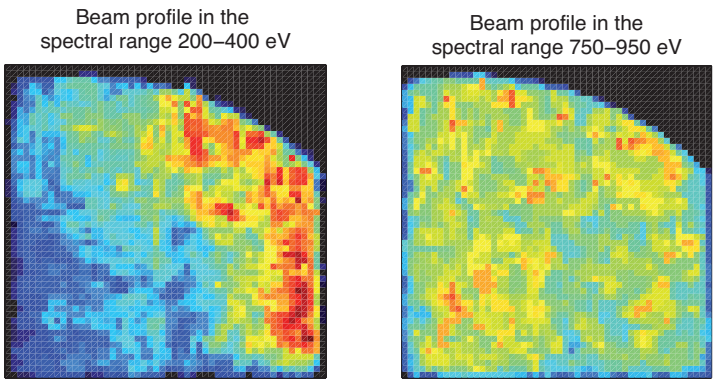

Figure 2.18: Energy-resolved XUV radiation profiles for two different spectral ranges. The uniform radiation distribution at photon energies of 750–950 eV is an indication that it comes from a fluorescence process and not from harmonic generation. The detector size is $\sim 1 \times 1$ cm^2 and it was placed 60 cm away from the gas target. The rounded upper right corner is due to the aluminum filter.

Support for this hypothesis is gained by analyzing the XUV beam profile as a function of the photon energy. It is well known that the harmonics beam, due to their spatial coherence, has a very low divergence and well defined beam shape. The fluorescent radiation on the other hand is going into all directions and is expected to cover the detector uniformly. The ability of our custom-built detector to resolve both the position and the energy of the XUV photons at the same time, allows us to observe the shape of the emitted radiation as a function of the photon energy. Fig. 2.18 shows the energy-resolved XUV radiation profiles at two different spectral ranges. The first profile is taken at the spectral range between 200–400 eV, where the XUV radiation is expected to come from the harmonic process, while the second profile is set in the spectral range between 750–950 eV, around the K-edge of Ne, where we assume that the radiation is coming mainly from fluorescence. Although not perfectly adjusted through the aluminum filter and on the CCD

chip, due to the inherent difficulties with alignment of a 2.1-μm-wavelength driver laser mentioned above, we clearly see that the radiation between 200–400 eV is spatially confined as we can expect from high harmonic radiation. On the other hand, the radiation distribution in the spectral range between 750–950 eV is uniform, supporting the assumption that it stems from a fluorescence process.

To further verify whether this assumption is correct, we scrutinized the pressure dependence of the photon yield particularly around the K-edge. The probability per unit time for an electron detached at $t = t_i$ to excite an inner-shell electron of its parent ion is given by

$$dp_{ex}(t_i) = \left(\sigma_{ie}/\pi W^2\right)\eta(t_i)\,dt, \tag{2.10}$$

where σ_{ie} is the cross section for excitation of the inner-shell electron through inelastic collision [96], W is the radius of the electron wave packet at the recollision time and η is the ionization rate calculated with the Ammosov-Delone-Krainov (ADK) tunnel ionization theory [97]. The density of the inner-shell excited ions is accordingly:

$$\rho_{ex} = \int \rho_0\, dp_{ex} = \rho_0 \frac{\sigma_{ie}}{\pi W^2} R, \tag{2.11}$$

with the gas density ρ_0 and $R = \int \eta(t)\,dt$ is the total degree of ionization. Including also the self-absorption in the gas, we can write the differential equation for the emitted photons as $dN/dz = \rho_{ex}S - (R\rho_0\sigma_a)N$, where N is the number of photons, z is the spatial coordinate in the direction of the laser propagation, S is the effective beam area in which the local intensity is high enough to generate electrons with energies above the K-edge and σ_a is the absorption cross-section. By solving this equation we finally get the averaged photon count rate on the CCD:

$$\Phi_{av} = \frac{\rho_{ex}}{R\rho_0}\frac{S}{\sigma_a}\left[1 - \exp\Big(-(R\rho_0\sigma_a)L_{med}\Big)\right]\frac{\Gamma_{rad}}{\Gamma_{Au}} f_R \frac{d\Omega}{4\pi}. \tag{2.12}$$

Here L_{med} is the length of the interaction medium, Γ_{Au} and Γ_{rad} are the Auger and the X-ray radiation decay rate of the excited state, respectively, f_R is the laser repetition rate and $d\Omega$ is the solid angle subtended by the CCD. Since $\rho_{ex} \propto \rho_0$, equation (2.12) predicts a linear growth of the photon yield

with the pressure, followed by a saturation when $(\rho_0\sigma_a)L_{med} \gg 1$ (compare the inset of Fig. 2.19). By substituting the absorption cross-section and the gas density relevant to our experiment (see Table 2.1 for numerical values of all mentioned parameters under our experimental conditions), we find that the predicted photon yield should already be saturated, though our experimental data still show a linear growth, as can be seen from Fig. 2.19.

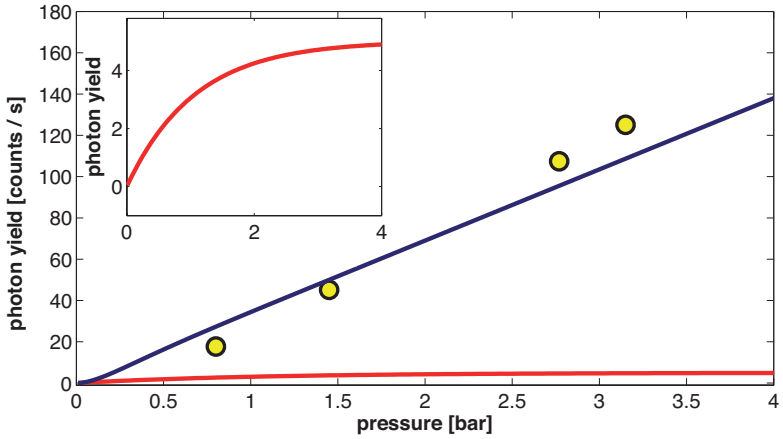

Figure 2.19: Comparison of electron recollision models. The photon yield around the Ne K-edge as a function of the backing pressure of the target gas. The red lines in the main figure and in the inset show the predicted incoherent photon yield according to the model of recollision with the parent ion, the blue line represents the prediction of the expanded calculation, taking into account the collisions with neighbouring atoms. The yellow circles mark the measured photon yield at a 10 % bandwidth around 870 eV (resulting from both coherent and incoherent radiation).

In an attempt to elucidate this behaviour further, we have to expand our model to include electron collisions with neighbouring atoms, on account of the fact that due to the long driver wavelength the liberated electron's excursion amounts to a few tens of nanometers, making the probability of collision with neighbouring atoms at high pressures significant. This can be taken into account by replacing (2.10) with

$$dp_{ex}(t_i) = \Big(\eta(t_i)\,dt\Big) \int_{t_i}^{\infty} \rho_0 \sigma_{ie}(v) v(t')\,dt' \tag{2.13}$$

and accordingly rewriting the differential equation for the photon emission

$dN/dz = \rho_{ex}S - [(1-R)\rho_0\sigma_a]\,N$, where $v(t)$ is the velocity of the electron in the laser field and $\rho_{ex} = \int \rho_0 dp_{ex}$ is obtained by substituting the new excitation probability dp_{ex}. Using the experimental parameters given in Table 2.1, we obtain a theoretical prediction in excellent agreement with the experimental data (see Fig. 2.19). σ_{ie} is the only parameter we used to fit our model to the experimental data, which was chosen due to the large uncertainty in the literature about its value. Regardless, a change in any of the less well-defined parameters (σ_{ie}, $\eta(t)$, Γ_{rad} and S) would cause merely an overall rescaling, thus not compromising our general argument. We further note, that we have neglected the contribution of the coherent radiation in all of the above calculations. This is justified, considering the observed decrease of the coherent photon yield by an order of magnitude in the range between 500–700 eV (see Fig. 2.14(a)) and because of our previous calculation that we cannot expect better phase-matching conditions in this energy range.

These findings strongly suggest, that inner-shell ionization by recolliding electrons and subsequent X-ray fluorescence is indeed a very likely explanation for the observed spectral peak near the K-edge in our experiment. In addition, our theoretical results (comparison of the blue and red curves in Figure 2.19) reveal that for pressures of the order of 1 bar and higher, collisions with neighbouring atoms become the dominant inner-shell excitation mechanism.

2.5 Conclusion

In conclusion, I have shown the extension of laser-induced recollision phenomena, a process vital for attosecond science, high-order harmonic generation and inner-shell excitation, into the kiloelectronvolt regime by using a few-cycle mid-infrared driving field. The enhanced peak and the isotropicity of the XUV radiation at the spectral range around the K-edge are evidences for inner-shell excitation by the laser induced electron re-collision. Owing to the highly nonlinear scaling of the tunneling probability with laser intensity and the pulse duration comparable to the wave period, the excitation can be substantially confined to a single, isolated recollision event and hence to a tiny fraction of the laser oscillation period. The resultant sub-femtosecond trigger window

Symbol	Value	Comments
W	0.63 nm	
ρ_0	$P \times \left(3 \times 10^{19}\right)$ cm^{-3}	P is the pressure in bar
L_{med}	0.2 cm	
S	4.3×10^{-6} cm^2	
f_R	1000 s^{-1}	
Γ_{Au}	4×10^{14} s^{-1}	
Γ_{rad}	$\approx 2.2 \times 10^{12}$ s^{-1}	ref. [98]
$d\Omega$	1/3600	
$\eta(t)$		calculated with the ADK theory [97]
σ_{ie}	$\approx 0.25 \times 10^{-19}$ cm^2	ref. [96]
σ_a	$\approx 2.2 \times 10^{-19}$ cm^2	ref. [99]

Table 2.1: Parameters for the theoretical model of electron recollision

and the orders of magnitude enhanced excitation probability (as compared to the use of current generation high harmonic sources) opens the prospect for studying atomic and molecular inner-shell excitation and relaxation processes directly in the time domain.

Chapter 3

Scaling the intensity of XUV pulses for high-flux experiments

It has been a longstanding goal of ultrafast physics to utilize the recently developed table-top sub-femtosecond XUV and soft X-ray sources (compare chapter 2; an overview can be found e. g. in [45] and [100]) for the time-resolved measurement of a vast scope of phenomena happening on an atomic time scale. A number of experiments have been conducted with these sources over the last decade, reporting on attosecond (1 as = 10^{-18} s) measurements of the coupled electronic and nuclear processes in photochemical reactions [101], photoemission in atoms [12, 16, 17], molecular photoionization and dissociation [14] and electron dynamics in solids [44].

Despite these breakthrough achievements, all of the experiments with HHG sources so far are severely limited by the relatively low conversion efficiency from long-wavelength infrared to the XUV wavelength, resulting in a total XUV flux of the order of 10^6 photons per isolated attosecond pulse that can be utilized for experiments [102]. Therefore, up to now these measurements have been restricted mainly to single-XUV-photon ionization processes and time-resolved pump/probe schemes relying on cross correlation techniques between the XUV pulse and the high harmonic-driving IR field.

On the contrary, many of the most intriguing research areas potentially accessible with the help of these XUV sources require high optical intensities, as has been demonstrated by pioneering studies in the field of nanoscale imaging, like time-resolved soft X-ray microscopy [103], coherent diffraction imaging

[104] or single-shot nanocrystallography [105], or for the envisioned real-time observation of ultrafast atomic reaction dynamics via XUV-pump/XUV-probe spectroscopy.

Different attempts to develop XUV sources with higher photon flux have been made over the past years, but have been confined to comparably low ($\lesssim$ 50 eV) XUV photon energies [106–108]. In this chapter I will present our results concerning the buildup of a $\sim$ 100 eV photon source, driven by a high-power, few-cycle NIR laser system and delivering XUV radiation with orders of magnitude higher power than obtained in previous HHG set-ups at these photon energies (e. g. [109]). Note, that the term 'flux' in the following discussion is defined as the number of photons per pulse, to facilitate meaningful comparisons between sources with different repetition rates.

3.1 LWS 20: A high-energy, few-cycle OPCPA system

The laser system delivering the necessary high-power, few-cycle NIR pulses for the efficient generation of XUV radiation with ultrahigh flux was developed at the Max-Planck-Institute of Quantum Optics and dubbed LWS 20, for Light Wave Synthesizer (with a power of) $\sim$ 20 TW. To reach the aimed for terawatt level of output power, the LWS 20 is making use of the principle of OPCPA, as described for the IR laser in section 2.1, and hence takes advantage of the broadband, high-gain amplification that such a set-up can provide. Nevertheless, the target specifications are obviously fundamentally different from the ones for the IR system, necessitating a completely different layout of the OPCPA. The whole laser system was developed in a series of a few distinctive steps, each comprising a novel demonstration of an ultrashort, high-power NIR source in its own right [70, 110–112]. Here I will give a very brief summary of the system in its current status and the delivered output characteristics during our measurements [71]. A thorough analysis of the design principles for a high-power noncollinear OPCPA can be found in [78].

The front end for the OPCPA (see Fig. 3.1) is a broadband Ti:sapphire oscillator delivering pulses with an energy of 4 nJ and a duration of 5.5 fs. For all-optical synchronization between the seed and the pump pulses in the

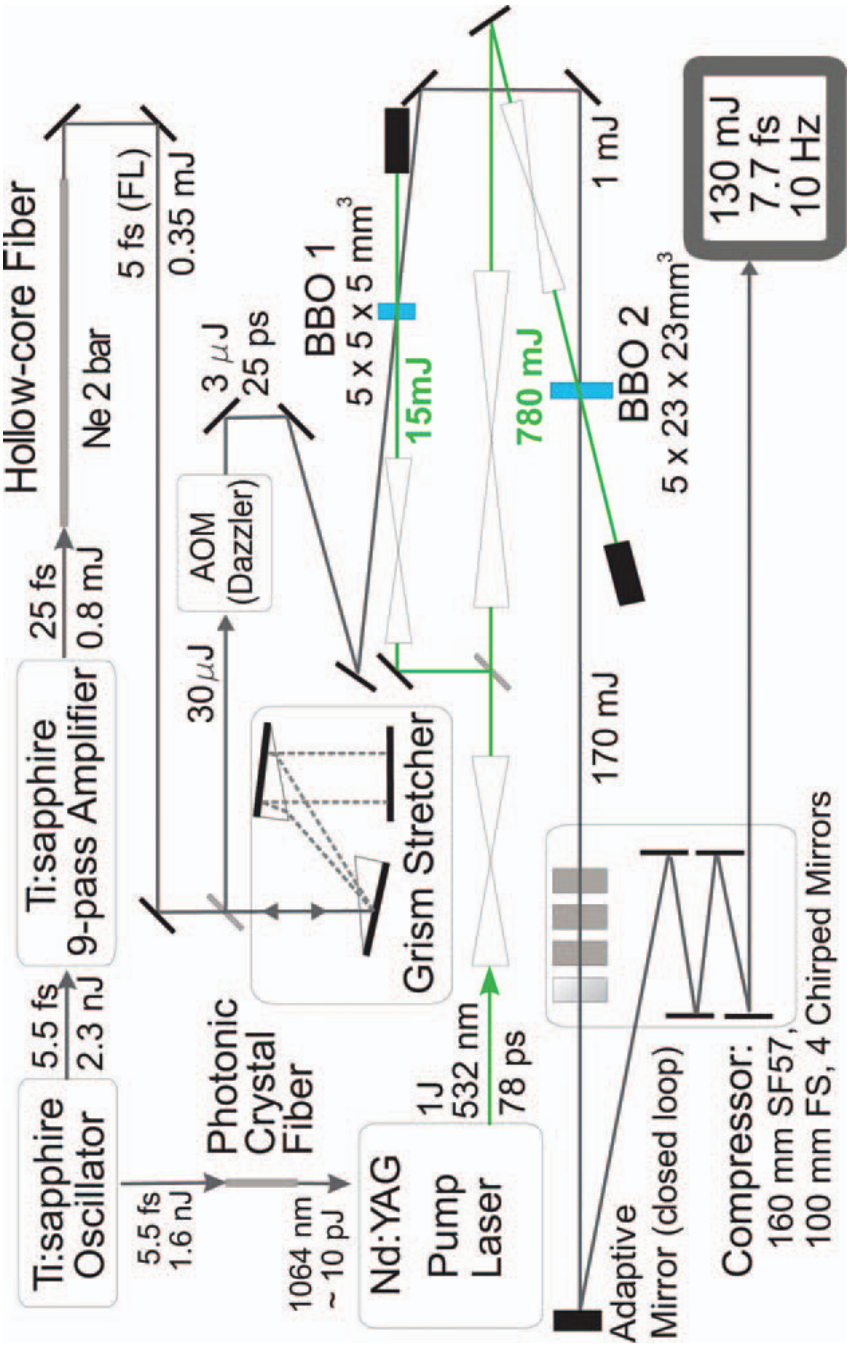

Figure 3.1: **Set-up of the high-power OPCPA LWS 20.** A detailed description of the system is given in the text. (Figure reproduced from reference [71].)

OPCPA stages the output from the oscillator is split at the rate of 60 to 40 %, respectively. The seed arm is further amplified in a multipass CPA system and subsequently focused into a hollow-core fiber (HCF) filled with neon gas at a pressure of $\sim$ 2 bar, where the seed is spectrally broadened via self-phase modulation [113, 114]. After the HCF the spectrum ranges from 500 to nearly 1000 nm, which corresponds to a transform limited pulse duration of 5.5 fs at 805 nm central wavelength. The pulses are then temporally stretched by introducing negative dispersion with the help of a pair of 'grisms', a combination of a prism and a grating [115, 116], in reflection geometry and an acousto-optical modulator (DAZZLER, Fastlite). In a grism (from grating + prism = 'grism') the prism selects a central wavelength that passes straight through on the optical axis of the arrangement, while the grating, with its much higher dispersive properties than glass, introduces the required negative dispersion. After the stretching the seed pulses for the noncollinear OPCPA have a duration of 25 ps and a pulse energy of 3 µJ and are synchronized to the pump pulses at a repetition rate of 10 Hz.

This pump pulse is built on the remaining 40 % of the oscillator output, which is converted to a central wavelength of 1064 nm by soliton-based self-frequency shifting in a photonic crystal fiber [82, 117] and then coupled into a Nd:YAG regenerative amplifier. Subsequently, these pulse are guided through two parallel flash-light pumped Nd:YAG amplifier chains (EKSPLA) that are brought together again in a Dueterated Potassium Dihydrogen Phosphate (DKDP) crystal to generate a single pump beam at 532 nm central wavelength via noncollinear type II second-harmonic generation (SHG) with a final energy of 1 J and a pulse duration of 78 ps.

The seed and the pump pulse are noncollinearly overlapped in two successive OPCPA stages, consisting of two type I Beta Barium Borate (BBO) crystals, which are pumped by 15 mJ pulses with a peak intensity of 13 GW/cm^2 (first stage, BBO front surface 5×5 mm^2) and by 780 mJ pulses with a peak intensity of 8.2 GW/cm^2 (second stage, BBO front surface 23 × 23 mm^2), respectively. The amplified signal pulse energy after the second OPCPA stage amounts to $\sim$ 170 mJ with energy fluctuations below 3 % rms. Since the seed pulse energy is comparatively high (some microjoules), the parasitic process of optical parametric fluorescence in the OPCPA crystals can successfully be suppressed

to a minimum and the second stage can be operated in saturation, leading to a good pulse energy stability and a high pulse contrast, both necessary prerequisites for efficient HHG.

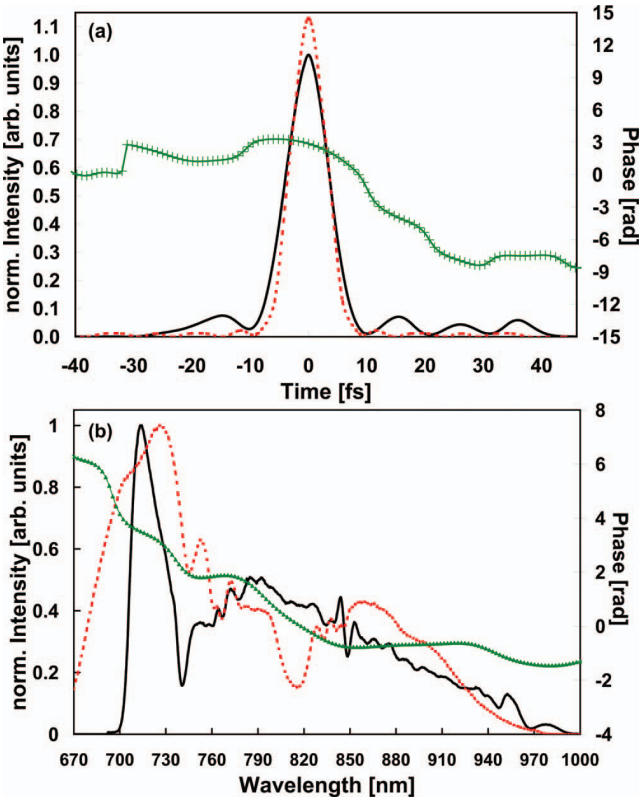

Figure 3.2: FROG measurement of the pulse duration (a) and spectrum (b) of the amplified output from LWS 20. Panel (a) shows the retrieved temporal pulse intensity envelope (black solid curve), the residual phase (green crosses) and the Fourier-limited pulse duration (red dashed curve). In Panel (b) the corresponding measured spectrum (black solid) is depicted, together with the retrieved spectral phase (green triangles) and the spectrum of the stretched seed pulse before amplification (red dashed) for comparison. (Figure reproduced from reference [71].)

The pulses are temporally pre-compressed with bulk material (160 mm of SF57-Schott glass and 100 mm of fused silica) and undergo wavefront correction on an adaptive mirror working in a closed-loop configuration utilizing a Shack-Hartmann sensor [118, 119]. Finally, the beam is coupled into a vacuum chamber and compressed by reflection on positive dispersive mirrors. This is done to avoid self-focusing of the short pulse due to an increase of the B in-

tegral along the beam path above 1 [120], where $B = \frac{2\pi}{\lambda_L} \int n_2 I_L(z)\, dz$, I_L and λ_L are the laser intensity and wavelength, respectively, and n_2 is the nonlinear refractive index in the traversed medium, defined by the change of the index of refraction n in proportion to the optical intensity, $\Delta n = n_2 I_L$. The achieved pulse duration is measured with the help of a home-built single-shot SHG frequency-resolved optical gating (FROG) device to be 7.9 fs FWHM and is shown along with the residual phase in Fig. 3.2. Taking into account the energy losses in the compression part of the laser set-up, under optimal conditions the LWS 20 system provides an output of 130 mJ pulses with 7.9 fs duration, and therefore am peak power of 16 TW, at a central wavelength of 805 nm and a repetition rate of 10 Hz. Due to the high complexity of the whole laser system and the very sensitive dependence of the actual compressed pulse duration on the spectral phase of the seed after the HCF, these parameters can only be reached by a meticulous and rather time-consuming alignment procedure, so that for our experiments on a day by day basis we used the compromise of a slightly less powerful but easier manageable OPCPA output performance.

3.2 Experimental set-up — the beamline AS 6

To utilize the described OPCPA system (section 3.1) for high harmonic generation, the usual set-up of the interaction region between the intense light field and the gas atoms has to be adapted to the application of a high-power driving laser. Essentially the whole experimental design for the conventionally employed sources providing pulse energies in the sub-mJ regime has to be scaled according to the needs of a $\sim$100 mJ, few-cycle near-infrared (NIR) laser pulse. The specific working conditions for efficient HHG are determined by the choice of the type and the density of the target gas on the one hand and, on the other hand, by the wavelength and the peak intensity I_L of the laser field on target, which is given by

$$I_L = \frac{W_L}{\tau_L w^2 \pi}, \tag{3.1}$$

where W_L is the pulse energy, τ_L is the pulse duration, measured as the full width at half maximum (FWHM) of the intensity envelope, and w is the beam radius, defined as the distance from the beam axis at which the intensity drops

to $1/e^2 \approx 13.5$ % of the value on axis. For the generation of XUV radiation around 100 eV with an 800 nm, few-cycle pulse the optimal laser intensity $I_L \sim 5 \times 10^{14}$ W/cm^2. Keeping the gas density, the driving laser wavelength and the pulse duration approximately unchanged, the requirement to work in the same intensity regime means that a factor hundred more in pulse energy W_L corresponds to a ten times bigger beam radius w — and therefore a factor 100 more with regard to the interaction area w^2 — in the focus. It follows, that for efficient HHG with the LWS 20 the beam radius on target must be ten times bigger than for the usual sub-mJ driver lasers (compare for example [102]), yielding a beam radius of ~ 500 µm in a realistic set-up.

To achieve those large spot sizes and big enough beam diameters on the optics in an experiment, the focusing geometry has to be chosen in a manner which requires optics with focal lengths in the order 7 to 15 meters. In addition, the increasing intensity of the focused beam due to the convergence along the axis surpasses the damage threshold of most optical components already ~ 5 m in front of the focus, preventing a space saving set-up by folding the beam with a suitable arrangement of high-reflective mirrors.

A special vacuum beamline was set up at the MPQ, situated on a robust steel bridge above the LWS 20 OPCPA system, and accommodating four vacuum chambers connected by metal tubes, to comply with these extraordinary demands. More vivid material concerning the construction of this beamline can be found in the appendix. The first part of the beamline is schematically depicted in Figure 3.3. In the first chamber the high-power beam is focused by an assembly of a plane backreflecting and a spherical focusing mirror under a small angle to avoid astigmatism. From there, the beam travels convergently to the folding chamber, the last accessible point along the beam path, where reflective optics can be introduced into the laser beam without destroying them. Alternatively, for smaller focal sizes in the third chamber and hence even higher intensities, the first chamber can just be passed through and the laser can be focused in the second chamber by optics with shorter focal lengths (still ~ 8 m!). In the third chamber the laser is interacting with rare gas atoms streaming from a nozzle and HHG takes place. For the details of the involved process compare section 1.2. Since the interaction area is hundredfold larger than in the case of the usual Ti:Sapphire-amplified laser sources, the number of

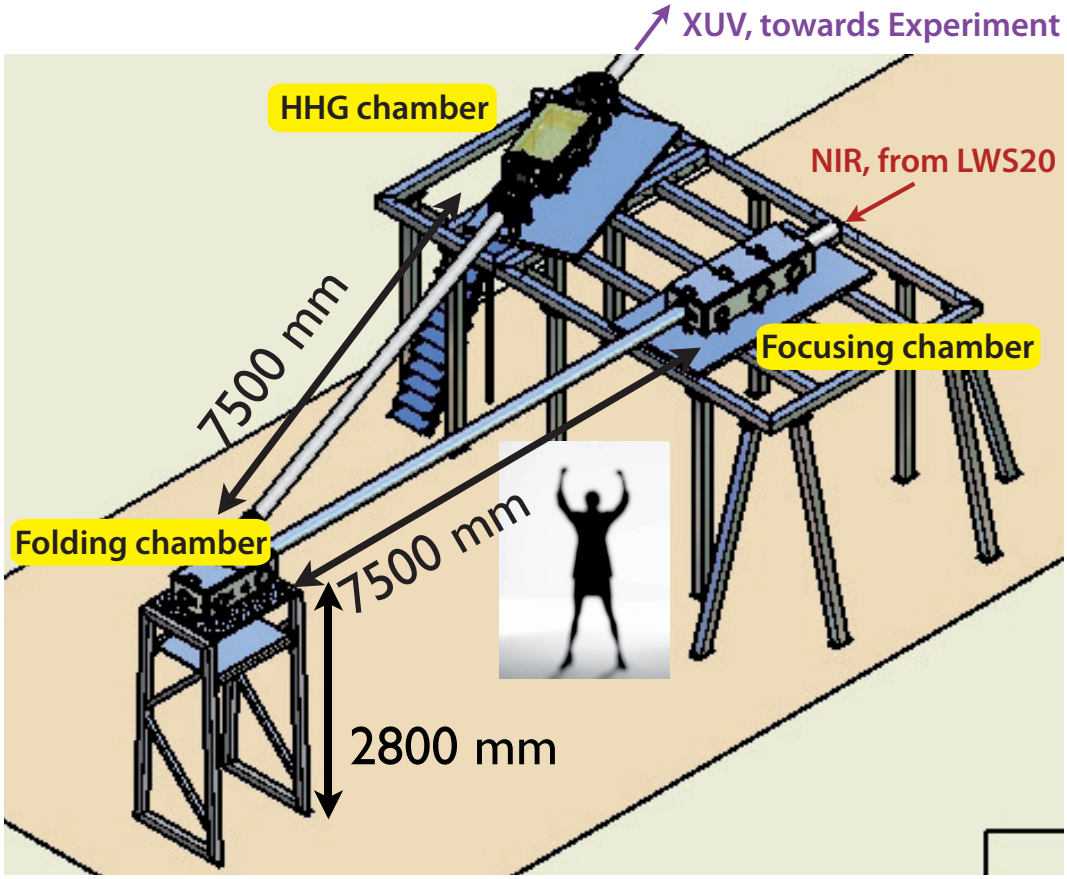

Figure 3.3: First part of the AS 6 Beamline at the MPQ. The scaffold for the vacuum beamline was built above the existing laser system LWS 20 to gain the necessary space for the implementation of the loose focusing geometry. Some distances are also denoted in the sketch.

generated XUV photons per pulse is expected to scale accordingly. This would enable the generation of coherent, ultrashort XUV pulses with intensities high enough for pump/probe or other nonlinear experiments. In section 3.3, I will report on the accomplished HH spectra and the measured intensities of the XUV radiation.

After HHG in the third chamber shown in the sketch in Fig. 3.3, the NIR and the XUV beam are propagating collinearly towards the experimental chamber. For the first proof-of-principle test of this high-intensity XUV beamline this part was composed of a simple XUV detection and characterization set-up, illustrated in Figure 3.4. It incorporates interchangeable metal filters, a home-built XUV spectrometer and a special XUV photodiode (not shown in the

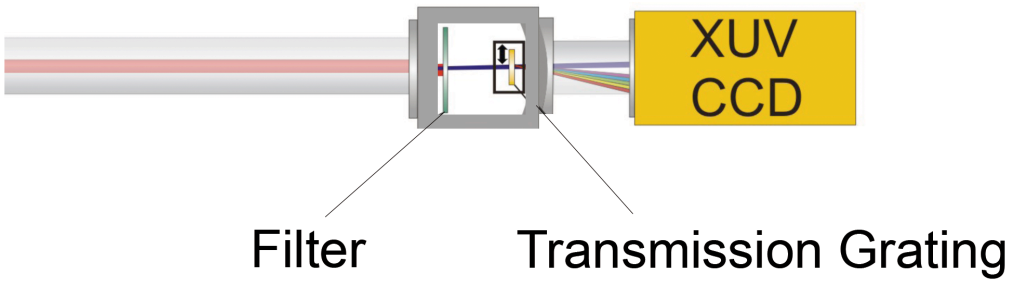

Figure 3.4: XUV detection and characterization assembly at the AS 6 Beamline. The drawing illustrates the XUV detection area with the metal filter wheel, the removable transmission grating and the XUV CCD, that can also be used as a spectrometer in combination with the grating. The photodiode for measuring the total XUV flux is not shown.

figure). The metal filter, usually zircon (Zr), is used for spectral filtering by completely blocking the fundamental laser, while still transmitting a substantial percentage of the XUV radiation, and is also important for the energy calibration of the spectrometer. The XUV spectrometer consists of a transmission grating with 5000 lines/mm and a XUV CCD (PIXIS-XO, Princeton Instruments) for the detection of the dispersed harmonics. Finally, the XUV photodiode (AXUV-100, IRD, Inc.) is used for the measurement of the XUV intensity. It is a special diode with directly deposited filters: 200 nm Zr as a filter for the fundamental laser combined with a carbon layer as protection against oxidation. These photodiodes are especially sensitive for the spectral range between 6–16 nm, corresponding to XUV photon energies of ∼80–200 eV.

3.3 High-flux harmonics at 100 eV

For the most efficient generation of high-intensity XUV radiation we used the output of the OPCPA system LWS 20, after transport through the beamline and reflection on a number of mirrors amounting to a pulse energy on target of ∼40 mJ with a pulse duration of ∼12 fs, and focused the beam into a gas cell with variable length between 1 and 10 cm. The beam radius in the focus after optimization of the adaptive mirror was ∼400 μm, leading to an intensity on target of roughly 7×10^{14} W/cm^2 (see Fig. 3.5).

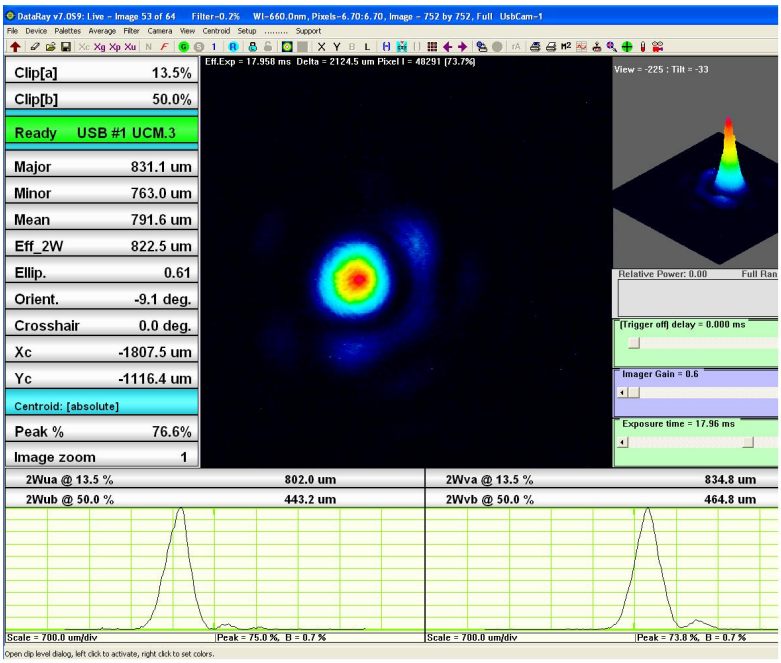

Figure 3.5: LWS 20 beam at the focus in the HHG chamber measured with a commercial beam profiling system (WinCam, DataRay Inc.). The beam profile was optimized depending on the high harmonic intensity with the adaptive mirror in the OPCPA system. The $1/e^2$-beam diameter in the focus is measured to be ~ 800 µm.

The cell has a 1-mm hole on the frontside and on the backside, so that the laser and the generated harmonic beam can pass through unhindered without completely opening the interaction volume to the rest of the chamber. This way, the gas load on the surrounding vacuum system was minimized, avoiding excessive absorption of the generated XUV radiation due to an increased background pressure. For the best high harmonic yield, the constant backing pressure on the gas inlet of the cell was set to 45 mbar, corresponding to an actual pressure in the laser focal area inside the cell that was estimated to ~ 11 mbar. This pressure difference is due to the nonnegligible loss of gas through the entrance and exit holes in the cell.

We also tried a supersonic gas nozzle as a target. A Laval design was chosen to achieve a small spread of the emitted gas packet with a diameter of $\sim$ 1.5 mm, and hence provides a high gradient of the gas density [121]. The nozzle was pulsed at the laser repetition rate of 10 Hz to restrict the generated gas

flow to the vacuum chamber. But even when increasing the backing pressure to 3 bar and more, essentially reaching the limit of the tolerable gas load for our vacuum pumping system, we could not achieve the same HH output as from the longer gas cell. It is important to note, that because of the Laval geometry the actual gas pressure at the nozzle exit is severely reduced from the value of the backing pressure and was determined experimentally (by way of XUV absorption measurements) and theoretically (by comparison to simulations, see [121]) to lie between 100 and 200 mbar. In Figure 3.6 you can see the bright plasma in the focus for the supersonic nozzle with high backing pressure.

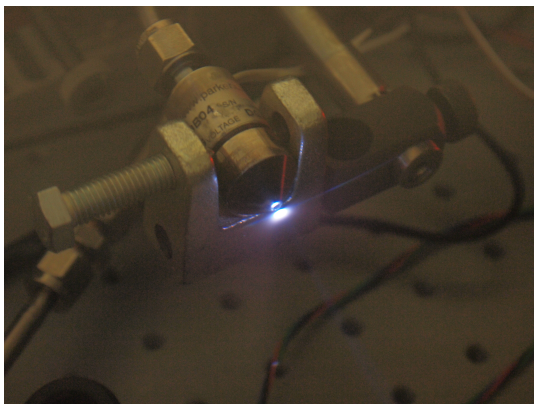

Figure 3.6: Plasma in the HHG focus at the beamline AS 6. Rare gas is streaming with a pressure of $\sim$ 150 mbar from the pulsed nozzle and ionized by the high-power laser. The large focal size in the employed focusing geometry is evident with the naked eye. The bluish colour of the plasma points towards argon as the interaction medium in this photograph.

The observed behaviour complies with the expectation from previous measurements [92, 106, 107, 122] and theoretical calculations [123], that for the loose focusing employed in our set-up good phase-matching conditions can be sustained over a distance defined by the Rayleigh range, $z_R \equiv \frac{w^2\pi}{\lambda_L}$ for a Gaussian beam. In the employed experimental geometry the Rayleigh range is substantially extended and amounts to some tens of centimeters. Hence harmonic radiation emitted all along the laser beam path through the gas cell is interfering constructively and contributions from the whole volume add up to the total XUV yield, resulting in a significantly enhanced conversion rate from the fundamental to the higher harmonic wavelength. Accordingly, the XUV flux was not very sensitive to changes of the gas cell length in the range of a

few centimeters. For the backing pressure of 45 mbar used in the experiment the highest XUV flux was achieved with an interaction length set to $\sim$4 cm.

A CCD image of the direct harmonic beam is shown in Figure 3.7. Inserting the transmission grating into the beam, the XUV radiation gets energetically dispersed and the spectrum can be spatially resolved on the CCD chip, which is demonstrated separately for the lower (Fig. 3.8a) and the higher (Fig. 3.8b) energy range.

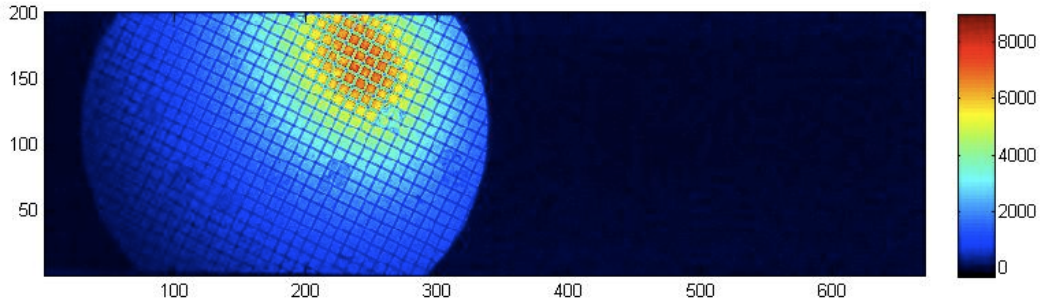

Figure 3.7: CCD image of harmonic beam from LWS 20. The visible grid structure is produced by the mesh supporting the 1000 nm-thick Zr filter, that blocks the fundamental laser.

In the lower energy spectrum, generated in argon, (Fig. 3.8a) the different harmonics are easily discernible, as well as the the Al edge from the filter that was used for the calibration of the spectrum. For the higher energies, presented in Fig. 3.8b, we used neon as a the interaction medium. The individual harmonics lie much closer together for these shorter wavelengths and cannot be distinguished anymore due to the limited resolution of our home-built spectrometer.

Nevertheless, the usual plateau (in the middle) and the cutoff region (to the right) typical for HHG are manifest in the spectrum, which extends well above 120 eV. Thus it has been proven that high harmonic generation under the condition of very gentle focusing is working as expected and the spectral structure is similar to that achieved with a much tighter focus with less intense laser sources.

However, the XUV flux should be much higher in the case of the high-power OPCPA system. Indeed, this was clearly confirmed by the investigation

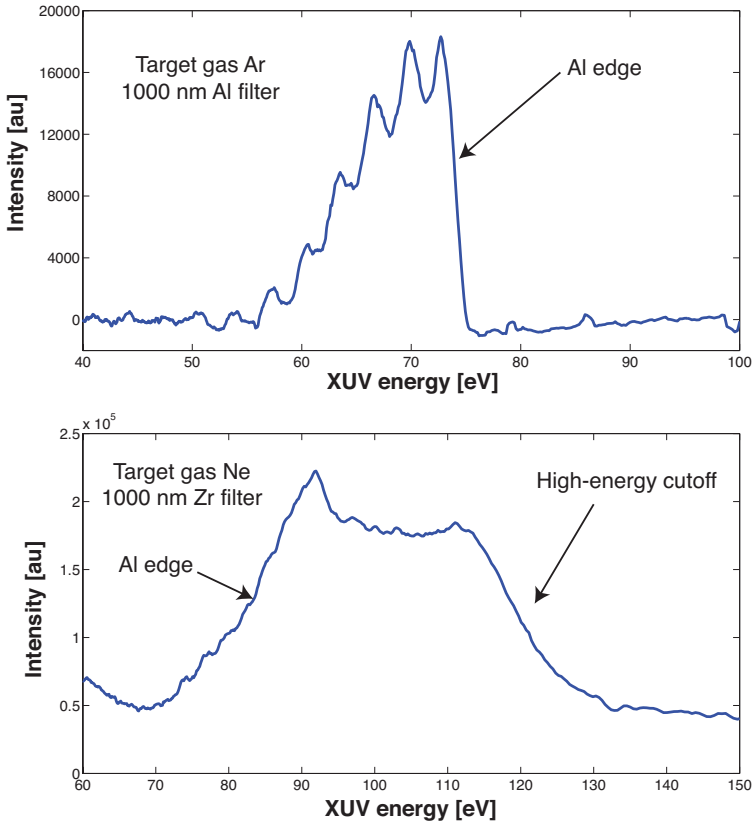

Figure 3.8: Harmonic spectra generated by the high-power OPCPA LWS 20. In the upper panel the high harmonic spectrum generated in Ar is presented, which ranges from around 55 eV up to the Al filter absorption edge at ∼73 eV. The lower panel shows the spectrum obtained from neon gas, starting at ∼ 70 eV, where the Zr filter becomes transmissive, with a plateau spanning from 90–110 eV and a high-energy cutoff extending to more than 130 eV.

of the harmonic intensity with the AXUV-100 photodiode described above. Figure 3.9 shows the trace of a measurement for a single XUV pulse with this device, recorded by a digital oscilloscope (DPO/DSA/MSO70000, Tektronix). To evaluate this voltage signal one has to integrate over the area below the curve and divide by the amplifier gain to get the total charge Q_{tot} that corresponds to the measured XUV intensity.

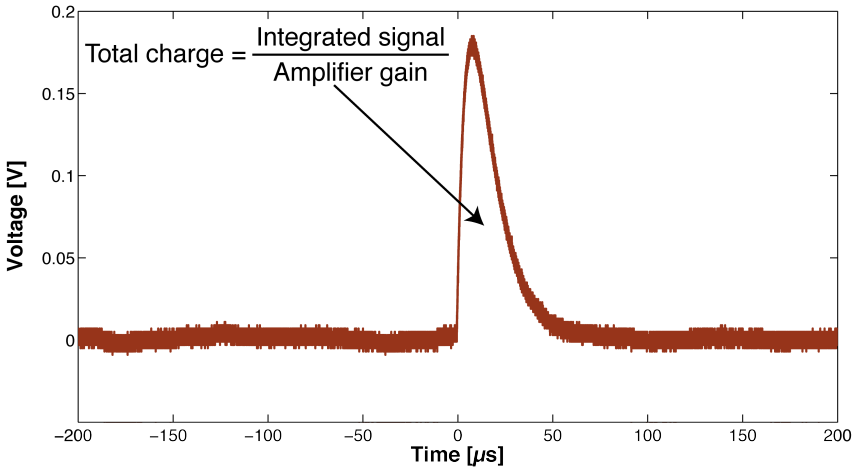

Figure 3.9: Determination of the XUV intensity. The Figure shows the trace of the amplified high harmonic signal, detected by the XUV photodiode and measured with the help of a digital oscilloscope.

The integrated signal amounts to $S_{int} \approx 3.75$ Vμs $= 3.75 \times 10^{-6}$ Vs and the amplifier gain was set to $g_{amp} = 10^3$ V/A, so that

$$Q_{tot} = S_{int}/g_{amp} = 3.75 \times 10^{-9} \text{ C} \tag{3.2}$$

or, expressed by the elementary charge $e \approx 1.6022 \times 10^{-19}$ C,

$$Q_e = 2.3435 \times 10^{10}\ e. \tag{3.3}$$

Taking into account the detection quantum efficiency of the photodiode (the number of electrons produced per incident photon $R_{eff} \approx E_{ph}/3.7$, with $E_{ph} =$ 100 eV being the relevant central XUV photon energy) and the transmission through the Zr filter with a thickness of 700 nm, $T_{filter} \approx 0.07$ in the spectral range 70–120 eV, the number of photons per XUV pulse is given by

$$N_{ph} = \frac{Q_e}{R_{eff} T_{filter}} \approx 1.24 \times 10^{10}. \tag{3.4}$$

As the XUV spectrum with Zr filter inserted is centered around 100 eV (see Fig. 3.8b), the total XUV pulse energy can be approximated to

$$100 \times N_{ph}\ [\text{eV}] \approx 2 \times 10^{-7}\ \text{J} = 0.2\ \mu\text{J}. \tag{3.5}$$

In comparison with recently reported state-of-the-art XUV generation at similar photon energies around 100 eV (for example refs. [5, 102]), these results mark an improvement of the total XUV flux per pulse by at least two orders of magnitude.

Another common measure for the efficiency of harmonic generation is the ratio of the produced XUV energy per shot to the pulse energy of the driving laser. Inserting the above numbers one gets $\sim 5 \times 10^{-6}$, a very reasonable scaling factor for this type of highly nonlinear conversion process and exceeding earlier measurements with mJ-energy driving lasers by more than an order of magnitude [109].

3.4 Conclusion

In this chapter I have presented the first results of multi-mJ-driven HHG at the high-flux XUV beamline AS 6 for ultrafast nonlinear and pump/probe studies in the photon energy range around 100 eV. The home-built few-cycle, high-power driving laser together with the employed loose focusing geometry and accordingly large interaction volume for the process of HHG lead to an increase in XUV radiation intensity by 2 orders of magnitude compared to similar sources at these wavelengths.

We can make a simple estimation of the XUV intensity, that could already be reached with this set-up for a potential experiment. Since we measured a pulse energy of ~ 0.2 μJ in a mostly flat spectral region from about 80 to 120 eV, we can calculate the energy that is contained in a 10 % bandwidth around the spectral centre at 100 eV. The whole spectrum covers a range of $120 - 80 = 40$ eV, while 10 % at 100 eV are 10 eV, so that approximately 10/40 or a quarter of the measured energy is contained in this bandwidth, amounting to $\sim 0.2/4 \approx 0.05$ μJ. Assuming a pulse duration of ~ 1 fs, which is easily supported by the 10 % spectral bandwidth, and a spot size of ~ 2 μm in the focus we may derive the available XUV intensity on target. Similar spot

sizes have already been achieved by focusing a 30-nm-wavelength XUV beam with the help of an off-axis parabolic mirror [124] and can be improved much further by more sophisticated focusing techniques, e. g. like the ones proposed in [125, 126].

If we substitute the above numbers into the formula for the averaged optical intensity we obtain a value of $I_{XUV} \approx 4 \times 10^{14}$ W/cm^2, on par with the intensities used for first pump/probe experiments with XUV radiation in the slightly lower spectral region from $\sim$80–50 nm [127]. Still, more systematic tests of the optimum length and the density of the target gas medium together with possible quasi-phase-matching schemes [128–130] and a spectrally resolved characterization method of the generated high harmonic radiation will be necessary to further improve the XUV flux to the µJ-level. Nevertheless, the enhanced XUV yield demonstrated above shows that we successfully entered the intensity regime in which nonlinear optics takes place. Thus, the way to the reliable implementation of long anticipated XUV-pump/XUV-probe schemes for the investigation of inner-shell dynamics on the natural atomic time scale has been paved.

Chapter 4

Temporal characterization of a high-intensity X-ray source

Pulse duration measurement of the FEL beam at the LCLS (Stanford)*

Over the past few years, short-wavelength free-electron lasers (FELs) have established themselves as essential and unrivalled sources of ultrabright and tunable coherent X-ray radiation [23–26]. One of the key characteristics of these X-ray pulses is their expected ultrashort duration [60, 61, 132]. Combining the high spatial resolution and the ultrashort duration of X-ray pulses for a full four-dimensional characterization of the sample under scrutiny in a single shot has been a long-standing goal of material and biological science. These properties open the door to the highly anticipated investigation of a plethora of phenomena of considerable importance with nanoscale spatial and attoscale temporal resolution. Proposed areas of interest range from single-atom processes such as inner-shell multiple ionization, all the way to biological systems, such as four-dimensional studies of viral genomes, diffraction tomography of whole cells, scattering-based imaging of organic samples and the dynamics of photosynthetic reactions to the basic research of the properties of novel and exciting materials like graphene. However, so far no measuring technique has

*This chapter was built on the manuscript Helml *et. al.* [131] reporting these measurements and currently under review for publication in *Nature Photonics*.

been able to directly and precisely determine the structure or even the duration of these ultrashort pulses.

4.1 The Linac Coherent Light Source at the SLAC National Accelerator Laboratory

Since 2009 the Linac Coherent Light Source (LCLS) at the Stanford Linear Accelerator Center (SLAC National Accelerator Laboratory) is generating the worldwide first FEL radiation in the soft and hard X-ray regime [25]. Figure 4.1 shows the LCLS machine layout from the electron injector gun, with two electron bunch compressor chicanes, BC1 and BC2, up to the 132-m-long undulator. The whole electron acceleration distance is roughly one kilometer long.

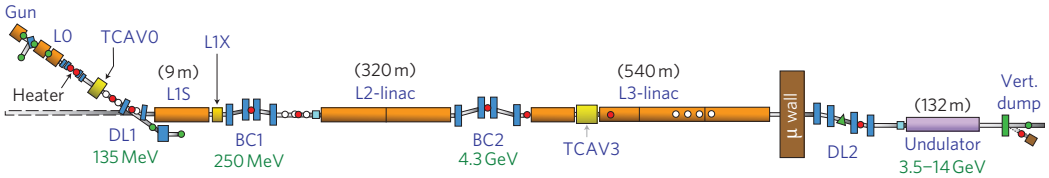

Figure 4.1: LCLS machine layout. (Figure reproduced from reference [25].)

This novel X-ray source has the additional advantage of being easily tunable both in photon energy — ranging from some hundreds of electronvolts (eV) up to nearly 10 keV — as well as in pulse duration. The achieved pulse duration is dependent on a number of parameters, that can be independently changed to compress the X-ray pulse from 500 fs to an expected shortest length of less than 10 fs. As one can see from table 4.1, there are two main modes that can be used for the operation of the FEL: a routine setting with an electron bunch charge of 250 pC and a so-called 'low-charge mode' with a much reduced bunch charge of only 20 pC. The higher bunch charge leads to an overall higher photon number in the generated FEL pulse, but due to the longer pulse duration compared to the FEL pulse expected from the low-charge mode the corresponding peak power is even higher for the 20 pC electron bunch charge. Be aware that these numbers for the ultrashort FEL pulse lengths are all derived from simulations. Since we were most interested in measuring the shortest possible X-ray pulses,

we performed our measurements in this low-charge mode.

Parameter[a]	20 pC	250 pC	Unit
Injector bunch length (rms)	1.3	2.5	ps
Initial peak current	5	30	A
Final bunch length (rms)	∼3	∼30	fs
Final peak current	∼3	∼3	kA
FEL pulse duration (FWHM)[b]	∼2	∼60	fs
FEL peak power[b]	∼400	∼20	GW

[a] FWHM stands for *full width at half maximum*, rms stands for *root mean square*

[b] Based on simulations with the GENESIS 1.3 [133] FEL code.

Table 4.1: LCLS machine parameters for the low bunch charge mode (20 pC) and a more routine setting with a higher bunch charge (250 pC), according to reference [134].

To reduce the pulse duration even further we made use of the so-called 'slotted spoiler' [27]. The working principle of this scheme is illustrated in Figure 4.2. A thin foil with a narrow vertical slit is introduced into the electron beam path in one of the magnetic bunch compressor chicanes and basically spoils the largest part of the electron bunch via Coulomb scattering. Only the small central slice of the bunch passes the foil unhindered through the slit and will subsequently experience efficient FEL amplification in the undulator. This method, in combination with the above described low-charge mode, is predicted to produce pulses with sub-femtosecond duration, consisting of only one single coherent X-ray spike stemming from a residual unspoiled electron bunch length on the order of the undulator slippage length (compare section 1.4.3).

As with any signal based on the self-amplified spontaneous emission (SASE) process (see section 1.4.2) the underlying temporal shape of each subsequent single FEL pulse at the LCLS is implicitly different from the previous one, demanding a single-shot measurement technique for its investigation. The attosecond streaking technique [135, 136] has been successfully employed for the temporal characterization of longer (∼ 40 fs) FEL pulses in the spectral re-

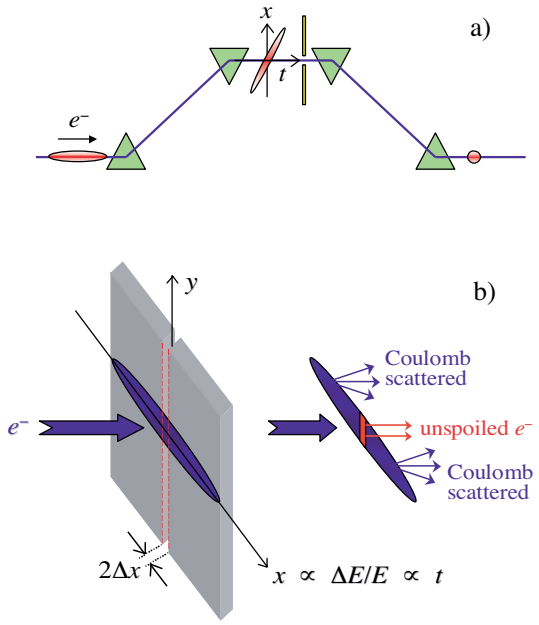

Figure 4.2: Sketch of the working principle of the slotted spoiler. (a) shows the electron bunch at the center of the compressor chicane and with a marked tilt with respect to the direction of propagation. In (b) the slotted foil is depicted, that leaves only a narrow central region of the bunch pass unspoiled. (Figure reproduced from reference [27].)

gion of the extreme ultraviolett (XUV) [137], utilizing inherently synchronized terahertz (THz) radiation as a streaking field at the Free-Electron Laser in Hamburg (FLASH) facility [23]. Recently, other measurements on soft X-ray pulses of similar pulse length have been conducted at the LCLS, again relying on the concept of streaking spectroscopy, but with an external NIR laser at a wavelength around 800 nm as a streaking field [138, 139].

Neither of these set-ups is capable of measuring the ultrashort X-ray pulse durations ($<$ 10 fs) predicted in the above described low-charge operating mode in combination with the slotted spoiler at the LCLS, because of lack of temporal resolution in the case of the THz streaking and due to the breakdown of the streaking regime for the case of the NIR laser, when the X-ray pulse duration is longer than half the oscillation period of the streaking field ($>$ 1.3 fs for a central carrier wavelength of 800 nm, compare section 4.2).

On the other hand, SASE FEL pulse durations have also been indirectly inferred from measurements on the electron bunch length before the undulator [134] or from statistical analysis on the spectral coherence properties of the ultrashort X-ray pulses [140]. Nevertheless, these characterization techniques cannot provide single-shot information on the temporal structure of the X-ray pulses and only statistically averaged quantities for possible pulse length predictions can be derived from these measurements. Furthermore, recent studies of fundamental ionization processes and measurements for longer X-ray pulses ($>$ 40 fs) have revealed a substantial deviation of the actual X-ray pulse duration from the one inferred from electron bunch length measurements [138, 141].

Thus, no direct experimental determination of the structure of these X-ray pulses in the time domain has yet been feasible. However, for many of the planned or future envisioned experiments at LCLS and other FELs, exact knowledge of the peak intensities of individual ultrashort X-ray pulses in the interaction region is of utmost importance, a prerequisite for which is precise information about the pulse duration. This fact holds especially true for any kind of time-resolved measurements that could give insight into the dynamics of reaction processes on the fundamental electronic time scale of only hundreds of attoseconds.

4.2 Basic principles of streaking spectroscopy

The method of choice to directly measure the ultrashort FEL pulse duration is the concept of streaking photoelectron (PE) spectroscopy, which is a well established technique for temporal characterization of attosecond pulses in the XUV spectral region. This scheme has been theoretically described in [135, 142] and been successfully demonstrated in numerous time-resolved measurements, e. g. [4, 136, 143]. The essential parts of the theory for the purpose of the temporal FEL pulse characterization shall be briefly discussed in the following section. Throughout this discussion for the rest of the chapter atomic units [au] are used (see section 1.2.1).

In the streaking spectroscopy set-up the FEL X-ray pulse is focused into an interaction volume filled with a rare gas, where it is temporally and spatially overlapped with an IR pulse, both horizontally polarized. The X-ray pulse ionizes a small fraction of the gaseous atoms, thereby liberating the generated photoelectrons with a kinetic energy $\epsilon_c = \hbar\omega_{X-ray} - I_p$, with ω_{X-ray} being the angular frequency corresponding to the X-ray photon energy and I_p the ionization potential of the atom's electronic state. Ignoring the IR field for the moment and on the condition of $\hbar\omega_{X-ray} \gg I_p$, the electron is rapidly moving away from the ion with velocity $v_c = \sqrt{2\epsilon_c}\,/\,m_e$, so that the Coulomb potential can be neglected.

If the photoelectron is born into the presence of a strong IR laser field (subsequently referred to as a *streaking* field), it feels the influence of the corresponding electric field and suffers a change in its final velocity. The final electron velocity under this circumstances can be expressed most conveniently with the help of the vector potential (compare section 1.2.1) by

$$v(t_b) = v_c - eA_{IR}(t_b), \tag{4.1}$$

where $A_{IR}(t_b)$ is the IR vector potential at the time t_b of the birth of the electron.

Since there is a monotonous slope of the vector potential between neighboring extrema for any half-cycle period of the streaking field, there is a direct mapping of the temporal profile of the ionizing FEL pulse to the velocity distribution of the generated photoelectrons. Obviously, this scheme works only,

when the duration of the X-ray pulses becomes comparable to or is ideally shorter than the IR laser half-cycle period. In this case, electrons generated at different delays between the FEL and the IR pulse 'feel' a well-defined and time-dependent variation of the amplitude and the slope of the laser's vector potential, so that some photoelectrons are decelerated while some are accelerated.

On the contrary, if the ionizing X-ray pulse is longer than the streaking laser period, this modulation of the photoelectron spectrum is repeated identically every optical cycle, destroying the one-to-one temporal mapping and leading to the emergence of spectral sidebands spaced by $\hbar\omega_{IR}$ [138, 144, 145].

The overall shift $\Delta\epsilon(t)$ of the photoelectron spectrum can be calculated using the approximation formula [135, 146]

$$\Delta\epsilon(t) = -p_c A_{IR}(t) + \frac{1}{2}A_{IR}^2(t), \tag{4.2}$$

where $p_c = \sqrt{2\epsilon_c}$ is the momentum corresponding to the central energy of the unstreaked photoelectrons. When the peak vector potential of the employed streaking field is much smaller than the initial momentum of the generated electrons, $A_{peak} \ll p_c$, then the second term in eq. (4.2) can be neglected and the equation is further simplified to

$$\Delta\epsilon(t) \approx -p_c A_{IR}(t). \tag{4.3}$$

Since this condition is easily met by our experiment, where the peak vector potential $A_{peak} \simeq 0.18$ au and the initial photoelectron momentum $p_c \sim 5.8$ au, equation (4.3) is applicable to our experiment. This way, the electrons become strongly redistributed in kinetic energy, resulting in a significant change in their final energy spread and central energy with respect to the unstreaked spectrum (see Fig. 4.3), thus providing direct, single-shot time-domain information on the X-ray pulse duration.

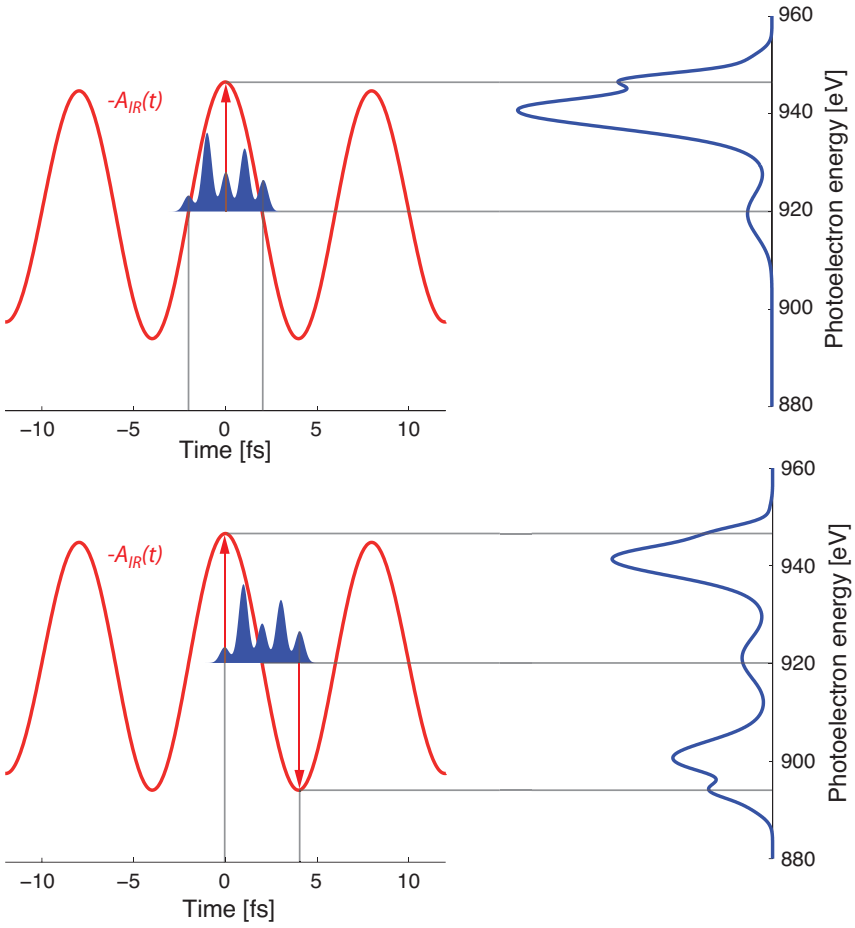

Figure 4.3: Basic concept of streaking measurements on few-femtosecond FEL pulses. Depicted is the temporal overlap of a 4 fs FEL pulse (blue filled area, representing the X-ray pulse intensity envelope) and a longer ($\sim$ 50 fs) IR pulse with a central wavelength of 2.4 µm, i. e. an optical cycle-period of 8 fs. In the interaction region photoelectrons from a rare gas are liberated by the FEL X-ray pulse with a certain excess kinetic energy ϵ_c. Subsequently the electron is treated as a free particle in the continuum and only 'feels' the influence of the IR streaking field. If the photoelectron bunch coincides with a maximum of the IR vector potential $A_{IR}(t)$, the electrons are mainly shifted to higher or lower energies, but the whole distribution is only slightly broadened (upper panel). On the other hand, if the overlap happens during a zero-crossing of the vector potential, the photoelectrons are redistributed over a broad spectral range, while the central energy is not changed at all (lower panel).

4.3 The instrumentation at the AMO hutch

We performed the measurements at the atomic, molecular and optical science (AMO) instrumental end-station at the LCLS [147]. It comprises a vacuum chamber inside which an optical laser co-propagates with the FEL. Both beams are focused into the same interaction region where a nozzle emits a jet of neon gas. In addition, the instrumentation incorporates a magnetic bottle electron spectrometer (MBES) [148], a high collection efficiency spectrometer that operates over a broad energy range capable of detecting the photoelectron spectra for every single shot.

4.3.1 Experimental set-up and alignment

Figure 4.4 shows a sketch of the experimental set-up and illustrates the basic principle of streaking. The X-rays eject electrons from the gas atoms via the photoelectric effect, and set them free with a kinetic energy equal to the X-ray photon energy minus the specific electron binding energy of the atom. These photoelectrons can be described as free electron wave packets for our experimental conditions. The temporal structure of the generated photoelectron wave packet mimics that of the incoming FEL pulse and its width is directly related to the X-ray pulse duration [149].

The streaking laser was based on an optical parametric amplifier (TOPAS-C, Light Conversion). We used the idler wave tuned to 2.4 μm central wavelength, with horizontal polarization of the electric field, a pulse energy of ~ 30 μJ and a compressed pulse duration of ~ 50 fs full width at half maximum (FWHM), measured by a custom-built second-order autocorrelator. The output beam of the IR laser was suitably enlarged by a telescope, then transported to the experimental chamber by reflection on silver mirrors and subsequently focused through a 2 inch CaF_2 lens to a beam diameter of ~ 450 μm in the interaction region, yielding an optical intensity on target of roughly 4×10^{11} W/cm^2 or a corresponding peak vector potential of the streaking field of $A_{peak} \simeq 0.18$ au. The coupling into the FEL vacuum beamline was accomplished by passing the beam through a CaF_2 window, glued to a flange cut at Brewster's angle to minimize reflective losses, and reflection off a mirror mounted at 45 degrees with respect to the X-ray propagation direction with

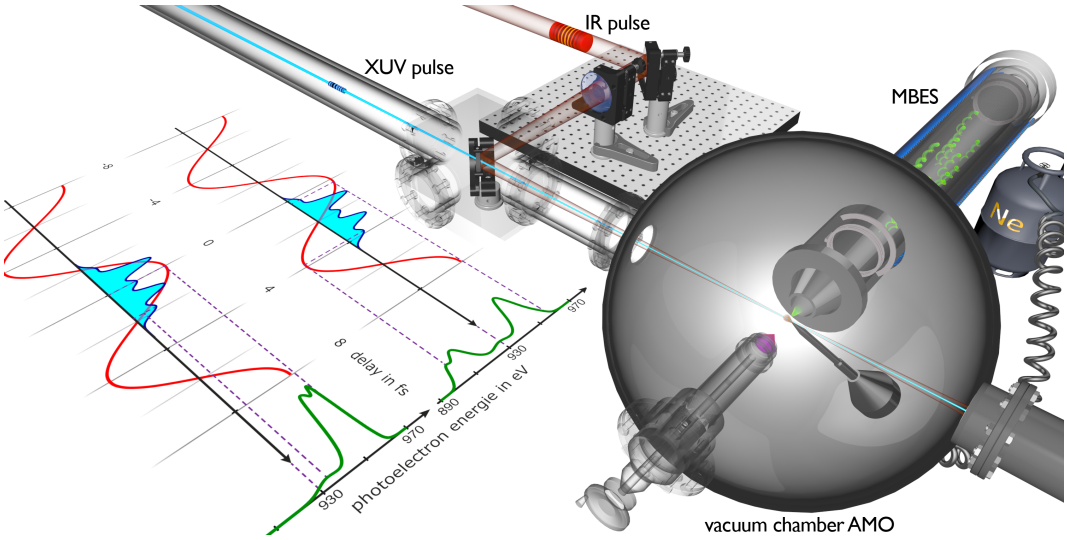

Figure 4.4: Experimental set-up and measurement principle. The picture shows the experimental set-up in the AMO hutch at the LCLS. The X-ray laser and the IR streaking laser are coupled into the vacuum chamber and are co-linearly focused onto a Ne gas target. The generated photoelectrons are then energy resolved with a magnetic bottle electron spectrometer (MBES). The inset on the left depicts two distinctive cases of temporal overlap of the FEL with respect to the streaking field, one at the zero crossing and one at a maximum of the IR vector potential. The respective photoelectron (PE) spectra are also shown. More details are given in the text and in Fig. 4.3.

a hole in the middle, through which the FEL beam passed. As a target for photoexcitation we used neon gas streaming from a nozzle with a background pressure in the experimental chamber of $\sim 1 \times 10^{-7}$ mbar and the photoelectrons were detected with the MBES.

For our streaking experiment we had to carefully overlap the FEL pulse with the IR laser spatially and temporally. Separately looking at the images on a YAG screen in the interaction region and then aligning the two beams to the same spot provided us with the spatial overlap position. Rough temporal overlap was then achieved by synchronizing the arrival times according to the signal from a fast photodiode in the beam path. Then we did a fine-scan by changing the length of the path of the optical laser in small steps and integrating the electron detection signal in an energy region close to the photoline. The better the FEL and the IR laser are synchronized, the more electrons see the IR field and the detected electron spectrum deviates from a pure photoline. This signal can be used to find the maximum temporal overlap.

4.3.2 FEL settings

The LCLS was working in the so-called 'low-charge mode', with an electron bunch charge of 20 pC around the point of maximum compression at $\sim$10 kA, producing FEL pulses expected to be of sub-10 femtosecond duration and with photon energies tuneable from 800 eV to 2000 eV at a repetition rate of up to 120 Hz [25]. In order to further minimize the FEL pulse duration, a 'slotted spoiler' [27] was inserted into the electron beam at the second bunch-compressor chicane along the SLAC Linac ahead of X-ray generation in the undulator. We measured various characteristics of the FEL: That the X-ray central energy varies slightly from shot to shot is manifest as an energy shift of the photoline peak that we detected in the MBES. With an FEL photon energy of $E_\gamma = 1790$ eV and a binding energy of $E_B = 870$ eV for the 1s electron shell in neon, the central energy of the photoelectrons is distributed around the mean value of 920 eV with a standard deviation of ~ 2 eV root mean square (rms). The bandwidth of the photoline, corresponding to the energy spread of the X-ray pulse, was measured to be $\sim$3.3 eV rms.

4.3.3 Magnetic bottle electron spectrometer (MBES)

The magnetic bottle electron spectrometer consists of a 1 m-long drift tube surrounded by a solenoid creating a constant low magnetic field, and a strong 0.5 T permanent magnet. Together, they create a magnetic field capable of collecting and guiding a large portion of the photoelectrons and Auger electrons created in the interaction region. Since every electron with the same initial energy arrives at the end of the drift tube at the same time, a simple time of flight treatment yields the electron energy spectrum. An electrostatic retarding potential is used to slow down the electrons and improve the energy resolution that ends up being limited by the time response of the micro channel plate detector. The final resolution corresponds to around 0.5 % of the initial energy, e. g. around 4 eV FWHM when operating the FEL at 1800 eV. A small aperture is used to limit the acceptance solid angle ($\sim 30°$ at the energies used in the experiment). Combined with the sharply peaked angular distribution of the 1s photoelectrons that are used in the measurement, this ensures that the streaking method can be used without loss of resolution due to integration over a large range of angle and thus streaking strengths.

4.4 Direct time domain measurement of ultrashort X-ray pulses

Here, we apply this technique for the first time to hard X-ray pulses. In this approach, an externally synchronized IR laser field is overlapped with the X-ray pulses and both beams are subsequently focused into a gas target. One of the major challenges for these types of correlation measurements is the arrival time jitter of each single FEL pulse with respect to the IR laser. With our scheme and following analysis we overcome this issue and derive an upper limit of the X-ray pulse duration for each single shot in a manner that is decoupled from all machine parameters and can be used simultaneously with any ongoing measurement.

Before presenting the details of our evaluation it is an important prerequisite for the following analysis to make an estimate of the X-ray pulse duration compared to the streaking laser period. Following the previous reasoning, for

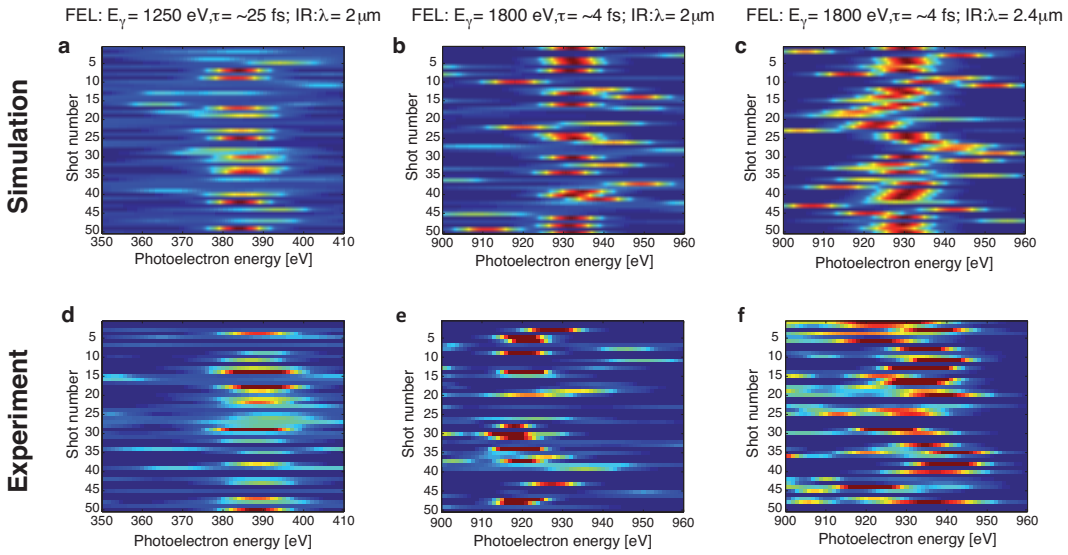

Figure 4.5: Streaked X-ray photoelectron spectra (top: Simulation, bottom: Experiment). Six colour-coded intensity plots for photoelectron spectra of 50 consecutive shots, for two different X-ray pulse durations ($\tau_{X-ray} \approx 25$ fs and $\tau_{X-ray} \approx 4$ fs) streaked by optical lasers with two different central wavelengths ($\lambda = 2$ μm and $\lambda = 2.4$ μm). Fig. 4.5 a to c are simulations, while d to f are constructed from the corresponding measurements taken at the LCLS during our experiment. The long 25 fs X-ray pulses (panels a and d) exhibit nearly no spectral shift but rather uniform smearing of the PE spectra, revealing that for these long pulses our measurement method breaks down. A similar behaviour can also be observed for the short X-ray pulses (< 5 fs) when streaked with the 2 μm IR field, shown in the middle in panels b and e: the ratio of the period of one optical cycle at this wavelength to the X-ray pulse duration is still not optimal, resulting in a high probability to find the spectral centre near the unstreaked value. In contrast, for the 2.4 μm streaking field, right panels c and f, the whole spectrum is hugely shifted away from the mean, as is expected when the PEs 'see' only part of the IR vector potential, a clear demonstration of the onset of the streaking regime. Note that the overall shift of the central energy in panels e and f from 930 eV to 920 eV is due to an accordingly lower X-ray photon energy (1790 eV instead of 1800 eV) for this measurement and is not a streaking effect.

longer X-ray pulses (enclosing one or more cycles of the streaking field) the energy shift of the streaked photoelectron spectrum is negligible, thereby resulting in uniformly larger streaked spectral widths. This is evident when looking at the spectra presented in Fig. 4.5 a and d, which show 50 simulated (a) and measured (d) streaked spectra obtained with X-ray pulses stretched to around 25 fs (by changing the compression of the electron bunch) and a streaking field with a wavelength of 2 μm. For the X-ray pulses at optimized compression and inserting the spoiler [27], we can see in Fig. 4.5 b and e that when employing the same 2 μm streaking laser, the situation is globally unchanged, whereas when using a 2.4 μm wavelength IR laser, we observe the apparition of a clear streaking regime [9, 136] (Fig. 4.5 c and f). Thus we have demonstrated that the FEL pulses under these experimental conditions are at least shorter than 8 fs (one period at 2.4 μm wavelength) and we can apply the streaking concept for the X-ray pulse duration acquisition.

4.4.1 Single-shot X-ray pulse duration measurement

The FEL and the streaking laser were externally synchronized with a timing jitter that we determined by a cross-correlation measurement between the two lasers (see Figure 4.6). By changing the delay between the two pulses and integrating the measured signal over an area of the PE spectrum that lies just beside the main unstreaked photoline we get a time-dependent measure of the strength of the overlap. With this method we found an arrival time jitter of ~ 90 fs rms for our set-up (Fig. 4.6 c). Since the arrival time jitter between FEL and IR is of the same order as the IR pulse duration, it is not possible to assign a definite delay and corresponding value of the vector potential with respect to the streaking field to each single FEL pulse.

Furthermore, due to the statistical nature of the SASE process (compare section 1.4.2) the actual pulse shape and thus the duration of consecutive FEL pulses also varies from shot to shot, necessitating a single-shot measurement technique for its determination. That means that we have to adopt a different method to extract the X-ray pulse duration from the measured spectra than what is conventionally used in streaking experiments with precisely synchronized gas-phase high harmonic sources. As the relative phase between the X-ray pulse and the streaking field is not known a priori, we have, in a first

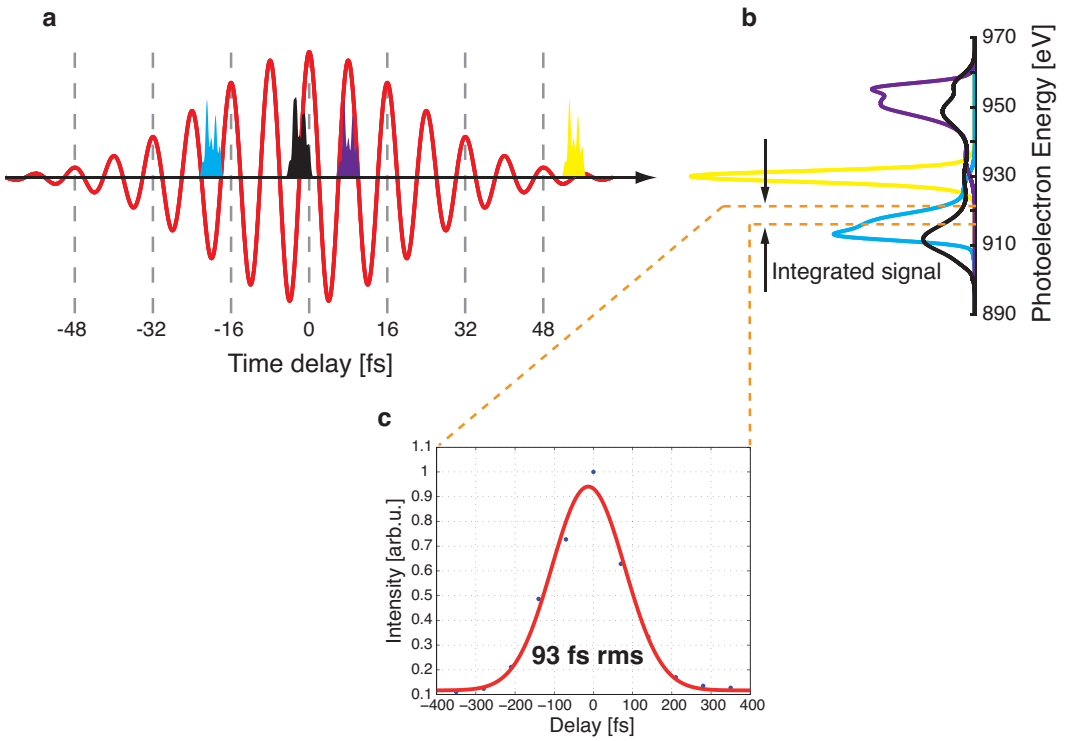

Figure 4.6: Determination of FEL–IR arrival time jitter. Figure 4.6 panels a and b show the simulation of X-ray pulses (blue, black, purple & yellow) overlapping with the IR streaking field (red) at different relative delays and the corresponding photoelectron spectra. Panel c depicts the measured cross-correlation obtained by integrating the signal over a small region of the spectrum at a point $4\,\sigma$ away from the unstreaked photoline for different delay settings. In the case of very poor overlap (the situation depicted as the yellow FEL pulse in panel a) there is nearly no streaking effect: the measured photoline stays narrow and the signal in the region of interest is small. As the X-ray pulse overlaps more and more with a vector potential of higher amplitude (the cases of the blue, purple and black pulse, in ascending order of streaking potential amplitude), the generated PE spectra become ever more broadened and the integrated signal rises accordingly. Therefore, the detected width of this cross-correlation can be interpreted as a measure of the average effective arrival time jitter between the FEL and the streaking field, which amounts to $\sim$93 fs rms in our case.

step, to determine the value of the streaking vector potential for each single FEL pulse. This fact is critical for our analysis and leads to the determination of an upper limit of the X-ray pulse duration. In the second step we use this vector potential as a calibration factor to convert the measured spectral width of each streaked photoelectron wave packet into the duration of the corresponding X-ray pulse.

For the first step of our evaluation we assume that the detected peak of the spectrum that is pushed farthest away from the unstreaked centre stems from an overlap of the X-ray pulse with a local maximum of the vector potential. This way, we will on average underestimate the gradient of the vector potential, thereby overestimating the underlying FEL pulse length and deriving an upper limit for the associated pulse duration. To illustrate the principle of evaluation let's have a look at an example from our data, sketched in blue in Figure 4.7 a. In this case we have measured a streaked spectrum ranging from 915 to 945 eV, corresponding to a width of the streaked spectrum of $\delta_s = 30$ eV and a maximal energetic shift in relation to the unstreaked photoline at 920 eV of $\Delta\epsilon = 945 - 920 = 25$ eV. Following ref. [146], we estimate the vector potential $A_{IR}(t)$ of the streaking field as approximately linear in time,

$$A_{IR}(t) \approx -E_{peak} \times (t - t_{peak}), \tag{4.4}$$

with a slope given by the peak electric field $E_{peak} = E(t_{peak})$ of the half-cycle that the photoelectrons are overlapping with, which occurs at the moment t_{peak}. The period of the streaking laser was $t_{period} = 8$ fs, setting the time interval for the vector potential to rise from a zero-crossing to a maximum (a quarter period) to 8 fs/ 4 = 2 fs. This value corresponds to the above calculated maximum shift $\Delta\epsilon = 25$ eV in the energy domain. Now we can use the measured width of the streaked spectrum, $\delta_s = 30$ eV, as a ruler for the pulse length, resulting in an upper limit for the X-ray pulse duration:

$$\tau_{X-ray} = \frac{\delta_s}{\Delta\epsilon} \times \frac{t_{period}}{4}. \tag{4.5}$$

This gives $(30/25) \times (8/4) = 2.4$ fs in our case, represented by the blue X-ray pulse on the left in Fig. 4.7 a. There is, in addition, a residual ambiguity in our analysis method that we have to consider. Figure 4.7 a shows schematically a second FEL pulse (green, in the middle) with a different duration that

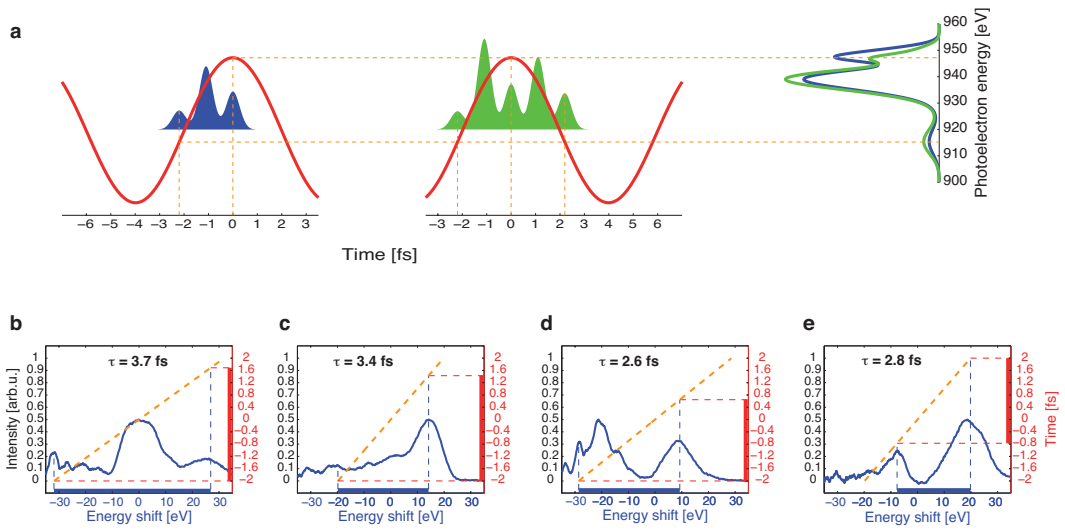

Figure 4.7: Streaking of few-femtosecond X-ray pulses. The top panel, Fig. 4.7 a, shows the principle of the X-ray pulse duration evaluation: the maximal shifted peak of the measured PE spectrum is associated with an overlap of the X-ray pulse with a local maximum of the streaking field (blue pulse on the left). This energy shift $\Delta\epsilon$ defines the gradient of the energy-to-time conversion and the overall width δ_s of the streaked spectrum is used for the determination of the FEL pulse duration. The green X-ray pulse, twice as long and depicted in the middle, gives rise to a very similar PE spectrum, leading to a residual ambiguity of the FEL pulse length measurement. Panels 4.7 b–e show four different streaked photoelectron spectra as measured in our experiment (blue solid lines) at different values of the IR vector potential and the respective linear streaking ramp (orange dashed lines) derived from the maximum shifted peak of the spectrum. In panel b we infer a maximal shift $\Delta\epsilon = |-32|$ eV from this peak, i. e. the laser half-cycle of 4 fs is mapped onto an energy range of $2 \times \Delta\epsilon = 64$ eV. The complete spectrum spans from -32 eV to 27 eV, setting the overall width to $\delta_s = 59$ eV and corresponding to a pulse duration of 3.7 fs. In a similar manner we derive upper limits for the other pulse durations of 3.4 fs (panel c), 2.6 fs (panel d) and 2.8 fs (panel e), respectively. Considering the ambiguity of the energy-to-time mapping all those shots are in principle also compatible with the doubled pulse length (see text).

nevertheless leads to the same measured width of the streaked spectrum. Since we assumed that the X-ray pulse partly overlaps with a local maximum of the vector potential, we cannot discern streaking effects caused by the right or the left edge of this vector potential curve. To get a correct upper limit for the possible X-ray pulse duration, we therefore must double the above calculated value to 4.8 fs. All pulse lengths between 2.4 fs and 4.8 fs are compatible with our measurement.

Owing to the statistical nature of the SASE generated FEL pulses originating from noise, the x-ray pulse profile differs greatly from shot to shot. For the first time, we are able to show this variation and demonstrate the intensity substructure of the FEL pulses directly in the time domain, with a resolution better than the coherence length. Figure 4.7, panels b–e, show the comparison of the unstreaked photoline (dashed blue) with measured X-ray pulse profiles (red). In Fig. 4.7 b an FEL pulse consisting of only one single peak overlaps with the zero crossing of the vector potential and is broadened compared to the photoline. Different arrival times of the FEL pulse relative to the streaking laser lead to an overall shift of the whole spectrum as depicted in Fig. 4.7 c and d, where the FEL pulse overlaps with the positive or negative part of the vector potential and the resulting spectrum is shifted accordingly. An individual peak followed by a tail (c) can be distinguished from a pulse containing two well separated spikes (d) or even three individual spikes as shown in Fig. 4.7 e.

If we repeat this analysis for each single shot and plot the number of shots versus the respective pulse durations they are in agreement with, we get an estimation of the average X-ray duration (Figure 4.8). We find that the average pulse duration of the FEL is best fitted by a gaussian distribution with a mean value of 4.7 fs and a standard deviation of 1.7 fs. We emphasise here that this is obviously a very conservative upper limit and that the actual pulse duration is likely to be considerably shorter for the vast majority of LCLS pulses in this mode of operation.

4.4.2 Measurement of sub-femtosecond X-ray pulses

Due to pulse-to-pulse fluctuations there are some pulses that are considerably shorter than the average duration. FEL theory predicts a temporal pulse substructure composed of a train of ultrashort spikes [61] with a typical width

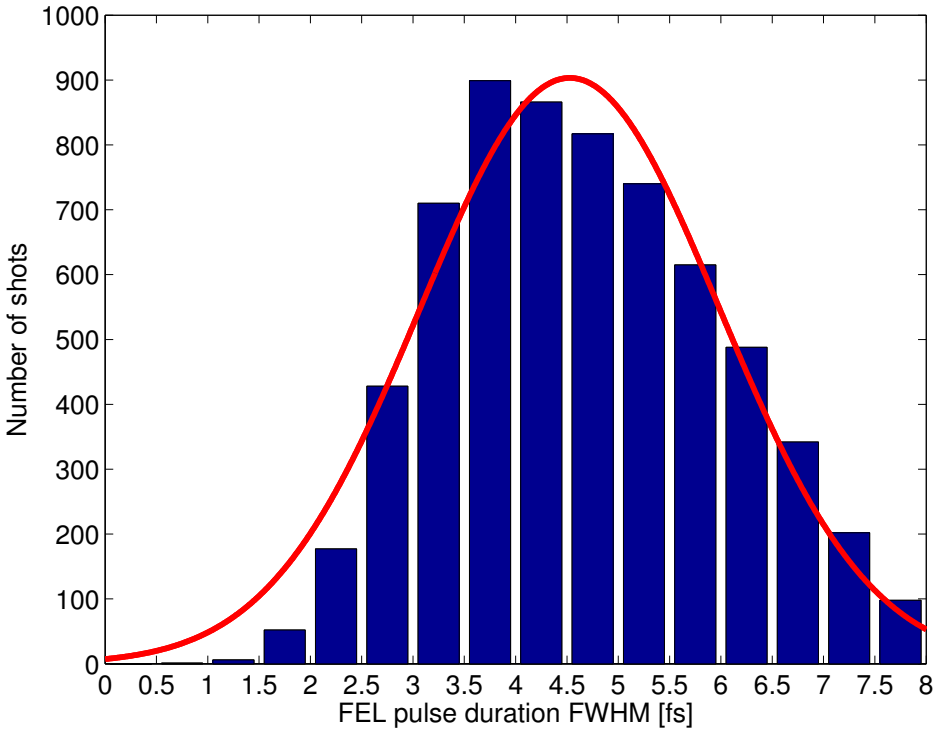

Figure 4.8: Average FEL pulse duration. A histogram of the possible pulse duration values in agreement with our measurement (blue) for the parameter range we were working with at LCLS (20 pC low-charge mode, 1790 eV X-ray photon energy, electron bunch nearly fully compressed at 10 kA, slotted spoiler inserted into the electron beam path). The red solid line shows a Gaussian fit to the distribution, indicating an upper limit for the average X-ray pulse duration of $\sim$4.5 fs.

corresponding to the coherence time, characterized by the X-ray photon energy bandwidth and machine specific parameters (see section 1.4.3). For the parameter range we were working at during our measurements at the LCLS, spike durations of about one femtosecond and even below are expected to occur (compare for example ref. [134]). The average number of spikes per FEL pulse can be estimated, but it will also be subject to shot-to-shot variations. Occasionally, an X-ray pulse consisting of just one single isolated spike will occur.

A closer analysis of our data has confirmed the existence of such ultrashort 'single-spike' pulses, constituting about 5 % of the total number of shots for the run we analysed. By sorting and collating the streaked spectra with just one peak and determining their centres we can identify the energy shift $\Delta\epsilon$ and the spectral width δ_s for each of these shots. Figure 4.9 shows the measurement principle for attosecond X-ray pulses: For the evaluation of these single-spike pulses we assume that due to simple statistical considerations the predominant number of FEL shots overlaps with a part of the ramp of the vector potential and hence again equation (4.4) is valid. Then we can employ a reasoning similar to that described above to assess an upper limit for the pulse duration. In order to not overestimate the actual value of the vector potential for the conversion into the time domain we use the minimum possible value of the vector potential, that is the value that corresponds to the observed shift of the central photoelectron energy for each of these single-spike pulses. This is a very conservative approach and will again result in the determination of an upper limit for the respective pulse duration.

In the case of one shot I have selected from our data (Fig. 4.9) this energetic shift amounts to $\Delta\epsilon = 17.4$ eV and is marked as the bigger light blue dot in panel b. Following deconvolution of the initial unstreaked X-ray photon energy bandwidth, which was determined by separate measurements, from the measured signal and using $\Delta\epsilon$ as a calibration factor the spectral bandwidth of this single peak corresponds to an X-ray pulse with a duration of maximum $\sim$800 attoseconds FWHM. In general, the derived upper limits for the duration of X-ray single-spike pulses are mainly in a range of 750 to 1500 as FWHM (marked by the green oval in Fig. 4.9 b), which is in good agreement with the predictions based on equations for the SASE process under the conditions of

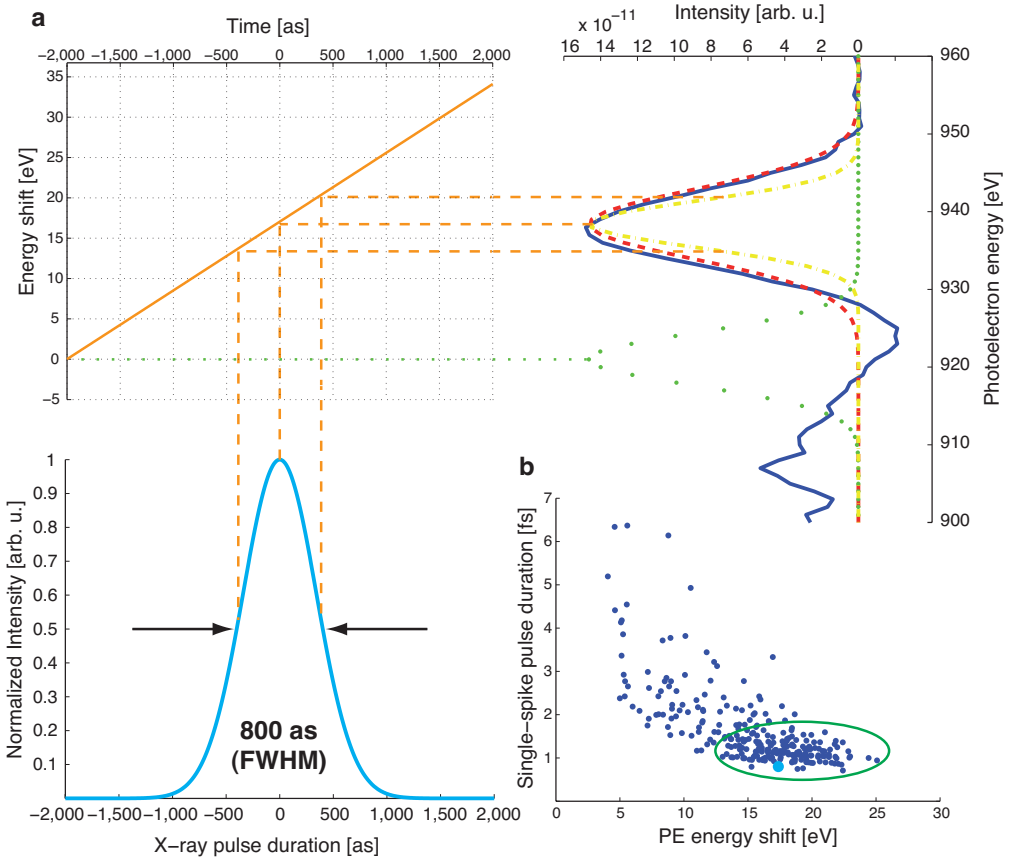

Figure 4.9: Measurement of an attosecond X-ray pulse. Panel a on the right-hand side shows a measured spectrum of a single FEL intensity spike (solid dark blue line) and the corresponding Gaussian fit (dashed red line). The shift of the peak from the unstreaked central energy at 920 eV (green dotted line) defines the energy-to-time ramp (top left), with the help of which the width of the deconvoluted spectrum (yellow dashed-dotted line) can be converted into a pulse duration upper limit of ~ 800 as, depicted as the light blue line on the bottom left. Panel b at the bottom right shows the derived upper limits for the pulse duration of all single-spike shots in one run that we analysed as a function of the spectral energy shift of the peak. The very short pulse described in panel a is marked as the bigger light blue dot. The outliers towards longer pulse durations are all associated with small energy shifts (≤ 5 eV), and therefore potentially stemming from an underestimation of the actual streaking vector potential by our method. Nevertheless, most of the measured single-spike X-ray pulse durations are in the region of one femtosecond and below, highlighted by the green oval.

the LCLS machine parameters [134].

4.5 Conclusion

In conclusion, we have experimentally demonstrated that the FEL X-ray source at LCLS is capable of producing high-energy, ultrabright pulses with an average duration of only a few femtoseconds. Our method of streaking spectroscopy allows us, for the first time, to conduct consecutive single-shot measurements of these ultrashort X-ray pulses directly in the time domain with attosecond resolution and independent of the photon energy. We determined an upper limit for the pulse duration of each single FEL shot and showed that a statistical evaluation yields a characterization of the average pulse duration for a given setting of the machine parameters of the FEL. In addition, we were able to investigate the substructure of these pulses and confirm the expected behaviour of an underlying train of ultrashort single-spikes for these SASE FEL pulses. The duration of these single X-ray pulses was measured to be in the order of hundreds of attoseconds, in good agreement with theoretical predictions.

The set-up as described above only requires a tiny portion of the available FEL power and is therefore suitable as a real-time diagnostic that can be used online and parasitically in parallel with an active experiment. Streaking spectroscopy therefore is an ideal technique for tagging the pulse duration of each subsequent FEL pulse during an ongoing measurement, with the potential of providing complete information on the X-ray pulse structure for future pump-prope and all other intensity dependent experiments. This would enable the development of a versatile, ultrabright X-ray instrument with tunable photon energies and pulse durations for the investigation of a wide range of physical and biological systems and molecular reaction dynamics with nanoscale spatial and attoscale temporal resolution.

Summary & Outlook

The new and exciting field of attosecond science is developing rapidly to be one of the main research areas for time-resolved measurements on the dynamics of such diverse systems as inter-shell electronic motion of single atoms, dissociation and charge transfer of complex molecules, formation and change of electronic band structure and collective excitations like plasmons in solid-state matter and even intricate reactions of live biological samples, such as proteins, viruses and whole cells. The instruments necessary for the scientific investigation of all these subjects are provided by novel laser sources, generating ultrashort pulses in the femtosecond and attosecond range with wavelengths from the near-infrared down to the hard X-ray regime, corresponding to photon energies of a few electronvolts to a few kiloelectronvolts.

Since these topics represent scientifically uncharted territory, the involved methods still face some serious challenges and limitations and are thus subject to ongoing improvement. In this thesis I have studied two distinctive schemes for a future broader applicability of ultrafast laser spectroscopy as a reliable and multifunctional tool for attosecond time-resolved investigations. Both techniques are applicable on few-cycle laser pulse based set-ups, that are comparably cheap and space-saving in contrast to large-scale FEL facilities and provide so-far-unrivalled temporal resolution:

- The first approach discussed in chapter 2 was concerned with the increase of the achievable photon energies by pushing the efficient conversion to shorter wavelengths corresponding to energies in the water window ($\sim$ 284–535 eV) or even beyond into the keV regime. This was accomplished by utilizing a few-cycle, longer-wavelength 2.1 µm mid-infrared laser as the driver for the process of high-order harmonic generation, thereby taking advantage of the favorable scaling of the generated high-

est harmonic energy with the square of the driving laser wavelength. We demonstrate the extension of the high-energy cutoff up to 1.6 keV, in good agreement with theoretical predictions. In addition we could, for the first time, experimentally observe direct inner-shell ionization in neon by the recolliding electron, temporally confined to the ultrashort time window of a small interval around one extremum of the fundamental driving field. This ultrafast excitation in combination with the precisely synchronized fundamental laser as a 'trigger' pulse opens the door to the investigation of electronic motion between inner shells of atoms with attosecond resolution.

- The second project dealt with the enhancement of the available XUV flux as a fundamental prerequisite for pump/probe experiments and other nonlinear optical studies that require high photon intensities and was presented in chapter 3. By building a dedicated beamline for the implementation of a lose-focusing geometry with a high-power ~ 100 mJ, few-cycle laser system as a front end we were able to achieve the intensity necessary for efficient HHG in neon over a focal region approximately 100 times as large as the area used with conventional Ti:sapphire-based ~ 100 μJ driving lasers. We managed to amplify the XUV flux per pulse in the region around 100 eV by roughly two orders of magnitude, already providing a potential intensity on target of $I_{XUV} \approx 4 \times 10^{14}$ W/cm^2 and thus enough power for highly anticipated nonlinear measurements in the XUV spectral range.

The brightest coherent X-ray sources to date are free-electron lasers based on the SASE principle that provide orders of magnitude more photons per pulse than any current HHG set-ups. To demonstrate that these FELs can also deliver the ultrashort pulses necessary for time-resolved measurements or experiments depending on high peak powers, we characterized the pulses from the LCLS when it was operated in the so-called low-bunch mode and with the 'slotted spoiler' inserted into the electron beam path. The technique of *attosecond streaking spectroscopy* allowed us to measure the structure of these FEL pulses directly in the time domain on a single-shot basis, which is important since the pulse durations change from shot to shot due to the

generating process by self-amplified spontaneous emission. We found out that the average pulse duration in this mode of operation at LCLS has an upper limit of ~ 4.7 fs and that some of the pulses, consisting of only one intensity sub-peak, are even considerably shorter. Among these single-spike pulses, that make up approximately 5 % of all shots for the run during which we did our experiments, are a few with an upper limit on the pulse duration that lies even below one femtosecond, comprising, to our knowledge, the first directly measured attosecond FEL pulses.

These results broach a multitude of interesting prospects for future research activities. On the one hand the demonstrated scalability of the high-energy cutoff of high harmonic radiation with driver laser wavelength and the possibility to enhance the photon flux per pulse with recently developed high-power, few-cycle OPCPA systems in a loose-focusing geometry set-up pave the way to utilize HHG as a tool for the investigation of hitherto inaccessible scientific subjects at comparably low costs and space requirements. This list includes the study of organic samples with ultrashort soft X-ray pulses in the water window, XUV pump/probe measurements, experiments on amorphous materials that recover the complete structural information about an object under scrutiny in a single-shot before radiation damage takes place and a host of other highly intensity-dependent nonlinear measurements in the spectral region beyond 100 eV.

On the other hand, with the presently available SASE FELs and even more so with the new facilities under construction or in the planning stage all over the world there already exist unique instruments for ultrafast time-resolved X-ray spectroscopy. In combination with a precisely synchronized trigger pulse and the shot-to-shot knowledge of the FEL pulse duration gained by the methods described in chapter 4 of this thesis these machines permit pump/probe measurements with unprecedented X-ray intensities and corresponding high signal-to-noise ratio.

It is therefore a natural coarse of action to go a step further and put this scheme to a test. In the frame of a Marie Curie Fellowship I will conduct a proof-of-principle experiment at the LCLS. In this project a few-cycle UV pulse initiates a reaction in an ensemble of aligned oxygen-containing molecules and the synchronized X-ray pulse is used as a probe, in effect sampling the cor-

related dynamics of the oxygen valence electrons in real-time. The proposed measurement will be able to determine these reactions on a 10-femtosecond-scale and would be a first step in the development of a completely new field of ultrafast X-ray pump/probe physics. Future examples encompass time-resolved studies of the optical response of graphene to high-intensity X-rays, the real-time observation of the electronic dynamics involved in the process of photosynthesis or the investigation of the structural evolution of living cells, thereby promoting such diverse fields of research as materials science, chemistry and biology to a level of examination with nanoscale spatial resolution and femtoscale temporal resolution.

Appendix A

Build-up of the beamline AS 6

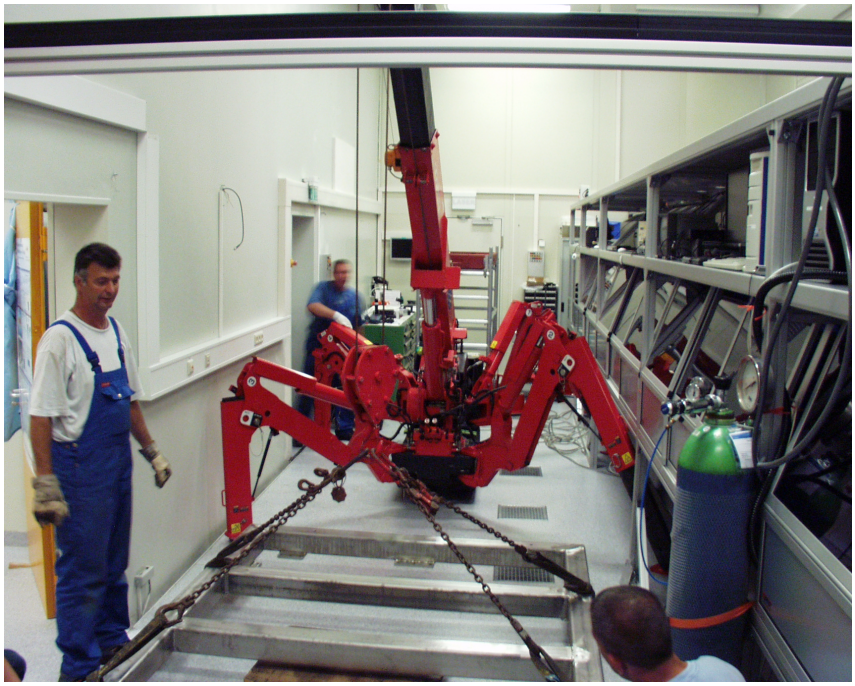

Figure A.1: The crane is ready to install the beamline in the cleanroom.

Figure A.2: Lifting a few hundred kilogram of steel frame above a sensitive high-power laser system.

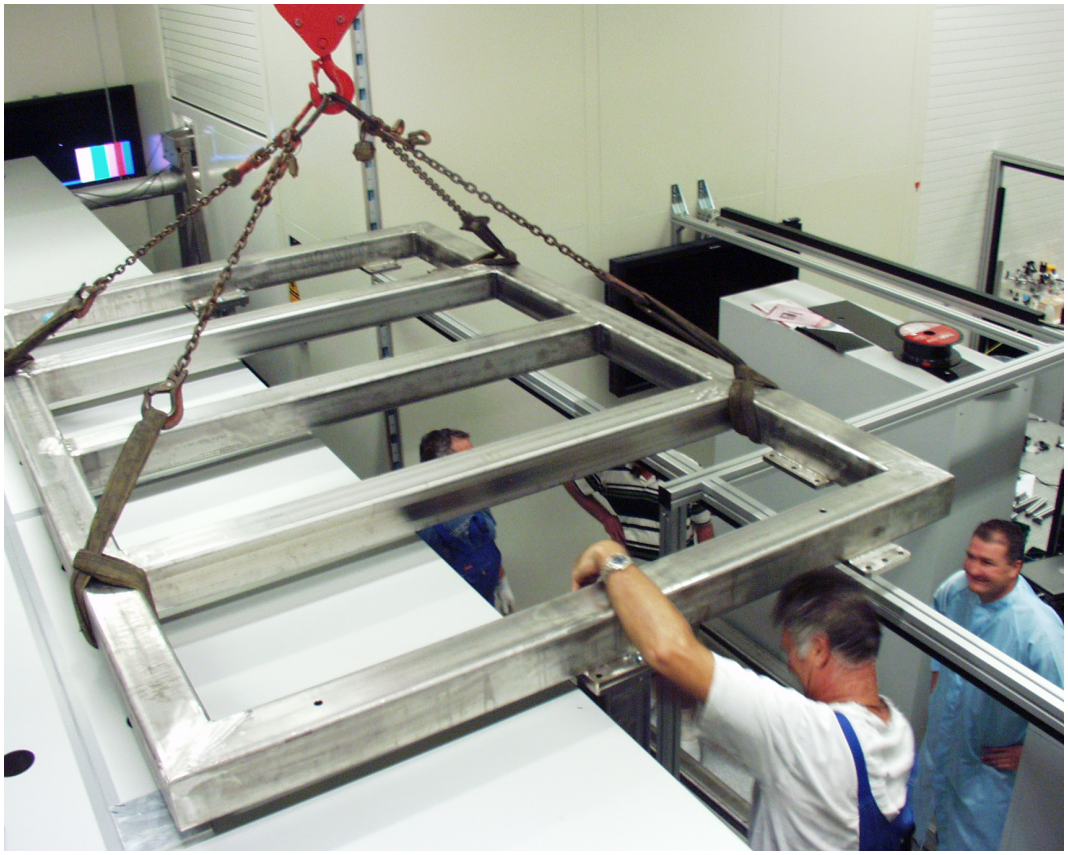

Figure A.3: The first part is resting safely on the laser housing. Prof. Kienberger supervises the progress and has everything safely under control.

Figure A.4: To stabilize the bridge above the laser huge steel pillars are needed.

Figure A.5: During the construction laser work has to stop, so speed is of the essence.

Figure A.6: The bridge seems stable enough for a first static load test.

Figure A.7: Everything holds, although not all screws are tightened yet.

Figure A.8: Now that the bridge is safely installed, the vacuum chambers need to be put into place.

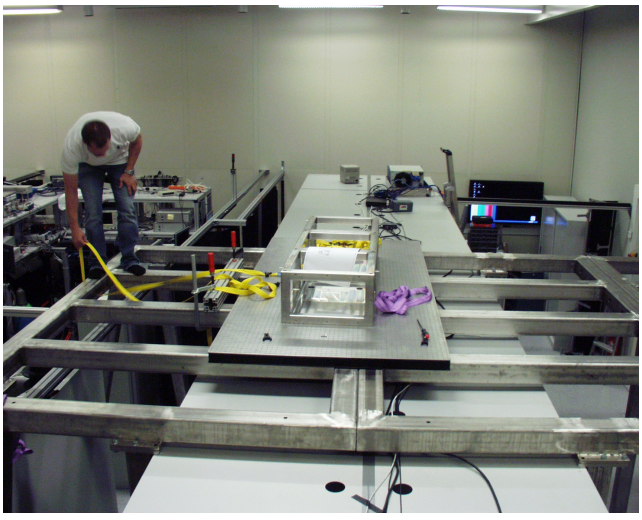

Figure A.9: There is still a lot of work left, but at least the basic fundament for the new high-flux XUV beamline AS 6 has been laid!

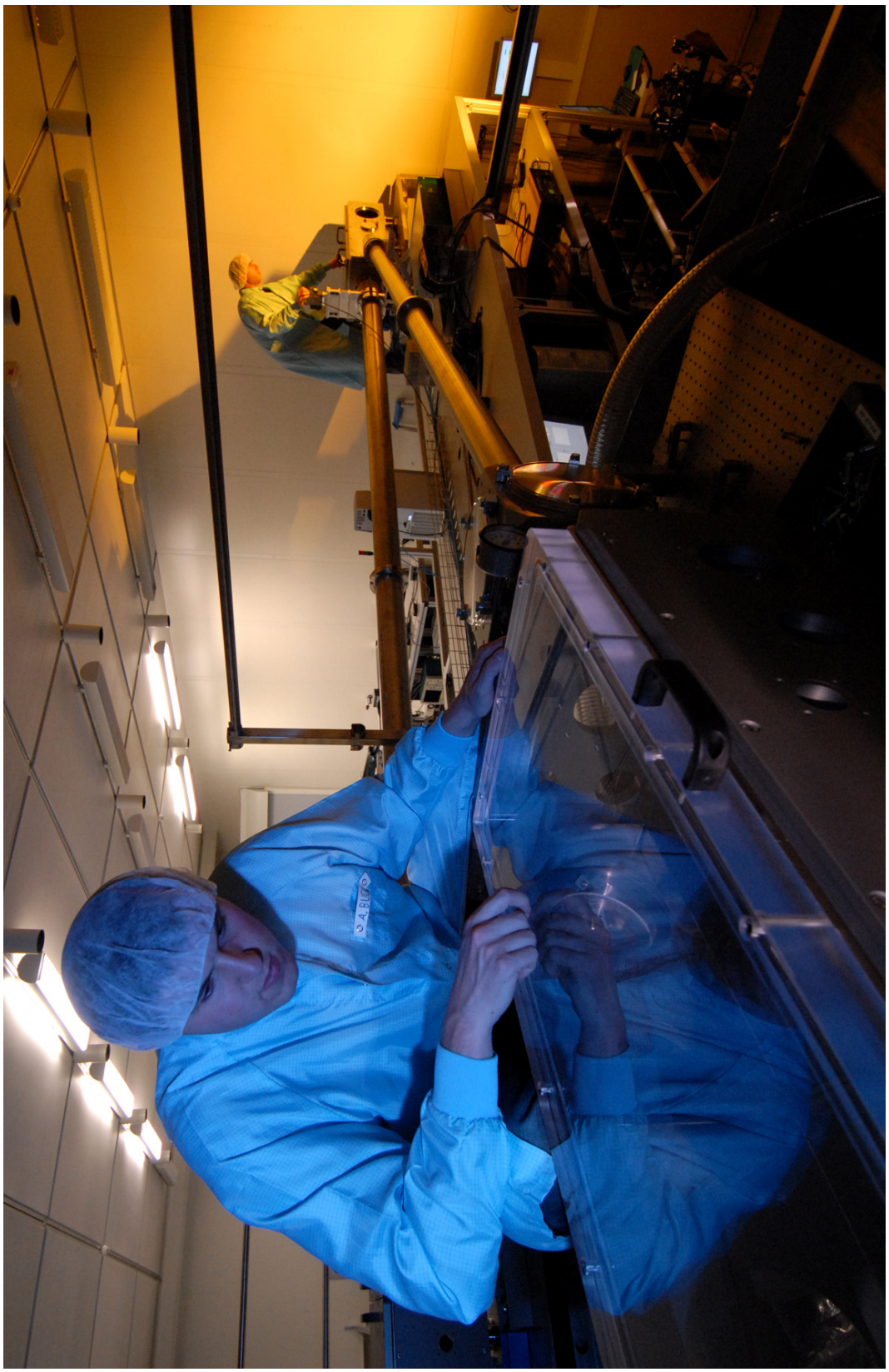

Figure A.10: AS 6 beamline at large.

Appendix B

List of Acronyms

AMO	atomic, molecular and optical science
AS 4	AttoSecond 4
AS 6	AttoSecond 6
ASE	amplified spontaneous emission
BC	bunch compressor chicane
CCD	charge-coupled device
CEP	carrier–envelope phase
CPA	chirped-pulse amplification
DFG	difference-frequency generation
FEL	free-electron laser
FLASH	Free-Electron Laser in Hamburg
FROG	frequency-resolved optical gating
FWHM	full width at half maximum
GD	group delay
GDD	group delay dispersion
HCF	hollow-core fiber
HH	high harmonic
HHG	high-order harmonic generation
IR	infrared
LCLS	Linac Coherent Light Source
LWS 1	Light Wave Synthesizer 1
LWS 20	Light Wave Synthesizer 20
MBES	magnetic bottle electron spectrometer

MPQ	Max-Planck-Institute of Quantum Optics
NIR	near-infrared
OPA	optical parametric amplification
OPCPA	optical parametric chirped-pulse amplification
PE	photoelectron
pnCCD	positive–negative-junction charge-coupled device
PPLN	periodically poled lithium niobate
QPM	quasi-phase-matching
rms	root mean square
SASE	self-amplified spontaneous emission
SDD	silicon drift detector
SFA	strong-field approximation
SHG	second harmonic generation
SLAC	Stanford Linear Accelerator Center
SPM	self-phase-modulaton
THG	third harmonic generation
THz	terahertz
XUV	extreme ultraviolet

References

[1] Capelle, W. *Die Vorsokratiker* (Alfred Kröner, Stuttgart, 1938).

[2] Ippen, E. P., Eilenberger, D. J. & Dixon, R. W. Picosecond pulse generation by passive mode locking of diode lasers. *Applied Physics Letters* **37**, 267 (1980).

[3] Krausz, F. *et al.* Femtosecond solid-state lasers. *IEEE Journal of Quantum Electronics* **28**, 2097–2122 (1992).

[4] Hentschel, M. *et al.* Attosecond metrology. *Nature* **414**, 509–13 (2001).

[5] Goulielmakis, E. *et al.* Single-cycle nonlinear optics. *Science (New York, N.Y.)* **320**, 1614–7 (2008).

[6] Seres, J. *et al.* Laser technology: Source of coherent kiloelectronvolt X-rays. *Nature* **433**, 596 (2005).

[7] Drescher, M. *et al.* X-ray pulses approaching the attosecond frontier. *Science (New York, N.Y.)* **291**, 1923–7 (2001).

[8] Paul, P. M. *et al.* Observation of a train of attosecond pulses from high harmonic generation. *Science (New York, N.Y.)* **292**, 1689–92 (2001).

[9] Drescher, M. *et al.* Time-resolved atomic inner-shell spectroscopy. *Nature* **419**, 803–7 (2002).

[10] Kienberger, R. *et al.* Steering attosecond electron wave packets with light. *Science (New York, N.Y.)* **297**, 1144–8 (2002).

[11] Kling, M. F. *et al.* Control of electron localization in molecular dissociation. *Science (New York, N.Y.)* **312**, 246–8 (2006).

[12] Uiberacker, M. *et al.* Attosecond real-time observation of electron tunnelling in atoms. *Nature* **446**, 627–32 (2007).

[13] Cavalieri, A. L. *et al.* Attosecond spectroscopy in condensed matter. *Nature* **449**, 1029–32 (2007).

[14] Sansone, G. *et al.* Electron localization following attosecond molecular photoionization. *Nature* **465**, 763–6 (2010).

[15] Goulielmakis, E. *et al.* Real-time observation of valence electron motion. *Nature* **466**, 739–43 (2010).

[16] Schultze, M. *et al.* Delay in photoemission. *Science (New York, N.Y.)* **328**, 1658–62 (2010).

[17] Klünder, K. *et al.* Probing Single-Photon Ionization on the Attosecond Time Scale. *Physical Review Letters* **106** (2011).

[18] Madey, J. M. J. Stimulated Emission of Bremsstrahlung in a Periodic Magnetic Field. *Journal of Applied Physics* **42**, 1906 (1971).

[19] Elias, L., Fairbank, W., Madey, J., Schwettman, H. & Smith, T. Observation of Stimulated Emission of Radiation by Relativistic Electrons in a Spatially Periodic Transverse Magnetic Field. *Physical Review Letters* **36**, 717–720 (1976).

[20] Deacon, D. *et al.* First Operation of a Free-Electron Laser. *Physical Review Letters* **38**, 892–894 (1977).

[21] Bonifacio, R., Pellegrini, C. & Narducci, L. Collective instabilities and high-gain regime in a free electron laser. *Optics Communications* **50**, 373–378 (1984).

[22] Milton, S. V. Exponential Gain and Saturation of a Self-Amplified Spontaneous Emission Free-Electron Laser. *Science* **292**, 2037–2041 (2001).

[23] Ackermann, W. *et al.* Operation of a free-electron laser from the extreme ultraviolet to the water window. *Nature Photonics* **1**, 336–342 (2007).

[24] Shintake, T. *et al.* A compact free-electron laser for generating coherent radiation in the extreme ultraviolet region. *Nature Photonics* **2**, 555–559 (2008).

[25] Emma, P. *et al.* First lasing and operation of an ångstrom-wavelength free-electron laser. *Nature Photonics* **4**, 641–647 (2010).

[26] Pile, D. X-rays: First light from SACLA. *Nature Photonics* **5**, 456–457 (2011).

[27] Emma, P. *et al.* Femtosecond and Subfemtosecond X-Ray Pulses from a Self-Amplified Spontaneous-Emission–Based Free-Electron Laser. *Physical Review Letters* **92** (2004).

[28] Huang, Z. & Kim, K.-J. Review of x-ray free-electron laser theory. *Physical Review Special Topics - Accelerators and Beams* **10**, 034801 (2007).

[29] Einstein, A. Über einen die Erzeugung und Verwandlung des Lichtes betreffenden heuristischen Gesichtspunkt. *Annalen der Physik* **322**, 132–148 (1905).

[30] Schawlow, A. & Townes, C. Infrared and Optical Masers. *Physical Review* **112**, 1940–1949 (1958).

[31] Maiman, T. H. Stimulated Optical Radiation in Ruby. *Nature* **187**, 493–494 (1960).

[32] Brabec, T. & Krausz, F. Intense few-cycle laser fields: Frontiers of nonlinear optics. *Reviews of Modern Physics* **72**, 545–591 (2000).

[33] Keldysh, L. V. Ionization in the field of a strong electromagnetic wave. *Soviet Physics - JEPT* **20**, 1307–1314 (1965).

[34] Corkum, P. Plasma perspective on strong field multiphoton ionization. *Physical Review Letters* **71**, 1994–1997 (1993).

[35] Schafer, K., Yang, B., DiMauro, L. & Kulander, K. Above threshold ionization beyond the high harmonic cutoff. *Physical Review Letters* **70**, 1599–1602 (1993).

[36] Krausz, F. & Ivanov, M. Y. Attosecond physics. *Reviews of Modern Physics* **81**, 163–234 (2009).

[37] Krause, J., Schafer, K. & Kulander, K. High-order harmonic generation from atoms and ions in the high intensity regime. *Physical Review Letters* **68**, 3535–3538 (1992).

[38] Lewenstein, M., Balcou, P., Ivanov, M., L'Huillier, A. & Corkum, P. Theory of high-harmonic generation by low-frequency laser fields. *Physical Review A* **49**, 2117–2132 (1994).

[39] Walker, B., Sheehy, B., Kulander, K. & DiMauro, L. Elastic Rescattering in the Strong Field Tunneling Limit. *Physical Review Letters* **77**, 5031–5034 (1996).

[40] Paulus, G. G. *et al.* Absolute-phase phenomena in photoionization with few-cycle laser pulses. *Nature* **414**, 182–4 (2001).

[41] Wittmann, T. *et al.* Single-shot carrier–envelope phase measurement of few-cycle laser pulses. *Nature Physics* **5**, 357–362 (2009).

[42] L'Huillier, A., Lompre, L. A., Mainfray, G. & Manus, C. Multiply charged ions induced by multiphoton absorption in rare gases at 0.53 μm. *Physical Review A* **27**, 2503–2512 (1983).

[43] Fittinghoff, D., Bolton, P., Chang, B. & Kulander, K. Observation of nonsequential double ionization of helium with optical tunneling. *Physical Review Letters* **69**, 2642–2645 (1992).

[44] Cavalieri, A. L. *et al.* Intense 1.5-cycle near infrared laser waveforms and their use for the generation of ultra-broadband soft-x-ray harmonic continua. *New Journal of Physics* **9**, 242–242 (2007).

[45] Goulielmakis, E. *et al.* Attosecond control and measurement: lightwave electronics. *Science (New York, N.Y.)* **317**, 769–75 (2007).

[46] Christov, I. P., Murnane, M. M. & Kapteyn, H. C. High-Harmonic Generation of Attosecond Pulses in the "Single-Cycle" Regime. *Physical Review Letters* **78**, 1251–1254 (1997).

[47] Baltuška, A. *et al.* Attosecond control of electronic processes by intense light fields. *Nature* **421**, 611–615 (2003).

[48] Fuji, T. *et al.* Monolithic carrier-envelope phase-stabilization scheme. *Optics Letters* **30**, 332 (2005).

[49] Corkum, P. B. & Krausz, F. Attosecond science. *Nature Physics* **3**, 381–387 (2007).

[50] Gordon, A. & Franz, X. K. Scaling of keV HHG photon yield with drive wavelength. *Optics Express* **13**, 2941–2947 (2005).

[51] Tate, J. *et al.* Scaling of Wave-Packet Dynamics in an Intense Midinfrared Field. *Physical Review Letters* **98**, 1–4 (2007).

[52] Frolov, M., Manakov, N. & Starace, A. Wavelength Scaling of High-Harmonic Yield: Threshold Phenomena and Bound State Symmetry Dependence. *Physical Review Letters* **100** (2008).

[53] Yakovlev, V. S., Ivanov, M. Y. & Krausz, F. Enhanced phase-matching for generation of soft X-ray harmonics and attosecond pulses in atomic gases. *Optics Express* **15**, 15351–64 (2007).

[54] Sheehy, B. *et al.* High Harmonic Generation at Long Wavelengths. *Physical Review Letters* **83**, 5270–5273 (1999).

[55] Shan, B. & Chang, Z. Dramatic extension of the high-order harmonic cutoff by using a long-wavelength driving field. *Physical Review A* **65** (2001).

[56] Popmintchev, T. *et al.* Extended phase matching of high harmonics driven by mid-infrared light. *Optics Letters* **33**, 2128–30 (2008).

[57] Popmintchev, T. *et al.* Bright Coherent Ultrahigh Harmonics in the keV X-ray Regime from Mid-Infrared Femtosecond Lasers. *Science* **336**, 1287–1291 (2012).

[58] Galayda, J. N., Arthur, J., Ratner, D. F. & White, W. E. X-ray free-electron lasers—present and future capabilities [Invited]. *Journal of the Optical Society of America B* **27**, B106 (2010).

[59] Murphy, J. B. & Pellegrini, C. Free electron lasers for the XUV spectral region. *Nuclear Instruments and Methods in Physics Research Section A: Accelerators, Spectrometers, Detectors and Associated Equipment* **237**, 159–167 (1985).

[60] Bonifacio, R., De Salvo, L., Pierini, P., Piovella, N. & Pellegrini, C. Spectrum, temporal structure, and fluctuations in a high-gain free-electron laser starting from noise. *Physical Review Letters* **73**, 70–73 (1994).

[61] Krinsky, S. & Gluckstern, R. Analysis of statistical correlations and intensity spiking in the self-amplified spontaneous-emission free-electron laser. *Physical Review Special Topics - Accelerators and Beams* **6**, 050701 (2003).

[62] Vinokurov, N., Huang, Z., Shevchenko, O. & Kim, K.-J. Quasilinear theory of high-gain FEL saturation. *Nuclear Instruments and Methods in Physics Research Section A: Accelerators, Spectrometers, Detectors and Associated Equipment* **475**, 74–78 (2001).

[63] Xie, M. Design optimization for an X-ray free electron laser driven by SLAC linac. In *Proceedings Particle Accelerator Conference*, vol. 1, 183–185 (IEEE, 1995).

[64] Gu, X. *et al.* Few-Cycle Mid-Infrared OPCPA System. To be published.

[65] Marcus, G. *et al.* Subfemtosecond K-Shell Excitation with a Few-Cycle Infrared Laser Field. *Physical Review Letters* **108** (2012).

[66] Dubietis, A., Butkus, R. & Piskarskas, A. Trends in chirped pulse optical parametric amplification. *IEEE Journal of Selected Topics in Quantum Electronics* **12**, 163–172 (2006).

[67] Dubietis, A., Jonušauskas, G. & Piskarskas, A. Powerful femtosecond pulse generation by chirped and stretched pulse parametric amplification in BBO crystal. *Optics Communications* **88**, 437–440 (1992).

[68] Ross, I., Matousek, P., Towrie, M., Langley, A. & Collier, J. The prospects for ultrashort pulse duration and ultrahigh intensity using op-

tical parametric chirped pulse amplifiers. *Optics Communications* **144**, 125–133 (1997).

[69] Butkus, R., Danielius, R., Dubietis, A., Piskarskas, A. & Stabinis, A. Progress in chirped pulse optical parametric amplifiers. *Applied Physics B* **79**, 693–700 (2004).

[70] Tavella, F., Marcinkevicius, A. & Krausz, F. 90 mJ parametric chirped pulse amplification of 10 fs pulses. *Optics Express* **14**, 12822 (2006).

[71] Herrmann, D. *et al.* Generation of sub-three-cycle, 16 TW light pulses by using noncollinear optical parametric chirped-pulse amplification. *Optics Letters* **34**, 2459–61 (2009).

[72] Adachi, S. *et al.* 5-fs, multi-mJ, CEP-locked parametric chirped-pulse amplifier pumped by a 450-nm source at 1 kHz. *Optics Express* **16**, 14341 (2008).

[73] Witte, S. *et al.* A source of 2 terawatt, 2.7 cycle laser pulses based on noncollinear optical parametric chirped pulse amplification. *Optics Express* **14**, 8168 (2006).

[74] Zimmermann, M., Gohle, C., Holzwarth, R., Udem, T. & Hnsch, T. W. Optical clockwork with an offset-free difference-frequency comb: accuracy of sum- and difference-frequency generation. *Optics Letters* **29**, 310 (2004).

[75] Fuji, T., Apolonski, A. & Krausz, F. Self-stabilization of carrier-envelope offset phase by use of difference-frequency generation. *Optics Letters* **29**, 632–4 (2004).

[76] Manzoni, C., Cerullo, G. & De Silvestri, S. Ultrabroadband self-phase-stabilized pulses by difference-frequency generation. *Optics Letters* **29**, 2668 (2004).

[77] Baltuška, A., Fuji, T. & Kobayashi, T. Controlling the Carrier-Envelope Phase of Ultrashort Light Pulses with Optical Parametric Amplifiers. *Physical Review Letters* **88** (2002).

[78] Tavella, F. *Multiterawatt few-cycle pulse OPCPA for applications in high-field physics*. Doctoral thesis, Ludwig-Maximilians-Universität München (2007).

[79] Gu, X. *et al.* Generation of carrier-envelope-phase-stable 2-cycle 740-μJ pulses at 2.1-μm carrier wavelength. *Optics Express* **17**, 62–9 (2009).

[80] Fuji, T. *et al.* Parametric amplification of few-cycle carrier-envelope phase-stable pulses at 2.1 μm. *Optics Letters* **31**, 1103 (2006).

[81] Ishii, N. *et al.* Seeding of an eleven femtosecond optical parametric chirped pulse amplifier and its Nd^3+ picosecond pump laser from a single broadband Ti:Sapphire oscillator. *IEEE Journal of Selected Topics in Quantum Electronics* **12**, 173–180 (2006).

[82] Teisset, C. Y. *et al.* Soliton-based pump-seed synchronization for few-cycle OPCPA. *Optics Express* **13**, 6550 (2005).

[83] Tsang, T. Y. F. Surface-plasmon-enhanced third-harmonic generation in thin silver films. *Optics Letters* **21**, 245 (1996).

[84] Colosimo, P. *et al.* Scaling strong-field interactions towards the classical limit. *Nature Physics* **4**, 386–389 (2008).

[85] Salières, P., L'Huillier, A. & Lewenstein, M. Coherence Control of High-Order Harmonics. *Physical Review Letters* **74**, 3776–3779 (1995).

[86] Meidinger, N. *et al.* pnCCD for photon detection from near-infrared to X-rays. *Nuclear Instruments and Methods in Physics Research Section A: Accelerators, Spectrometers, Detectors and Associated Equipment* **565**, 251–257 (2006).

[87] Hartmann, R. *et al.* A high-speed pnCCD detector system for optical applications. *Nuclear Instruments and Methods in Physics Research Section A: Accelerators, Spectrometers, Detectors and Associated Equipment* **568**, 118–123 (2006).

[88] Holl, P. *et al.* pnCCDs for Ultra-Fast and Ultra-Sensitive Optical and NIR Imaging. In *AIP Conference Proceedings*, vol. 984, 115–123 (AIP, 2008).

[89] Strüder, L. *et al.* Large-format, high-speed, X-ray pnCCDs combined with electron and ion imaging spectrometers in a multipurpose chamber for experiments at 4th generation light sources. *Nuclear Instruments and Methods in Physics Research Section A: Accelerators, Spectrometers, Detectors and Associated Equipment* **614**, 483–496 (2010).

[90] Popmintchev, T. *et al.* Phase matching of high harmonic generation in the soft and hard X-ray regions of the spectrum. *Proceedings of the National Academy of Sciences of the United States of America* **106**, 10516–21 (2009).

[91] Constant, E. *et al.* Optimizing High Harmonic Generation in Absorbing Gases: Model and Experiment. *Physical Review Letters* **82**, 1668–1671 (1999).

[92] Takahashi, E. J., Kanai, T., Ishikawa, K. L., Nabekawa, Y. & Midorikawa, K. Coherent Water Window X Ray by Phase-Matched High-Order Harmonic Generation in Neutral Media. *Physical Review Letters* **101** (2008).

[93] Balcou, P., Sali'eres, P., L'Huillier, A. & Lewenstein, M. Generalized phase-matching conditions for high harmonics: The role of field-gradient forces. *Physical Review A* **55**, 3204–3210 (1997).

[94] Gaarde, M. B., Tate, J. L. & Schafer, K. J. Macroscopic aspects of attosecond pulse generation. *Journal of Physics B: Atomic, Molecular and Optical Physics* **41**, 132001 (2008).

[95] Glover, T. E. *et al.* Controlling X-rays with light. *Nature Physics* **6**, 69–74 (2010).

[96] Michelin, S. *et al.* Angle-resolved inner-shell excitation in N2 molecules by electron impact. *Chemical Physics* **293**, 365–374 (2003).

[97] Ammosov, M. V., Delone, N. B. & Krainov, V. P. Tunneling ionization of complex atoms and of atomic ions in an alternating electromagnetic field. *Sov. Phys. JETP* **64**, 1191–1194 (1986).

[98] Rohringer, N. An atomic inner-shell laser pumped with an x-ray free-electron laser. *Journal of Physics: Conference Series* **194**, 012012 (2009).

[99] Henke, B., Gullikson, E. & Davis, J. X-Ray Interactions: Photoabsorption, Scattering, Transmission, and Reflection at E = 50-30,000 eV, Z = 1-92. *Atomic Data and Nuclear Data Tables* **54**, 181–342 (1993).

[100] Popmintchev, T., Chen, M.-C., Arpin, P., Murnane, M. M. & Kapteyn, H. C. The attosecond nonlinear optics of bright coherent X-ray generation. *Nature Photonics* **4**, 822–832 (2010).

[101] Wörner, H. J., Bertrand, J. B., Kartashov, D. V., Corkum, P. B. & Villeneuve, D. M. Following a chemical reaction using high-harmonic interferometry. *Nature* **466**, 604–7 (2010).

[102] Schultze, M. *et al.* State-of-the-art attosecond metrology. *Journal of Electron Spectroscopy and Related Phenomena* **184**, 68–77 (2011).

[103] Wieland, M. *et al.* Toward time-resolved soft X-ray microscopy using pulsed fs-high-harmonic radiation. *Ultramicroscopy* **102**, 93–100 (2005).

[104] Dierolf, M. *et al.* Ptychographic X-ray computed tomography at the nanoscale. *Nature* **467**, 436–9 (2010).

[105] Chapman, H. N. *et al.* Femtosecond X-ray protein nanocrystallography. *Nature* **470**, 73–7 (2011).

[106] Takahashi, E., Nabekawa, Y. & Midorikawa, K. Generation of 10-μJ coherent extreme-ultraviolet light by use of high-order harmonics. *Optics Letters* **27**, 1920 (2002).

[107] Hergott, J.-F. *et al.* Extreme-ultraviolet high-order harmonic pulses in the microjoule range. *Physical Review A* **66** (2002).

[108] Zeitoun, P. *et al.* A high-intensity highly coherent soft X-ray femtosecond laser seeded by a high harmonic beam. *Nature* **431**, 426–9 (2004).

[109] Schnürer, M. *et al.* Few-cycle-driven XUV laser harmonics: generation and focusing. *Applied Physics B* **70**, S227–S232 (2000).

[110] Tavella, F. *et al.* High-dynamic range pulse-contrast measurements of a broadband optical parametric chirped-pulse amplifier. *Applied Physics B* **81**, 753–756 (2005).

[111] Tavella, F., Marcinkevičius, A. & Krausz, F. Investigation of the superfluorescence and signal amplification in an ultrabroadband multiterawatt optical parametric chirped pulse amplifier system. *New Journal of Physics* **8**, 219–219 (2006).

[112] Tavella, F. *et al.* Dispersion management for a sub-10-fs, 10 TW optical parametric chirped-pulse amplifier. *Optics Letters* **32**, 2227–9 (2007).

[113] Nisoli, M., De Silvestri, S. & Svelto, O. Generation of high energy 10 fs pulses by a new pulse compression technique. *Applied Physics Letters* **68**, 2793 (1996).

[114] Brewer, R. Frequency Shifts in Self-Focused Light. *Physical Review Letters* **19**, 8–10 (1967).

[115] Kane, S. & Squier, J. Grism-pair stretcher–compressor system for simultaneous second- and third-order dispersion compensation in chirped-pulse amplification. *Journal of the Optical Society of America B* **14**, 661 (1997).

[116] Gibson, E. A. *et al.* Efficient reflection grisms for pulse compression and dispersion compensation of femtosecond pulses. *Optics Letters* **31**, 3363 (2006).

[117] Ishii, N. *et al.* Widely tunable soliton frequency shifting of few-cycle laser pulses. *Physical Review E* **74**, 1–10 (2006).

[118] Planchon, T. A., Rousseau, J.-P., Burgy, F., Chériaux, G. & Chambaret, J.-P. Adaptive wavefront correction on a 100-TW/10-Hz chirped pulse amplification laser and effect of residual wavefront on beam propagation. *Optics Communications* **252**, 222–228 (2005).

[119] Nicolle, M., Fusco, T., Rousset, G. & Michau, V. Improvement of Shack-Hartmann wave-front sensor measurement for extreme adaptive optics. *Optics Letters* **29**, 2743 (2004).

[120] Perry, M. D., Ditmire, T. & Stuart, B. C. Self-phase modulation in chirped-pulse amplification. *Optics letters* **19**, 2149–51 (1994).

[121] Schmid, K. *Supersonic Micro-Jets And Their Application to Few-Cycle Laser-Driven Electron Acceleration.* Doctoral thesis, Ludwig-Maximilians-Universität München (2009).

[122] Ravasio, A. *et al.* Single-Shot Diffractive Imaging with a Table-Top Femtosecond Soft X-Ray Laser-Harmonics Source. *Physical Review Letters* **103** (2009).

[123] Nabekawa, Y. & Midorikawa, K. Nonlinear Optics for Characterizing XUV/Soft X-ray High-order Harmonic Fields in Attosecond Regime. In Lin, S. H., Villaeys, A. A. & Fujimura, Y. (eds.) *Advances in Multi-Photon Processes and Spectroscopy - Vol. 18*, Advances in Multi-Photon Processes and Spectroscopy, chap. 1, 304 (World Scientific Publishing Co., Singapore, 2008). URL `http://www.worldscibooks.com/physics/6743.html`.

[124] Mashiko, H., Suda, A., Midorikawa, K. & Omi, K. Focusing coherent XUV light to micron spot size with an intensity of 1014 W/cm2 - Technical Digest (CD). In *Conference on Lasers and Electro-Optics/International Quantum Electronics Conference and Photonic Applications Systems Technologies*, JMD1 (Optical Society of America, 2004).

[125] Mimura, H. *et al.* Breaking the 10 nm barrier in hard-X-ray focusing. *Nature Physics* **6**, 122–125 (2009).

[126] Reese, M. *et al.* Submicron focusing of XUV radiation from a laser plasma source using a multilayer Laue lens. *Applied Physics A* **102**, 85–90 (2010).

[127] Tzallas, P., Skantzakis, E., Nikolopoulos, L. A. A., Tsakiris, G. D. & Charalambidis, D. Extreme-ultraviolet pump–probe studies of one-femtosecond-scale electron dynamics. *Nature Physics* **7**, 781–784 (2011).

[128] Gibson, E. a. *et al.* Coherent soft x-ray generation in the water window with quasi-phase matching. *Science (New York, N.Y.)* **302**, 95–8 (2003).

[129] Seres, J. *et al.* Coherent superposition of laser-driven soft-X-ray harmonics from successive sources. *Nature Physics* **3**, 878–883 (2007).

[130] Tosa, V., Yakovlev, V. S. & Krausz, F. Generation of tunable isolated attosecond pulses in multi-jet systems. *New Journal of Physics* **10**, 025016 (2008).

[131] Helml, W. *et al.* Measuring the world's shortest X-ray pulses directly in the time domain (2012). In review by *Nature Photonics*.

[132] Krinsky, S. & Li, Y. Statistical analysis of the chaotic optical field from a self-amplified spontaneous-emission free-electron laser. *Physical Review E* **73** (2006).

[133] Reiche, S. GENESIS 1.3: a fully 3D time-dependent FEL simulation code. *Nuclear Instruments and Methods in Physics Research Section A: Accelerators, Spectrometers, Detectors and Associated Equipment* **429**, 243–248 (1999).

[134] Ding, Y. *et al.* Measurements and Simulations of Ultralow Emittance and Ultrashort Electron Beams in the Linac Coherent Light Source. *Physical Review Letters* **102** (2009).

[135] Itatani, J. *et al.* Attosecond Streak Camera. *Physical Review Letters* **88** (2002).

[136] Kienberger, R. *et al.* Atomic transient recorder. *Nature* **427**, 817–21 (2004).

[137] Frühling, U. *et al.* Single-shot terahertz-field-driven X-ray streak camera. *Nature Photonics* **3**, 523–528 (2009).

[138] Düsterer, S. *et al.* Femtosecond x-ray pulse length characterization at the Linac Coherent Light Source free-electron laser. *New Journal of Physics* **13**, 093024 (2011).

[139] Schorb, S. *et al.* X-ray–optical cross-correlator for gas-phase experiments at the Linac Coherent Light Source free-electron laser. *Applied Physics Letters* **100**, 121107 (2012).

[140] Lutman, A. *et al.* Femtosecond x-ray free electron laser pulse duration measurement from spectral correlation function. *Physical Review Special Topics - Accelerators and Beams* **15**, 1–13 (2012).

[141] Young, L. *et al.* Femtosecond electronic response of atoms to ultra-intense X-rays. *Nature* **466**, 56–61 (2010).

[142] Kitzler, M., Milosevic, N., Scrinzi, A., Krausz, F. & Brabec, T. Quantum Theory of Attosecond XUV Pulse Measurement by Laser Dressed Photoionization. *Physical Review Letters* **88** (2002).

[143] Goulielmakis, E. *et al.* Direct measurement of light waves. *Science (New York, N.Y.)* **305**, 1267–9 (2004).

[144] Schins, J. *et al.* Observation of Laser-Assisted Auger Decay in Argon. *Physical Review Letters* **73**, 2180–2183 (1994).

[145] Glover, T., Schoenlein, R., Chin, A. & Shank, C. Observation of Laser Assisted Photoelectric Effect and Femtosecond High Order Harmonic Radiation. *Physical Review Letters* **76**, 2468–2471 (1996).

[146] Gagnon, J. & Yakovlev, V. S. The robustness of attosecond streaking measurements. *Optics Express* **17**, 17678 (2009).

[147] Bozek, J. D. AMO instrumentation for the LCLS X-ray FEL. *The European Physical Journal Special Topics* **169**, 129–132 (2009).

[148] Kruit, P. & Read, F. H. Magnetic field paralleliser for 2π electron-spectrometer and electron-image magnifier. *Journal of Physics E: Scientific Instruments* **16**, 313–324 (1983).

[149] Yakovlev, V. S., Gagnon, J., Karpowicz, N. & Krausz, F. Attosecond Streaking Enables the Measurement of Quantum Phase. *Physical Review Letters* **105**, 3–6 (2010).

Danksagung

Mein erster Dank gilt Prof. Kienberger, meinem Doktorvater und Freund. Reini ist in vielerlei Hinsicht schuld daran, dass es mich überhaupt nach Garching verschlagen hat und er sorgt jetzt in ähnlich konsequenter Weise dafür, dass er mich rechtzeitig wieder los wird – wenigstens für die nächsten knapp zwei Jahre! Wenn es auf einer Elite-Universität im 21. Jahrhundert noch so etwas wie eine mentorenhafte Rundumbetreuung gibt, dann habe ich sie genießen dürfen. Der Fülle an Gelegenheiten, bei denen ich von Reini gelernt, von seinem Wissen und seiner Erfahrung als Forscher profitiert, mit ihm politisiert, auf einen Berg gestiegen oder einfach ein kühles Helles getrunken habe, kann hier nicht erschöpfend entsprochen werden. Es bleibt am Ende nur zu sagen: „Heil Dir und Danke, Reini!“

Mein zweiter Dank gilt Prof. Ferenc Krausz, der mich vor mittlerweile über fünf Jahren mit großem Enthusiasmus in seiner Attosekundengruppe willkommen geheißen hat, obwohl ich damals ein quantenoptischer Komplettneueinsteiger war. An die Begrüßung „Sagen wir Ferenc, das ist einfacher!“ werde ich mich wohl mein Leben lang erinnern. Die Möglichkeit hier, quasi an der Quelle, in die Laserkurzpulsphysik einzutauchen, war eine großartige Erfahrung und hat meinen weiteren wissenschaftlichen Werdegang sicher entscheidend mitgeprägt.

Unter meinen Kollegen am Max-Planck-Institut für Quantenoptik sind auch einige, mit denen sich im Laufe der Jahre eine echte Freundschaft entwickelt hat. Zuvorderst ist hier Martin zu nennen, mit dem mich mittlerweile nicht nur das wohl legendärste Lagerfeuer des südwestlichen Israels und eine glorreiche Büronachbarschaft verbinden, sondern auch die tiefe Liebe zum Bierbrauen und zu blonden Brauerinnen sowie die kalifornische Abenteuerlust. Yunpei Deng, der chinesische Panda, ist mir gerade wegen seiner Schrulligkeiten ans Herz gewachsen und war besonders dann ein begeisternder Motivationskünstler, wenn es darum ging, statt des Labors doch noch den Fußballplatz aufzusuchen – auch wenn er sich dann auf dem Platz nicht mehr ganz so motiviert bewegte.

Mit Franz habe ich die nassen Weiten Patagoniens durchquert und mit Adrian nicht nur meine ersten Lehrstunden am Femtopower absolviert, sondern auch die verborgenen Winkel des Napa Valley erforscht. Tom hat mich in die Geheimnisse des Eiskletterns eingeführt, wofür ich mich mit einem Schiwochenende im Kühtai revanchiert habe, das wohl keiner der Beteiligten, inklusive Karl und Richi Lugner, vergessen wird. Mit Gilad und Xun habe ich mir unzählige lange Messnächte um die Ohren geschlagen und währenddessen nicht nur viel über Laserphysik gelernt, sondern auch einen tieferen Einblick in die israelische und die chinesische Kultur gewonnen. Elisabeth hat mir, neben der Empfehlung von Mendeley, das sich nicht nur für die Dissertation als Goldgriff erwiesen hat, auch in der ersten Zeit ohne Ralph an der AS 3 mehrfach und mit der ihr eigenen freundlichen Lockerheit helfend unter die Arme gegriffen. Simon hat sich ebenfalls als Mitglied der kleinen Braugemeinde bewährt und sorgt zusammen mit Gitti dafür, dass der Ruf des weltfremden Physikers im Weinbauern und in der SchwaSie ordentlich ins Wanken geraten ist.

Die Truppe der International Max Planck Research School, insbesondere angetrieben durch die aufopferungsvolle Tätigkeit von Frau Wild, hat die Doktorandenzeit sowohl wissenschaftlich als auch geselligerweise extrem bereichert; die Klavierliederabende auf Ringberg bleiben unvergessen, und noch heute muss ich immer wieder daran denken: „Oh, wie ist das schön!“ In diesem Zusammenhang möchte ich mich speziell bei Andi bedanken, mit dem zusammen ich erstens einen einmaligen Doppelvortrag zu halten das Vergnügen hatte und mit dem auch meine erste größere Veröffentlichung, die in dieser Arbeit beschriebene Messung der ultrakurzen Röntgenpulse an der LCLS, gemeinsam erarbeitet wurde.

Euch allen gilt mein aufrichtiger und herzlicher Dank und ich hoffe, dass wir noch viele weitere geistige und hochgeistige Abenteuer erleben werden, auch wenn mich der Weg in nächster Zukunft erst einmal über den großen Teich führen wird.

Zu guter Letzt gilt mein ganz besonderer Dank meinen Eltern, überhaupt meiner ganzen Familie und natürlich meiner Dorli. Die unablässige Unterstützung aus dem innersten Kreis fällt einem erst dann so richtig auf, wenn man sie plötzlich dringend braucht. Dann aber überfällt sie einen regelrecht, mit einer Wucht, die allein schon wieder Kraft und Mut für die anstehenden Aufgaben gibt.